NATURAL CONVECTION IN WATER-SATURATED METAL FOAM WITH A SUPERPOSED FLUID LAYER

A THESIS
SUBMITTED TO THE FACULTY OF THE GRADUATE SCHOOL
OF THE UNIVERSITY OF MINNESOTA
BY

Aaron D. Wade

IN PARTIAL FULFILLMENT OF THE REQUIREMENTS
FOR THE DEGREE OF
MASTER OF SCIENCE

Dr. Jane H. Davidson, Adviser,

Dr. Francis A. Kulacki, Co-adviser

November 2010

ACKNOWLEDGEMENT

I would like to acknowledge all those who made this thesis possible. I would first like to thank my advisor, Professor Jane Davidson, for her continuous guidance and support over the past four years. I am grateful for the countless hours she dedicated to bettering this work. I would also like to offer a hearty thank you to my co-adviser, Professor Frank Kulacki, for sharing his porous media expertise with me. I want to thank Professor Terry Simon for his thoughtful discussions on porous media, and the use of his laboratory to perform pressure drop experiments. Both Robert Nelson and Peter Zimmermann generously offered their help and discussions surrounding my experimental apparatus. This project would not have been possible without funding from the National Renewable Energy Lab and the University of Minnesota Initiative for Renewable Energy and the Environment.

I am grateful to all of my colleagues who supported me in this process. In particular, I would like to thank my lab mates and fellow graduate students Vinayak Kathare, Julia Haltiwanger, Brandon Hathaway, Luke Venstrom, Ben Adams, Tom Shepard, Katie Krueger, Clayton Fitzgerald, and Dan Keene. Not only did they offer thoughtful discussions and help with experimental design and analysis, but their lightness and friendship kept my spirits up through the process. I would like to thank Josh Quinnell in particular for our many discussions on porous media, and for his help with performing pressure drop experiments.

Thank you to my father, Larry, mother, Carol, and sisters, Laurel and Alli Wade, my partner, Mary Ellen Six, and to my furry companions, Mickey and Buster, for their

unwavering love and support. Lastly, I would like to offer my regards to my friends and any others who helped me in any aspect during the completion of this project.

ABSTRACT

Experimental results are presented for steady state natural convection heat transfer in an enclosure with a horizontal layer of copper foam and an overlying water layer, heated from below. The foam was placed between two parallel plates in a cylindrical enclosure adjacent to either one or both boundaries. The cylindrical copper foam disks were manufactured by ERG Aerospace with 127 mm DIA, with porosity ranging from 0.88 to 0.92, and pore densities of 5 and 10 PPI. The effective thermal conductivity of the foam was measured by running experiments at pre-convection Rayleigh numbers. The permeability and drag coefficient of the foam were determined by measuring the pressure drop across foam samples in a separate facility. With foam on the hot boundary, natural convection heat transfer experiments are run for 5 and 10 PPI foam, Rayleigh numbers, based on the total height of the enclosure and the water properties, from 2×10^6 to 5×10^8, aspect ratios, H/D, from 0.1 to 0.8, and ratios of the total foam layer height to the total height of the apparatus, $\eta = H_p/H$, of 0.25, 0.5, and 0.75. With foam on both boundaries, experiments are run for 10 PPI foam, Rayleigh numbers from 1×10^7 to 3×10^8, aspect ratios from 0.3 to 0.8, and η of 0.5 and 0.75. Natural convection heat transfer experiments were also performed for water alone over the Rayleigh number range $9 \times 10^5 – 3 \times 10^8$ and for aspect ratios 0.2 to 0.8. Heat transfer results are presented as an enhancement factor, the ratio of heat transfer with foam to that of water alone at the same Rayleigh number.

The results with foam on the hot boundary were not a function of η. 10 PPI foam on the hot boundary did not enhance heat transfer with an average enhancement factor of 0.98. 5 PPI foam on the hot boundary had an enhancement factor of 1.1. The increased

enhancement of 5 PPI foam over 10 PPI foam is attributed to the greater permeability of the 5 PPI foam. With foam on both boundaries, enhancement tended to increase with Rayleigh number and is a function of η. For $\eta = 0.5$ enhancement ranged from 0.93 to 1.33. For $\eta = 0.75$ enhancement ranged from 1.1 to 1.29. For the same enclosure filled with copper foam (from Kathare et al. [13]), enhancement was not a strong function of Rayleigh number and ranged from 1.2 to 1.6, though enhancement was typically above 1.35. The decreased enhancement of a partially filled enclosure, compared to a fully filled enclosure, is attributed to a lack of direct conduction path from each boundary, significantly decreasing the apparent conductivity of the enclosure, and decreased advection as the convection cells do not fully penetrate the porous layer(s).

Power law correlations relating the fluid Nusselt number to the fluid Rayleigh number were determined for the three foam cases. The data for foam on the hot boundary alone and on both boundaries were also successfully correlated using porous media variables where an apparent conductivity of the composite system, considering the foam and fluid layers in series, was used as the effective conductivity. The porous media Nusselt number is related to the porous media Rayleigh number and a modified porous media Prandtl number.

TABLE OF CONTENTS

ACKNOWLEDGEMENT **i**

ABSTRACT **iii**

TABLE OF CONTENTS **v**

LIST OF TABLES **vii**

LIST OF FIGURES **viii**

NOMENCLATURE **xi**

CHAPTER 1 INTRODUCTION **1**

1.1 Motivation and Objectives **1**

CHAPTER 2 BACKGROUND AND LITERATURE REVIEW **4**

2.1 Metal Foams Background **4**

2.1.1 Porosity, Pore Density, Specific Surface Area and Foam Structure *4*

2.1.2 Governing Equations for Modeling Porous Media and Metal Foam *7*

2.1.3 Conservation of Momentum *7*

2.1.4 Conservation of Energy *11*

2.2 Natural Convection in Horizontal Layer of Metal Foam in an Infinite Domain **12**

2.3 Rayleigh-Bénard Equivalent Convection Heat Transfer in Saturated Porous Media **15**

2.4 Rayleigh-Bénard Equivalent Convection Heat Transfer in Saturated Porous Media with a Superposed Fluid Layer **22**

2.5 Summary of Literature Review **38**

CHAPTER 3 DESIGN OF EXPERIMENTS **41**

3.1 Experimental Scope **41**

3.2 Experimental Apparatus **42**

3.2.1 Apparatus Overview *42*

3.2.2 Temperature and Power Measurement *44*

3.2.5 Pressure Drop Apparatus for Measuring Permeability and Drag Coefficient. *47*

3.3 Data Acquisition **49**

3.4 Experimental Procedure **50**

3.5 Data Analysis **51**

3.5.1 Foam Porosity, Effective Conductivity, Drag Coefficient and Permeability *52*

3.5.2 Temperature Measurement *53*

3.6.2 Heat Transfer *54*

3.6.3 Dimensionless Variables *54*

3.6.7 Heat Transfer Enhancement *58*

CHAPTER 4 RESULTS AND DISCUSSION **59**

4.1 Foam Properties **59**

4.2 Rayleigh-Bénard Convection Heat Transfer in a Water Layer 64
4.3 Natural Convection Heat Transfer in Water-Saturated Copper Foam with an Overlying Water Layer 66
4.3.1 Foam on the Hot Boundary 66
4.3.1.1 Heat Transfer Results and Nu_H, Ra_H Correlations 66
4.3.1.2 Heat Transfer Correlations for Foam on the Hot Boundary Alone 72
4.3.2 Foam on Both Boundaries 75
CHAPTER 5 CONCLUSIONS AND RECOMMENDATIONS 83
REFERENCES 88
APPENDIX A UNCERTAINTY ANALYSIS 93
A.1 Uncertainty in Temperature Measurement 94
A.1.1 Estimate of Thermocouple Bias Error 94
A.1.2 Estimate of Mean Temperatures 97
A.1.3 Temperature Uncertainty Associated with Temperature Measurement - Temporal Variations 98
A.1.4 Temperature Uncertainty Associated with Temperature Measurement - Spatial Variations 100
A.1.5 Temperature Uncertainty Associated with Temperature Measurement – Total Uncertainty 100
A.1.6 Uncertainty in the Temperature Difference Across Hot and Cold Plate 101
A.2 Uncertainty Power Input 101
A.2.1 Uncertainty in Primary Heater Power 102
A.2.1.2 Heater Electrical Resistance Uncertainty 103
A.2.2 Uncertainty in Heat Loss Calculation 104
A.3 Uncertainty in Porosity 104
A.4 Uncertainty in the Permeability and Forchheimer (Drag) Coefficient 106
A.5 Uncertainty in Effective Thermal Conductivity 108
A.6 Uncertainty in Nusselt number 110
A.7 Uncertainty in Rayleigh number 110
A.8 Uncertainty in Nusselt Number for Water Alone 111
A.9 Uncertainty in Enhancement Factor 112
APPENDIX B HEAT LOSS CALCULATIONS 113
APPENDIX C MEASURED EFFECTIVE CONDUCTIVITY 116
APPENDIX D HYPOTHESIS TESTING 121
D.1 Hypothesis Testing Background for Comparing the Means of Independent Samples with Unequal Variances 121
D.2 Hypothesis Testing for Current Results 123
D.2.1 Results of Hypothesis Testing 124
APPENDIX E FLUID PROPERTY CORRELATIONS 125

LIST OF TABLES

Table 2.1	Description of terms in porous media momentum equation [27].	9
Table 2.2	Results of Kathare et al. [14] for natural convection in saturated copper foam with an overlying fluid layer. Configuration is referenced to Figure 2.12.	23
Table 3.1	Summary of experiments.	42
Table 3.2	Thermocouple locations.	48
Table 4.1	Comparison of present results with the upper and lower theoretical limits, the models of Calmidi and Mahajan [29], Bhattacharya et al. [30], and the experimental work of Kathare [32].	60
Table 4.2	Summary of pressure drop testing and foam samples for which the results of each test are used.	63
Table 4.3	Comparison of current permeability and drag coefficient with previously published values.	63
Table 4.4	Summary of copper metal foam properties.	64
Table 4.5	Comparison of Nu_H, Ra_H, correlation for Rayleigh-Bénard convection, in a cylindrical enclosure filled with water, to [13] and [38].	65
Table 4.6	Result of hypothesis testing to determine if variation in Nusselt number with changing η is statistically significant.	70
Table A.1	Results of thermocouple calibration using platinum RTD as reference standard. RTD measurements are taken before (#1) and after (#2) thermocouple measurements. Two thermocouples, TC_1 and TC_2, were used for calibration.	95
Table A.2	Resolution and accuracy of voltage measurement	102
Table A.3	Uncertainty associated with DAQ equipment for voltage measurement.	103
Table B.1	Summary of one dimensional heat loss components.	115
Table C.1	Measured and corrected effective conductivities.	119
Table C.2	Average of measured and corrected effective conductivities.	120
Table C.3	Comparison of present results with theoretical limits, the correlations of Calmidi and Mahajan [29], and Bhattacharya et al. [30], the manufacturer's estimate [25] and the experimental work of Kathare [32].	120
Table D.1	Results of hypothesis testing.	124
Table E.1	Properties of water at 101.325 kPa over the temperature range 15 - 35 °C.	125

LIST OF FIGURES

Figure 2.1	Foam structure viewed at three different scales. Dimensions in mm.	5
Figure 2.2	Ligament cross-section as a function of porosity [25].	6
Figure 2.3	Specific surface area as a function of pore density and porosity for ERG Duocel metal foams [25].	6
Figure 2.4	Apparatus Phanikumar and Mahajan for natural convection in metal foams [10].	13
Figure 2.5	Apparatus for studying Rayleigh-Bénard equivalent convection in an enclosure filled with porous media.	16
Figure 2.6	Medium Nusselt number versus medium Rayleigh number for Rayleigh-Bénard equivalent convection in an enclosure filled with copper foam along with a correlation for a packed bed of low conductivity spheres attributed to Elder [33]. Plot is from Kathare et al. [13].	17
Figure 2.7	Medium Nusselt number as a function of medium Rayleigh number and Pr_p for Rayleigh-Bénard equivalent convection in an enclosure filled with copper foam. $R^2 = 0.96$ [13].	19
Figure 2.8	Nusselt number versus Rayleigh number for water-saturated 10 and 20 PPI copper foam. Plot is from Kathare et al. [13].	19
Figure 2.9	Enhancement in heat transfer over a water layer for Rayleigh-Bénard equivalent convection in an enclosure filled with copper foam. Plot is from Kathare et al. [13].	20
Figure 2.10	Medium Nusselt number as a function of medium Rayleigh number P_{rp} and inverse conductivity ratio for Rayleigh-Bénard equivalent convection in an enclosure filled with copper and RVC foam [37].	21
Figure 2.11	Apparatus for studying Rayleigh-Bénard equivalent convection in an enclosure partially filled with porous media.	23
Figure 2.12	Two configurations of the experimental apparatus of Kathare et al. [14].	23
Figure 2.13	Representative streamline pattern and isotherms for $\eta < 0.9$. For the case shown, $\eta = 0.5$, $Ra_m = 20 \times Ra_{m,c}$ [16].	26
Figure 2.14	Nusselt number variation with dimensionless porous height and medium Rayleigh number [16]. Numerical results are for an enclosure filled and partially filled with 3 mm diameter glass beads saturated in water or a mixture of water and glycerin.	26
Figure 2.15	Variation in Nusselt number for increasing medium Rayleigh number [17]. Dimensionless porous height is fixed at $\eta \approx 0.9$. Numerical results are for an enclosure filled and partially filled with 3 mm diameter glass beads saturated in water or a mixture of water and glycerin.	28
Figure 2.16	Streamlines and isotherms for $Ra_H \approx 10^5$, $Da = K/H^2 = 10^{-4}$. The enclosure is half filled with porous media. The numerical study considers low conductivity porous media saturated in water ($Pr = 7$ and $\alpha_f/\alpha_m = 1$). From Poulikakos [18].	29
		30

Figure 2.17 Effect of porous layer height on Nusselt number. $Ra_H = 10^5$, H/L = 0.5, $Da = K/H^2 = 10^{-4}$. The numerical study considers low conductivity porous media saturated in water (Pr = 7 and $\alpha_f/\alpha_m = 1$) [18].

Figure 2.18 Effect of Rayleigh number on heat transfer. H/L = 0.5, $\eta = 0.5$. The numerical study considers low conductivity porous media saturated in water (Pr = 7 and $\alpha_f/\alpha_m = 1$) [18]. 30

Figure 2.19 Effect of aspect ratio on Nusselt number. $Ra_H = 10^5$, $\eta = 0.5$, $Da = K/H^2 = 10^{-4}$. The numerical study considers low conductivity porous media saturated in water (Pr = 7 and $\alpha_f/\alpha_m = 1$). [18]. 32

Figure 2.20 Effect of aspect ratio on Nusselt number. $Ra_H = 10^5$, $\eta = 0.5$, $Da = K/H^2 = 10^{-6}$. The numerical study considers low conductivity porous media saturated in water (Pr = 7 and $\alpha_f/\alpha_m = 1$) [19]. 33

Figure 2.21 Effect of porous layer height on Nusselt number, 12.7 and 25.4 mm acrylic beads saturated in silicon [20]. 35

Figure 2.22 Variation in heat transfer with Prandtl number for an enclosure partially filled with aluminum beads saturated in glycol, silicon, and "matching" silicon [22]. 36

Figure 2.23 Nusselt number versus Rayleigh number for 25.4 mm aluminum beads saturated in glycol. In the plot "pure" is when $\eta = 0$ and $\eta = 1.05$ is for a fully filled enclosure. From Prasad [22]. 37

Figure 2.24 Nusselt number variation with porous height for a cylindrical enclosure partially filled with glass beads saturated in water [23]. 38

Figure 3.1 Sketch of experimental apparatus showing two foam configurations, foam on the hot boundary (a), and foam on both boundaries (b). 42

Figure 3.2 Cross sectional view of experimental apparatus for heat transfer experiment (adapted from [32]). 43

Figure 3.3 Thermocouple locations on the isothermal plates. Only the outer thermocouples (D = 76.2 mm) were used on the hot plate. The cold plate used both the outer and inner sets of thermocouples. Dimensions are in mm. Figure from [32]. 45

Figure 3.4 Separator plate assembly. Dimensions are in mm. Figure from [32]. 46

Figure 3.5 Copper plate P_2 showing radial grooves for thermocouple mounting. Dimensions in mm. Figure from [32]. 47

Figure 3.6 Pressure drop apparatus for measuring permeability and drag coefficient. From [32]. 48

Figure 3.7 Flow chart of energy and data acquisition system. 49

Figure 3.8 Experimental data showing transient and steady regions. 51

Figure 3.9 Experimental apparatus showing four locations where one dimensional heat loss is assumed. Figure adapted from [32]. 55

Figure 4.1 Pressure drop results for 0.75 inch thick 10 PPI copper foam with $\phi = 0.88$. 61

Figure 4.2 Pressure drop results for 1 inch thick 10 PPI copper foam with $\phi = 0.92$. 62

Figure 4.3 Pressure drop results for 1 inch thick 5 PPI copper foam with $\phi = 0.89$. 62

Figure 4.4	Nusselt number versus Rayleigh number for Rayleigh-Bénard convection in a cylindrical enclosure using water.	64
Figure 4.5	Nusselt vs. Rayleigh number for 5 and 10 PPI foam on the hot boundary alone as a function of η. Shown with data of Kathare et al. for η = 1 [13], 0.66 and 0.33 [14]. Solid line is a correlation for water alone developed in the current study. Dashed line is a correlation for 5 PPI foam. Dash-dot line is a correlation for 10 PPI foam.	67
Figure 4.6	Enhancement in heat transfer as a function of Rayleigh number for 5 and 10 PPI foam with η = 0.25, 0.5, and 0.75 on the hot boundary alone. Data of Kathare et al. [13] for η = 1 with 10 and 20 PPI copper foam also shown.	71
Figure 4.7	Advection enhancement as a function of Rayleigh number for 5 and 10 PPI foam on the hot boundary alone with η = 0.25, 0.5, and 0.75. Data of Kathare et al. [13] for η = 1 with 10 and 20 PPI copper foam also shown.	72
Figure 4.8	Nusselt number versus product of Rayleigh number and Darcy number for 5 and 10 PPI foam on the hot boundary. Solid line is a correlation considering all data. The dashed lines show the confidence interval of the correlation.	74
Figure 4.9	Medium Nusselt number as a function of medium Rayleigh number and $Pr_{p,s}$ for 5 and 10 PPI copper foam on the hot boundary with a superposed fluid layer. Shown with the data of Kathare et al. [13] for 10 and 20 PPI copper foam filled enclosure. The dashed line is the trendline for the data of Kathare et al. [13].	75
Figure 4.10	Nusselt number versus Rayleigh number for 10 PPI foam on both boundaries as a function of η with data of Kathare et al. for η = 1 [13], 0.66 and 0.5 [14]. The correlation for water alone is shown as a solid line. The correlation for 10 PPI foam on both boundaries and η = 0.5 is shown with a dash-dot line. The correlation for 10 PPI foam on both boundaries and η = 0.75 is shown as a dashed line.	76
Figure 4.11	Enhancement in heat transfer as a function of Rayleigh number for η = 0.5 and 0.75 for 10 PPI foam on both boundaries. Data of Kathare et al. [13] for η = 1 with 10 and 20 PPI copper foam also shown.	79
Figure 4.12	Advection enhancement as a function of Rayleigh number for 5 and 10 PPI foam with η = 0.25, 0.5, and 0.75. Data of Kathare et al. [13] for η = 1 with 10 and 20 PPI copper foam also shown.	80
Figure 4.13	Medium Nusselt number as a function of medium Rayleigh number and $Pr_{p,s}$ for 10 PPI on both boundaries. Only the data with η = 0.5 and 0.75 are included in the correlation. The correlation is extended with the dashed line to cover the data range of Kathare et al. [13], with η = 1.	82
Figure A.1	Results of thermocouple calibration using platinum RTD as reference standard. Thermocouple temperature versus RTD temperature with equation of linear fit.	95
Figure A.2	Bias error in corrected thermocouple measurements as a function of corrected thermocouple temperature.	98

NOMENCLATURE

ã	specific surface area, A_s/V [m^2/m^3]
A_s	surface area [m^2]
A_c	cross sectional area [m^2]
A	aspect ratio, H/D [DIM];
c	specific heat [J/kg-K]
C_F	drag coefficient in Forchheimer term of porous media momentum equation [DIM]
D	diameter [m]
d	bead diameter [m]
d_l	metal foam ligament diameter [m]
d_p	pore diameter [m]
E	enhancement in heat transfer with foam over that of a water layer, $\frac{q_{foam}}{q_{fluid}}\Big\vert_{Ra_H}$
g	acceleration of gravity, 9.81 [m/s^2]
h	heat transfer coefficient [W/m^2-K]
H	total height of test section [m]
H_p	foam sample height [m]
K	permeability [m^2]
k_d	dispersion conductivity [W/m-K]
k_e	effective conductivity [W/m-K]
k_f	fluid thermal conductivity [W/m-K]
k_m	medium fluid conductivity [W/m-K]
$k_{m,s}$	medium fluid conductivity of the composite system [W/m-K]
m	mass [kg]
ΔP	pressure drop across metal foam sample [N/m^2]
PPI	pores per inch
Q	power input, heat transfer rate [W]
q	heat flux [W/m^2]
R	electrical resistance [Ω]
T	temperature [K]
T_c	temperature of cold plate [K]
T_h	temperature of hot plate [K]
T_i	temperature of interface between foam and fluid layer [K]
T_m	mean temperature of the hot and cold plate [K]
T_{s1}	temperature on the top of the separator plate [K]
T_{s2}	temperature on the bottom of the separator plate [K]

T_{mo} temperature on the outside of the acrylic cylinder in at the center of the test section [K]

T_{ho} temperature on the outside of the acrylic cylinder in the region of the hot plate [K]

T_{so} temperature on the outside of the acrylic cylinder in the region of the separator plate [K]

T_i interface temperature [K]

U velocity [m/s]

V volume [m^3], voltage [V]

Dimensionless

Nu_H Nusselt number based on total height and fluid properties, hH/k_f

Nu_m Medium Nusselt number, hH_p/k_m

$Nu_{m,s}$ Medium Nusselt number for the composite system, $hH/k_{m,s}$

Da Darcy number, K/H_p^2

Da_s Darcy number for the composite system, K/H^2

Ra_H Rayleigh number based on total height and fluid properties , $\frac{g\beta(Th-Tc)H^3}{\alpha_f \nu_f}$

Ra_m medium Rayleigh number, $\frac{g\beta(T_h-T_i)KH_p}{\alpha_m \nu_f}$

$Ra_{m,c}$ critical medium Rayleigh number for the onset of convection

$Ra_{m,s}$ medium Rayleigh number for the composite system, $\frac{g\beta(T_h-T_c)KH}{\alpha_{m,s} \nu_f}$

Re_{dp} Reynolds number based on pore diameter, Ud_p/ν_f

Pr Prandtl number, ν/α

Pr_m porous media Prandtl number, $\mu c_f/k_m$

Pr_p dimensionless group, $\frac{Pr_m}{C_F\sqrt{Da}}$

Pr_m porous media Prandtl number for the composite system, $\mu c_f/k_{m,s}$

Pr_p dimensionless group for the composite system, $\frac{Pr_{m,s}}{C_F\sqrt{Da_s}}$

Greek

α fluid thermal diffusivity, $k_f/\rho_f c_f$ [m^2/s]

α_m medium thermal diffusivity of porous layer, $k_m/\rho_f c_f$ [m^2/s]

$\alpha_{m,s}$ effective thermal diffusivity of composite system, $k_{m,s}/\rho_f c_f$ [m^2/s]

β volumetric coefficient of expansion, $(-1/\rho)\, d\rho/dT$ [K]

γ ratio of bead diameter to total height, d/H [DIM]

μ dynamic viscosity [Pa-s]

$\tilde{\mu}$ effective viscosity in the Brinkman term of porous media momentum equation

ν kinematic viscosity (momentum diffusivity) [m^2/s]

ϕ porosity [DIM]
ϑ volumetric flow rate (m^3/s)

Subscripts

c cold
f fluid
h hot
L loss
p primary

CHAPTER 1 INTRODUCTION

1.1. Motivation and Objectives

Metal foams are lightweight, rigid, and offer high specific surface area. Applications include use as a core structure for lightweight, high strength panels, and as a catalytic surface for chemical reactions. Metal foams are also of potential interest for heat transfer applications including electronics cooling [1 - 7]. Heat transfer can be potentially increased with highly conductive metal foams as heat is conducted through the ligaments and transferred to the saturating fluid through high specific surface area. A 2008 review of the literature relating to forced convection heat transfer in metal foam heat exchangers is provided by Mahjoob and Vafai [8]. Natural convection research is more scarce, but prior work has considered finned heat exchangers for passive cooling of electronics [9 - 12] and enclosures filled with metal foam [13, 14].

In 2008, Kathare and co-workers at the University of Minnesota measured natural convection in an enclosure with a horizontal layer of water-saturated copper foam heated from below [13]. The enclosure was filled with 92% porous foam of 10 and 20 pores per inch. Comparing the natural convection heat transfer with metal foam to that of a water layer alone, the metal foam enhanced heat transfer by 20 to 60%. The enhancement in heat transfer was attributed to the metal foam's high conductivity relative to that of water. The metal foam was found to suppress convection for $Ra_H < 7 \times 10^7$.

Kathare and co-workers also investigated natural convection in a horizontal layer of water-saturated foam with an overlying fluid layer [14]. The foam filled only a portion of the enclosure and was adjacent to either the hot boundary or both the hot and cold boundaries. A practical benefit of partially filled enclosures is that if a thin layer of foam

can provide similar enhancement in heat transfer as an enclosure fully filled with foam, the cost of the system is reduced. In a limited set of experiments, with 92% porous 10 PPI copper foam, Kathare et al. [14] found that when foam was placed on only the hot boundary and the enclosure was filled 33 and 66% with foam, heat transfer was enhanced by 12 and 15% over that of water alone. With foam on both boundaries and the enclosure filled with 50 and 66% foam, heat transfer was enhanced by 37 and 47% over that of a water layer alone. All four experiments were conducted at $Ra_H \approx 10^8$ based on the height of the enclosure. Aside from the work of Kathare et al. [14], to my knowledge there are no studies in the literature relating to natural convection in an enclosure with metal foam with an overlying fluid layer.

Three groups, Chen and Chen [15, 16], Kim and Choi [17], and Poulikakos et al. [18, 19], carried out numerical studies of natural convection in a horizontal layer of porous media with a superposed fluid layer using low conductivity porous media such as glass beads saturated in water or a mixture of water and glycol. Chen and Chen validated their results for the onset of convection. With different formulations for the porous media momentum equation and different numerical methods, there is significant variation in the heat transfer results and even the general trends of the numerical studies. Prasad et al. [20 - 22] performed flow visualization and experimentally investigated heat transfer in fluid superposed layers of glass, acrylic and aluminum beads saturated in silicon and glycol. The authors presented Nusselt number-Rayleigh number correlations for different porous heights and provided plots of the variation of Nusselt number with changing porous height. The experiments with aluminum spheres, the only high conductivity porous media studied, showed enhancement in heat transfer with the addition of

aluminum spheres for the saturating fluids with lower Prandtl numbers (glycol, $Pr \approx 350$, and a modified silicon fluid, $Pr \approx 185$), but a decrease in heat transfer when saturated in high Prandtl number silicon fluid ($Pr \approx 6000$). The aluminum spheres were very large with the ratio of bead diameter to total height of 0.29 ($\gamma = d/H = 0.29$). Chandra [23] experimentally investigated glass beads saturated in water. His experiments with fluid alone did not follow previously published results for water alone, and fluctuations were observed in temperature measurements.

The present study expands the work of Kathare et al. [14] by experimentally investigating steady state natural convection heat transfer in a enclosure with a horizontal layer of copper foam and an overlying fluid layer, heated from below. It attempts to answer the question: Can an enclosure partially filled with copper foam provide similar enhancement to a fully filled enclosure? To answer this question, the effects of changing the pore density of the foam, foam placement (on one boundary or both), the relative height of foam in the enclosure, and the Rayleigh number, on natural convection heat transfer and the enhancement of heat transfer over a water layer alone are investigated.

CHAPTER 2 BACKGROUND AND LITERATURE REVIEW

This chapter begins with a brief background on metal foam structure and governing equations for the flow of fluid and energy through metal foams. A discussion of the literature relating to natural convection in a horizontal layer of metal foam in an infinite domain is provided for additional background on the behavior of metal foam in natural convection heat transfer. A review of relevant literature relating to Rayleigh-Bénard equivalent convection heat transfer in saturated porous media and in saturated porous media with a superposed fluid layer is then provided.

2.1 Metal Foams Background

2.1.1 Porosity, Pore Density, Specific Surface Area and Foam Structure

Open cell metal foams are a subset of porous media identified by a network of rigid ligaments, creating a series of interconnected polyhedrons. The open cells allow fluid to flow through the metal foam. Figure 2.1 shows the structure of metal foams ranging from the microscale to the macroscale. Note the polyhedral shape of the individual cells. A defining characteristic of metal foam, and porous media in general, is the porosity. Porosity, ϕ, is the fraction of the total volume that is occupied by void space [24]. Metal foams typically have porosities greater than 0.9. Metal foams are also identified by their relative density; the ratio of the mass of the metal foam to the mass of the metal foam would be if it were a solid block of the same material [25]. The relative density is $1 - \phi$. Another distinguishing feature is the pore density (typically expressed in pores per inch, PPI), and the shape and size of the ligament cross-section. Pore density can be approximated by Eq. (2.1) where d_l and d_p are the average fiber and pore diameter

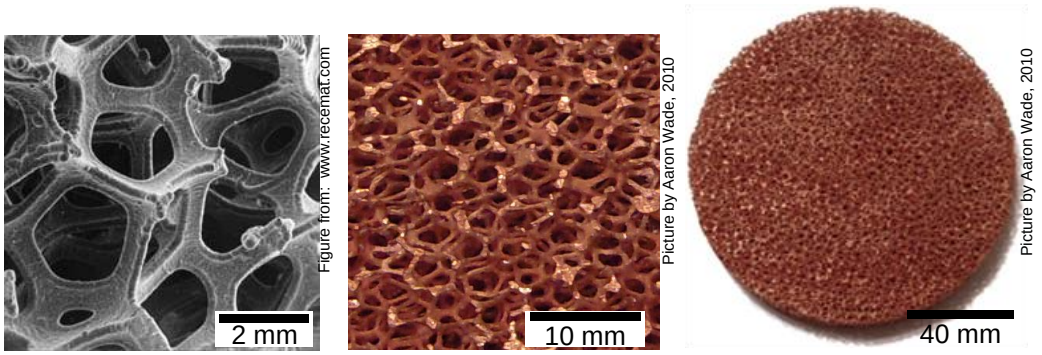

Figure 2.1. Foam structure viewed at three different scales. Dimensions in mm.

$$\text{PPI} \approx \frac{0.0254}{d_l + d_p} \tag{2.1}$$

of the foam, in meters. The pore density is a measure of how finely the raw material is divided, and metal foams with higher pore density have smaller size pores [25]. The shape and size of the ligament cross-section is a function of porosity and pore density. Figure 2.2 illustrates the effect of relative density on the shape of ligament cross-section. As the porosity decreases, the cross-sectional area of the ligaments increases and becomes more circular. Metal foams with higher pore density have smaller diameter ligaments.

Metal foams have high specific surface area, $\tilde{a} = A_s/V$. Figure 2.3 is a plot of the specific surface area as a function of pore density (in PPI) and porosity for aluminum foam manufactured by ERG Aerospace. Specific surface area increases with decreasing porosity and increasing pore density.

Effective thermal conductivity of metal foams is a function of the foam material, porosity, pore density, and saturating fluid [25]. The effective thermal conductivity of

Figure 2.2. Ligament cross-section as a function of porosity [25].

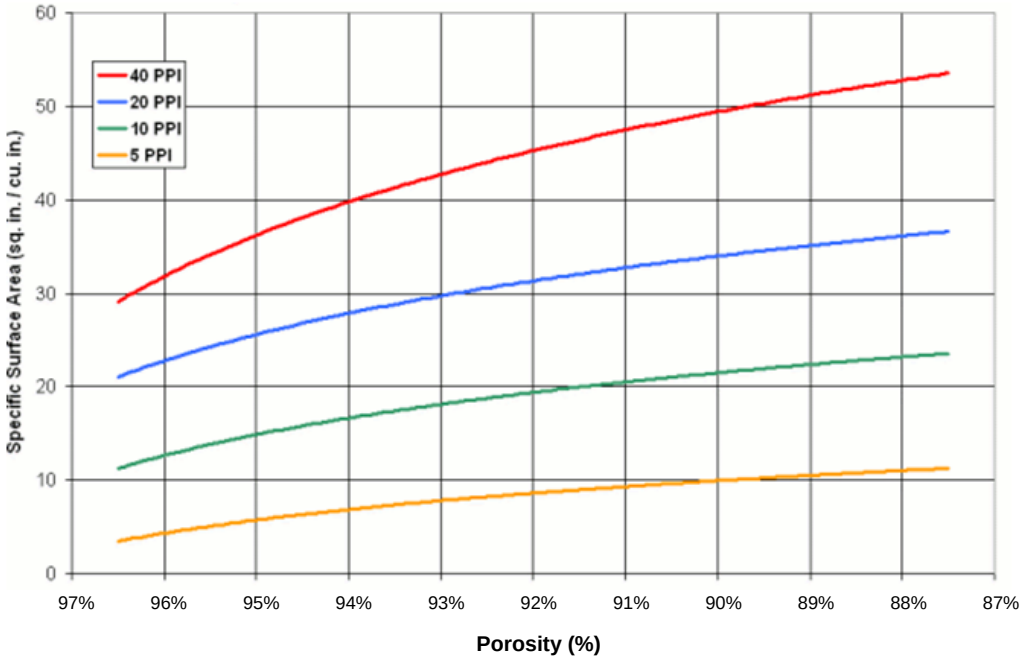

Figure 2.3. Specific surface area as a function of pore density and porosity for ERG Duocel metal foams [25].

metal foams is significantly reduced from the conductivity of the bulk material because of high porosity and the tortuous path created by the interconnected network of ligaments. As an example, the effective conductivity of air saturated aluminum foam is on the order of 5 W/mK [5], compared to a bulk conductivity of ~250 W/mK for aluminum.

2.1.2. Governing Equations for Modeling Porous Media and Metal Foam

Numerically solving the energy equation and the Navier-Stokes equations on the pore scale of the metal foam is possible if a representative pore is constructed. Assuming the foam is isotropic and homogeneous, the representative pore can be used to model heat and fluid flow though larger systems. This method has been shown to provide accurate predictions of pressure drop and effective thermal conductivity of fluid saturated foam [26]. However the approach may not be practical for macroscale problems, such as forced convection heat transfer in metal foam filled pipes, as boundary conditions have to be defined on the surface of every ligament of the metal foam and the bounding surfaces. If the metal foam is assumed to be isotropic and homogeneous, a volume averaging technique can be used to approximate the complexity of the metal foam structure. A finite volume, much larger than the pore scale, but still much smaller than the global scale of the problem, is constructed to represent the behavior of the entire porous medium. In this method, global parameters, such as effective thermal conductivity and permeability as a measure of viscous resistance to flow through the medium, are determined.

2.1.3. Conservation of Momentum

The average velocity can be defined with respect to the volume of void space V_f (the volume through which the fluid actually flows) or the total volume of the porous media V_m. The intrinsic velocity is determined with reference to the volume of the void space. The Darcy velocity is referenced to the total volume. The two definitions of velocity are related by the porosity, (Darcy Velocity) = ϕ × (Intrinsic Velocity) [24]. In this thesis, the Darcy velocity is used to describe fluid flowing through metal foam.

The idea of volume averaging is to create macroscopic momentum equations, starting with the Navier Stokes equations [27]. Due to the complex flow paths, this method creates a large number of macroscopic unknowns that represent the microscopic behavior of the flow at the pore level. The unknowns must be determined through experiment. In the same manner, semi-empirical momentum equations have been developed that attempt to represent the pore scale flow with macroscopic variables.

For steady, one dimensional flow through a loosely packed, uniform, rigid, isotropic solid matrix, Darcy found the pressure gradient to be proportional to the flow rate and viscosity [24]. The constant of proportionality, the permeability (K), is a measure of the microscopic viscous shear stress on the particles or struts making up the solid portion of the porous media. For isotropic porous media, the Darcy equation is:

$$-\nabla p = \frac{\mu}{K}\mathbf{U} \tag{2.2}$$

The Darcy equation is valid for fully developed flow with low pore-diameter Reynolds numbers ($Re_{dp} < 1$), and in situations when the viscous stress from the bulk media is much greater than the shear stress from the bounding surfaces [24]. Kaviany [27] provides a semi-empirical momentum equation as a series of extensions of the Darcy equation. The additional terms account for macroscopic flow development (convective term), macroscopic viscous shear stress at bounding surface (Brinkman term), and microscopic inertial force from flow separation at the solid surfaces of the porous media (Forchheimer term). For constant fluid properties, the full equation is given by

$$\underbrace{\frac{\rho_f}{\phi}\left(\frac{\partial \mathbf{U}}{\partial t} + \mathbf{U}\cdot\nabla\mathbf{U}\right)}_{\text{convective term}} = -\underbrace{\nabla p}_{\substack{\text{pressure}\\ \text{gradient}}} - \underbrace{\frac{\mu_f}{K}\mathbf{U}}_{\substack{\text{Darcy}\\ \text{term}}} + \underbrace{\frac{\tilde{\mu}}{\phi}\nabla^2\mathbf{U}}_{\substack{\text{Brinkman}\\ \text{term}}} - \underbrace{\frac{C_F}{K^{1/2}}\rho_f|\mathbf{V}|\mathbf{V}}_{\substack{\text{Forchheimer}\\ \text{term}}} + \underbrace{\rho\mathbf{F}}_{\substack{\text{body}\\ \text{force}}} \tag{2.3}$$

Table 2.1. Description of terms in porous media momentum equation [27].

Common Name	Equation	Description
Convective term	$\frac{\rho_f}{\phi}\left(\frac{\partial \mathbf{U}}{\partial t} + \mathbf{U}\cdot\nabla\mathbf{U}\right)$	Macroscopic inertial force, macroflow– development term
Pressure gradient	∇p	Pressure gradient
Darcy term	$\frac{\mu_f}{K}\mathbf{U}$	Microscopic viscous shear stress
Brinkman term	$\frac{\tilde{\mu}}{\phi}\nabla^2\mathbf{U}$	Macroscopic viscous shear stress due to bounding surface (wall effects)
Forchheimer Term	$\frac{C_F}{K^{1/2}}\rho_f\lvert\mathbf{U}\rvert\mathbf{U}$	Microscopic inertial force, microflow– development term
Body force	$\rho\mathbf{F}$	Gravitational force

As a reference, Table 2.1 provides a brief description of each term. The porous medium is assumed to be isotropic, meaning the permeability, K, is a scalar. The effective viscosity in the Brinkman term, $\tilde{\mu}$, asymptotes to the fluid viscosity for high porosity porous media such as metal foams ([27] p. 97). The drag coefficient, C_F, in the Forchheimer term is a measure of drag due to flow separation. The general form of Eq. (2.3) is widely used to account for the non-Darcy effects discussed above.

Often negligibly small, the Brinkman term can be significant for the high porosities found in metal foams [24]. The Brinkman term also raises the order of the differential equation and allows for a no slip condition at boundaries and the inclusion of a macroscopic boundary layer.

If body forces are significant, the variation of density with temperature in the body force term cannot be neglected. Known as the Boussinesq approximation, the simplest method of maintaining the assumption of constant properties, while allowing for variation in density with temperature, is to assume a linear relationship between the two quantities. The fluid density is then expressed as $\rho_f = \rho_0[1 - \beta(T - T_0)]$, where ρ_0 is the density at the reference temperature T_0, and β is the volumetric coefficient of expansion, $(-1/\rho)\, d\rho/dT$, at constant pressure [24].

Using a simplified momentum equation, the permeability, K, and drag coefficient, C_F, can be determined experimentally. In a numerical study of forced convection in porous media, Vafai and Tien [28] state that the boundary effect described by the Brinkman term, though potentially important for heat transfer, has a negligible effect on the flow field. For one dimensional, steady flow, neglecting the convective term, the Brinkman term and body force term, the momentum equation for flow inside porous media becomes

$$\frac{\Delta P}{H_p} = -\frac{\mu_f}{K} U - \frac{C_F}{K^{1/2}} \rho_f U^2 \tag{2.4}$$

where $\Delta P/H_p$ is the pressure drop across a sample of thickness H_p, μ_f is the viscosity of the fluid, ρ_f is the density of the fluid, U is the Darcy velocity, K is the permeability, and C_F is the drag coefficient. If the velocity and pressure drop across a sample are measured and fluid properties are known, the permeability and drag coefficient of the porous media can be determined by plotting $\Delta P/H_p$ versus U and fitting a second order polynomial to the data.

2.1.4. Conservation of Energy

Often, for simplicity, the solid and fluid phases are assumed to be in local thermal equilibrium (LTE). If the two phases have similar thermal diffusivities and convective heat transfer between the two phases is assumed large, the assumption of LTE is reasonable. However, in the case of natural convection in high conductivity metal foams saturated in water, heat transfer coefficients are small and the diffusivity ratio is far from unity. Heat is conducted through the solid matrix and is transferred by natural convection to the fluid. In this situation the two phases of a porous medium are in local thermal non-equilibrium (LTNE), and a two equation energy model is necessary to account for thermal transport in each phase. A semi-empirical model is recommended by Calmidi and Mahajan [1] and was utilized by Lu, Zhao and Tassou [2, 3] in a study of forced convection flow through metal foam filled pipes and counter flow heat exchangers. For LTNE, the steady energy equations for the solid and fluid phases are

$$0 = \underbrace{\nabla \cdot (k_{se} \nabla T_s)}_{\substack{\text{spatial gradient of} \\ \text{solid temperature}}} - \underbrace{h_{sf} \tilde{a} (T_s - T_f)}_{\substack{\text{heat transfer between} \\ \text{solid and fluid phases}}} \tag{2.5}$$

$$\underbrace{\rho_f c_f \mathbf{V} \nabla T_f}_{\substack{\text{thermal energy} \\ \text{convected with} \\ \text{bulk flow}}} = \underbrace{\nabla \cdot [(k_{fe} + k_d) \cdot \nabla T_f]}_{\substack{\text{spatial gradient of} \\ \text{fluid temperature}}} + \underbrace{h_{sf} \tilde{a} (T_s - T_f)}_{\substack{\text{heat transfer between} \\ \text{solid and fluid phases}}} \tag{2.6}$$

The energy equations account for spatial gradients in temperature for both phases, thermal energy advected with the bulk flow, and couple the two phases with a heat transfer coefficient, h_{sf}. Radiation is assumed to be negligible. In the above equations, k_{se} and k_{fe} are the effective thermal conductivities of the solid and fluid phases. Using an analytical model for the effective conductivity of the foam/fluid combination, Calmidi

and Mahajan [1] determined the effective solid and fluid thermal conductivities by separately setting the fluid and solid conductivities to zero. Thermal dispersion, pore scale mixing due to the presence of the solid matrix, is represented by an enhanced thermal diffusion with a dispersion conductivity, k_d. If the solid matrix has a significantly higher conductivity than the saturating fluid, Calmidi and Mahajan [1] found dispersion effects to be negligible compared to thermal diffusion in the foam matrix. The heat transfer coefficient is augmented by the specific surface area of the solid-fluid interface, $\tilde{a} = A_{sf}/V$.

Calmidi and Mahajan [29] determined effective solid and fluid conductivities through a semiempicical model based on one dimensional conduction through a simplified saturated metal foam matrix. The model is compared to experiments with aluminum foam saturated in water and air, to determine empirical parameters. Bhattacharya et al. [30] improved upon the Calmidi and Mahajan model by including a broader range of porosities and solid conductivities, and developing a more accurate one dimensional model for conduction. A similar model for effective thermal conductivity is proposed by Boomsma and Poulikakos [31], assuming one dimensional conduction based on an idealized three dimensional foam structure, and using the same data as [29] for model calibration.

2.2. Natural Convection in Horizontal Layer of Metal Foam in an Infinite Domain

In 2002, Phanikumar and Mahajan [10] numerically and experimentally investigated natural convection in metal foam surround by an enclosure approximating an infinite domain (Figure 2.4). The numerical model considered the Darcy-Forchheimer-Brinkman form of the momentum equation and two energy equations that considered the

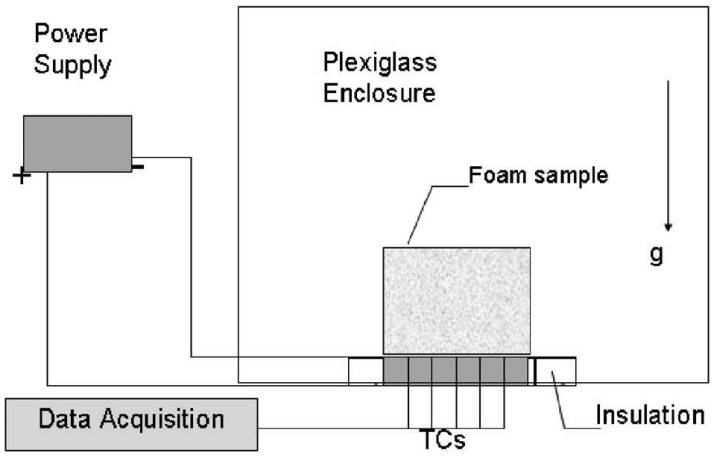

Figure 2.4. Apparatus Phanikumar and Mahajan for natural convection in metal foams [10].

effect of local thermal non-equilibrium (LTNE). They also used a single energy equation assuming local thermal equilibrium (LTE) to compare the accuracy of the LTE model with that of the LTNE model. The numerical model consisted of parameters for aluminum foam saturated in air and water, nickel foam saturated in water and reticulated vitreous carbon (RVC) foam saturated in air. RVC has a bulk conductivity of 8.5 W/mK. For their experimental study, aluminum foam of 5, 10, 20 and 40 PPI and $0.90 \phi < 0.96$ was saturated in air. For $1 \times 10^5 < Ra < 6 \times 10^5$ (Rayleigh number based on fluid properties and height of foam sample), the Nusselt number increases with decreasing pore density and porosity. As pore density decreases, the permeability increases and there is less resistance to flow, increasing convection. As porosity decreases, the fraction of solid material increases and the effective conductivity of the foam increases.

Their experimental data are in agreement with the LTNE model. The LTE model under-predicted heat transfer results. The difference in temperature between the two phases was as high as 60%. LTNE is a function of the Darcy number, a dimensionless

permeability, defined as $Da = K/H_p^2$ where K is the permeability and H_p is the height of the foam layer. Without providing specific numbers, the authors note that after examining a large number of cases the LTNE effects were more pronounced for the cases with higher Rayleigh and Darcy numbers where fluid velocities in the foam layer were larger. The effects of LTNE were also more significant for a large ratio of solid to fluid conductivity. For example, at $Ra = 4.1 \times 10^5$ and $Da = 7.7 \times 10^{-5}$, aluminum saturated in air ($k_s/k_f \approx 8400$) experienced a maximum temperature difference between the fluid and solid phases of 16%, while aluminum saturated in water ($k_s/k_f \approx 350$) experienced maximum temperature difference of 7.4%.

For the aluminum-air case, the thermal dispersion, or enhanced mixing due to the presence of the solid matrix, is negligible. However, the authors note that if the Darcy number is above 0.01 the effects of dispersion enhance heat transfer by 10%. Further increases in heat transfer, due to dispersion, would be observed by increasing the fluid Rayleigh number above 5×10^5 or decreasing the ratio of solid to fluid conductivity by using aluminum foam saturated in water.

Over a small range of fluid Rayleigh numbers ($10^5 - 5 \times 10^5$) heat transfer was enhanced using foam for all numerical cases except for the RVC foam saturated in air. Enhancement is greatest for the aluminum-water case with heat transfer enhanced by a factor of 16. When enhancement occurs it is primarily due to enhanced conduction as the foam provides resistance to flow which decreases convection heat transfer in the fluid. The enhancement is then seen as a balance between increased conduction in the solid phase and decreased convection in the fluid phase. The effective conductivity of the

solid must be large enough to overcome the reduced convection to enhance heat transfer. RVC foams do not have a high enough effective conductivity to enhance heat transfer.

In 2006, Bhattacharya and Mahajan [9] experimentally investigated horizontally and vertically positioned metal foam and a combination of metal fins and metal foam for passive cooling of electronics through natural convection. The study primarily focuses on using foam in combination with traditional heat sinks to enhance heat transfer, though a portion of the paper extends the results of Phanikumar and Mahajan [10] for horizontally positioned metal foam heated from below in an infinite domain. Assuming heat transfer will primarily be a function of the Rayleigh and Darcy numbers, the authors propose a correlation of the form

$$\mathrm{Nu_H} = \mathrm{CRa_H^m Da^n} \tag{2.7}$$

where the exponent for the Rayleigh number is defined for the case with no foam and the height of the foam is the length scale.

2.3. Rayleigh-Bénard Equivalent Convection Heat Transfer in Saturated Porous Media

Consider an enclosure of height, H, bounded on top and bottom by two parallel plates (Figure 2.5). The lower plate is heated, the upper plate is cooled, and the side walls are insulated. The temperature gradient between the two plates creates an unstable density gradient within the fluid. For a sufficiently large temperature difference, buoyancy associated with the density gradient is able to overcome viscous forces and thermal diffusion, creating fluid motion in the form of convective cells [32]. Known as Rayleigh-Bénard convection, this type of problem has been studied extensively for

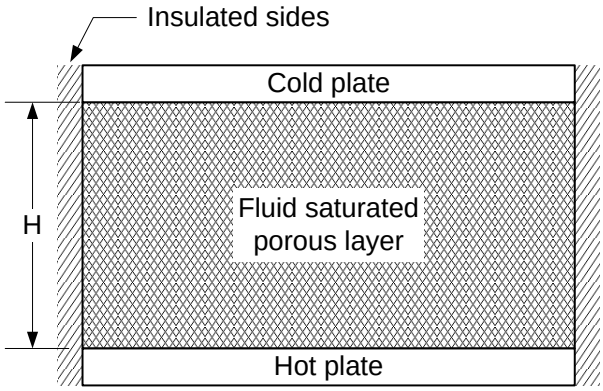

Figure 2.5. Apparatus for studying Rayleigh-Bénard equivalent convection in an enclosure filled with porous media.

enclosures filled with low conductivity porous media such as packed beds (e.g. [24], chapter 6). In 2008, Kathare et al. [13] studied this problem for 92% porous, 10 and 20 PPI copper foam saturated in water ($k_m \approx 9$ W/mK) with Darcy numbers on the order of 10^{-5}. Shown in Figure 2.6, the researchers found the natural convection in a horizontal layer of metal foam do not follow previously published correlations for natural convection in a packed bed of low conductivity spheres. Attributed to Elder [33], the correlation for Rayleigh-Bénard convection in a packed bed is $Nu_m = Ra_m/40$ where the medium Nusselt number is

$$Nu_m = \frac{hH}{k_m} = Nu_H \frac{k_f}{k_m} \tag{2.8}$$

where h is the heat transfer coefficient, k_m is the medium conductivity of the saturated porous media and k_f is the fluid conductivity and the medium Rayleigh number is

$$Ra_m = \frac{g\beta\Delta T H_p K}{\nu_f \alpha_m} = Ra_H Da \frac{k_f}{k_m} \tag{2.9}$$

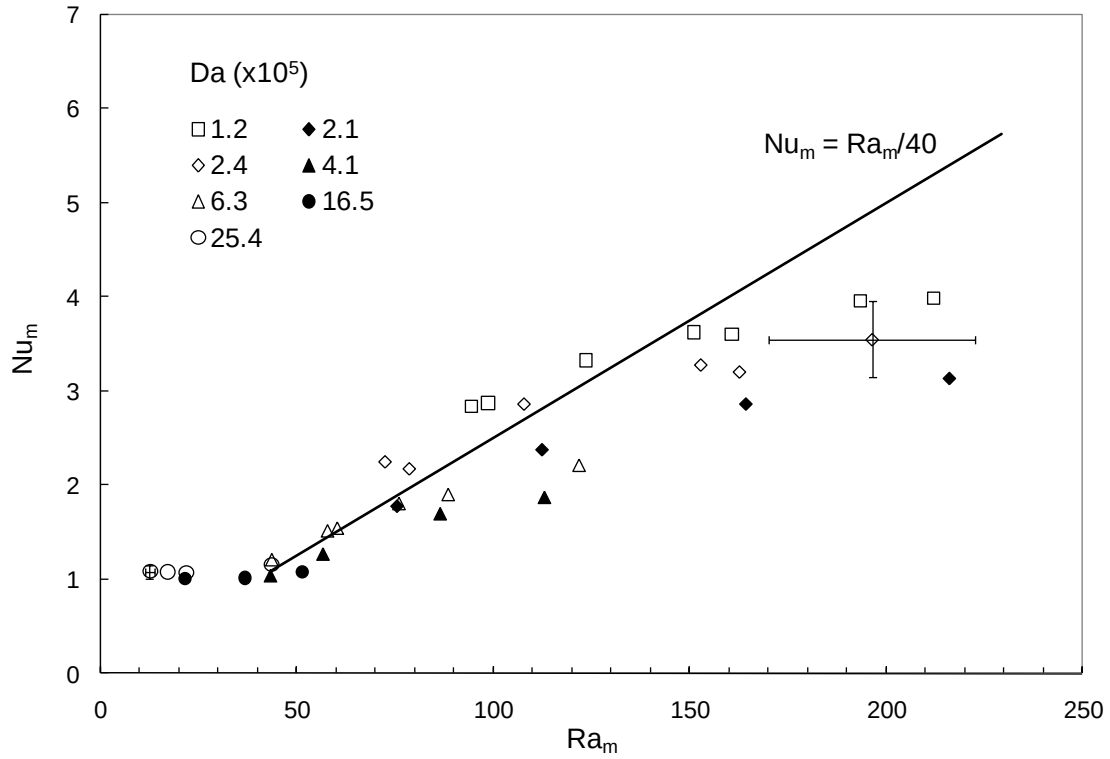

Figure 2.6. Medium Nusselt number versus medium Rayleigh number for Rayleigh-Bénard equivalent convection in an enclosure filled with copper foam along with a correlation for a packed bed of low conductivity spheres attributed to Elder [33]. Plot is from Kathare et al. [13].

The results of Kathare et al. [13] fall below the Elder correlation at high Rayleigh numbers. They suggest, though are not able to quantify, that the effects of LTNE may reduce heat transfer at high Rayleigh numbers as interfacial heat transfer between the foam provides additional resistance to overall heat transfer. The other proposed explanation is viscous boundary effects associated with the Brinkman term, which has been shown to be significant for highly porous media such as metal foam, and reduces heat transfer by suppressing flow. However, using a scale analysis the authors showed the ratio of Brinkman drag to Darcy drag was 0.008 or less for all cases, suggesting this explanation may not be valid. The authors also note that Darcy drag dominates over

Forchheimer drag, though Forchheimer drag is not insignificant. The ratio of the Forchheimer drag to Darcy drag ranged from 0.04 – 0.18 in their study.

Shown in Figure 2.7, Kathare et al. [13] correlated their data in a form suggested by the dimensional analysis of Wang and Bejan [34], where the medium Nusselt number is proportional to the medium Rayleigh number and a dimensionless parameter Pr_p

$$Pr_p = Pr_m \frac{H}{C_F\sqrt{K}} = \frac{Pr_m Da^{-1/2}}{C_F} \tag{2.10}$$

where $Pr_m = \mu c_f/k_m = Pr\,(k_f/k_m)$. The terms Ra_m and Pr_p fall out of the Darcy-Forchheimer equation when pressure is non-dimensionalized with $\mu\alpha_m/K$.

Kathare et al. [13] also estimated enhancement in heat transfer over that of a water layer, defining enhancement by

$$E = \frac{q_{foam}}{q_{fluid}}\bigg|_{Ra_H} \tag{2.11}$$

where q_{fluid} is determined using a correlation developed by Kathare et al. [13] for Rayleigh-Bénard convection with water alone, $Nu_H = 0.10Ra_H^{0.31}$. The heat transfer results, plotted in terms of the fluid Nusselt number and the fluid Rayleigh number, are shown in Figure 2.8. The results for enhancement are shown in Figure 2.9. With the enclosure filled with foam, heat transfer is by conduction below $Ra_H \approx 5 \times 10^6$ (corresponding to a critical porous media Rayleigh number of $Ra_m = 40$ [35]). However, the corresponding fluid Rayleigh number is substantially larger than the critical Rayleigh number for a fluid filled enclosure $Ra_H = 1708$ [36]. Therefore, below $Ra_H \approx 5 \times 10^6$, enhancement decreases with increasing Rayleigh number because the Nusselt number

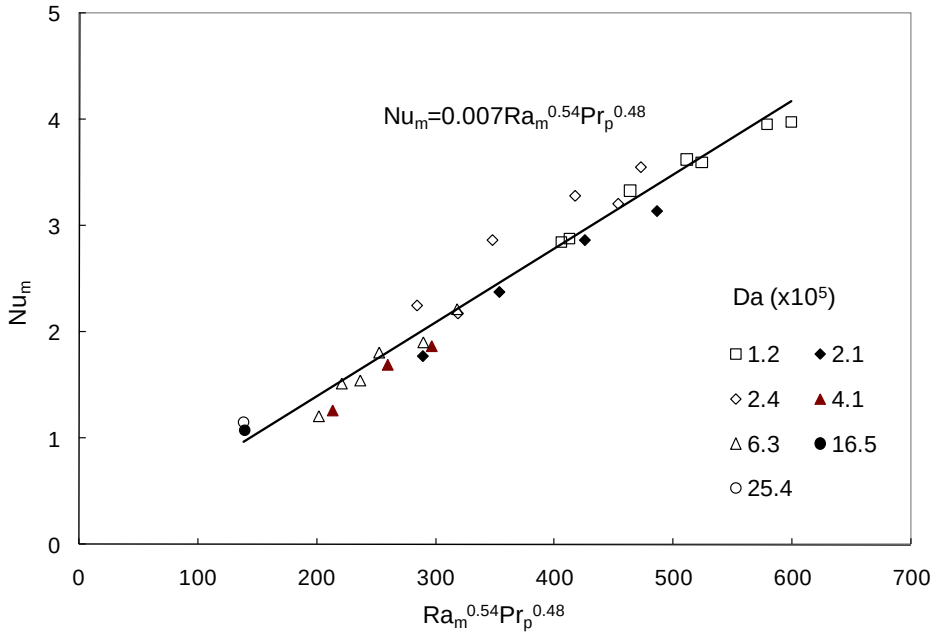

Figure 2.7. Medium Nusselt number as a function of medium Rayleigh number and Pr_p for Rayleigh-Bénard equivalent convection in an enclosure filled with copper foam. $R^2 = 0.96$ [13].

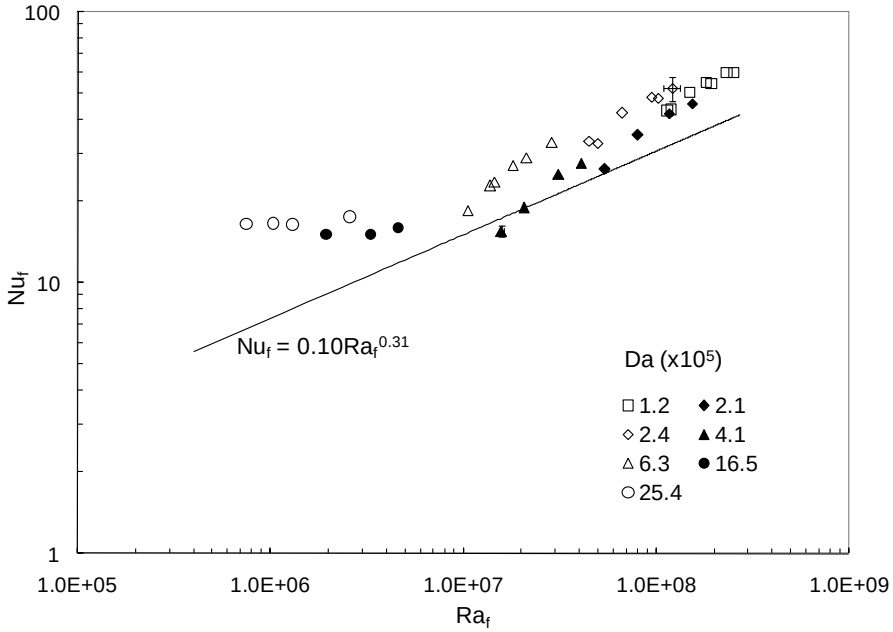

Figure 2.8. Nusselt number versus Rayleigh number for water-saturated 10 and 20 PPI copper foam. Plot is from Kathare et al. [13].

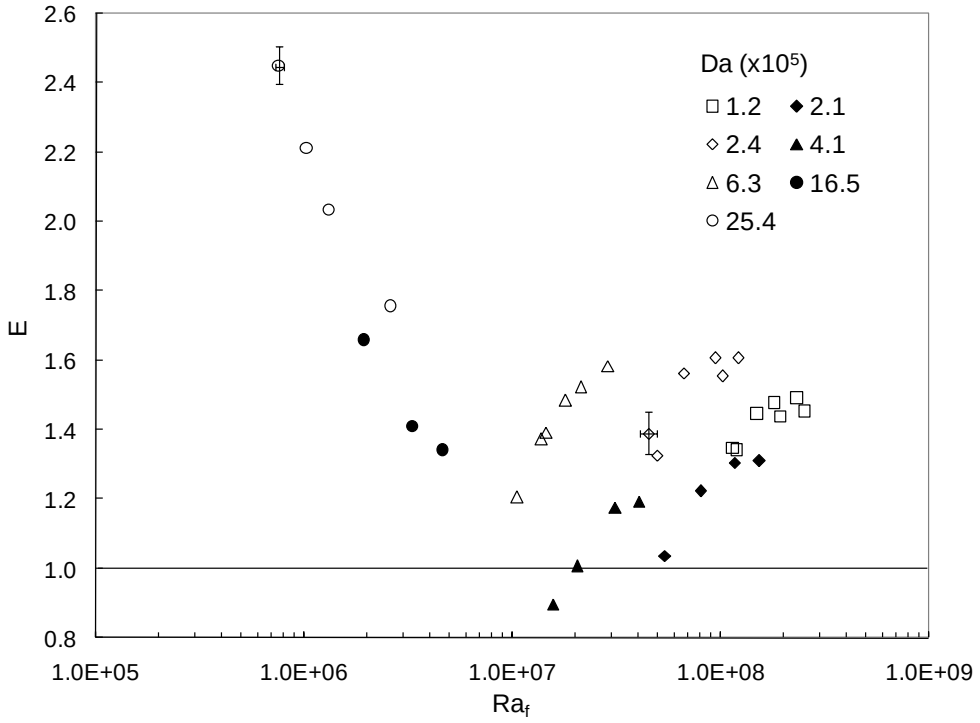

Figure 2.9. Enhancement in heat transfer over a water layer for Rayleigh-Bénard equivalent convection in an enclosure filled with copper foam. Plot is from Kathare et al. [13].

with foam is relatively constant with changing Rayleigh number (as it is in the conduction regime), while the Nusselt number for water alone increases with Rayleigh number (as it is in the convection regime). After the onset of convection in the foam layer, enhancement increases with increasing Rayleigh number as the foam layer suppresses fluid advection less for higher Rayleigh numbers. For the same Rayleigh number, foam layers with high Darcy number generally show greater enhancement as the suppression of convection is reduced for more permeable foams. The authors estimate the advection heat transfer as the total heat transfer minus the conduction heat transfer. Advection is suppressed for all but the highest Rayleigh numbers suggesting the primary

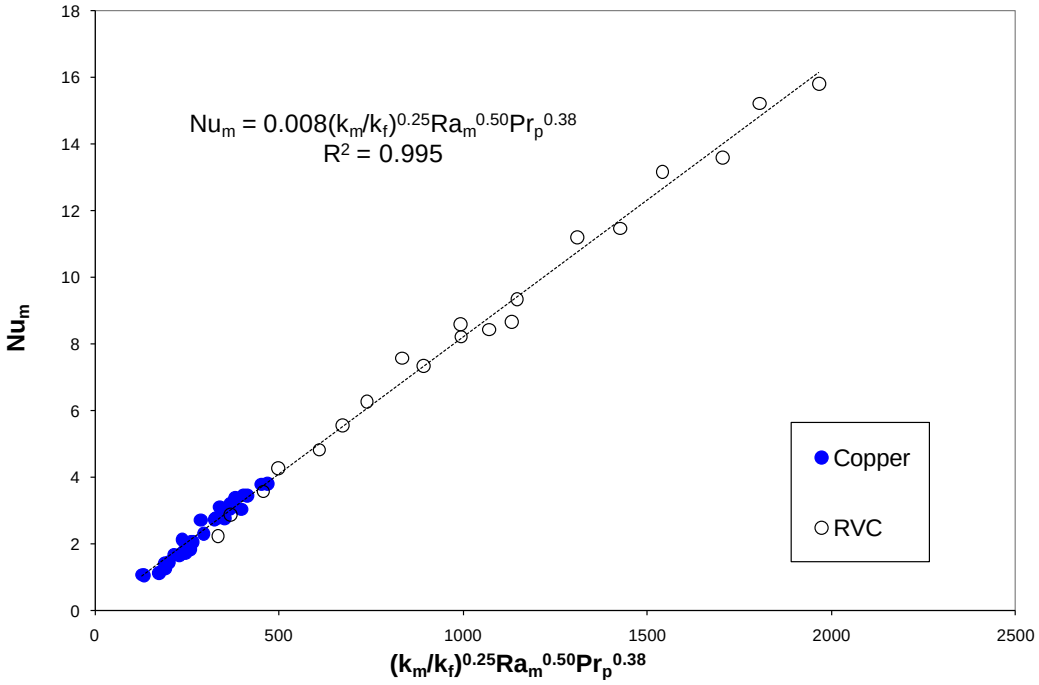

Figure 2.10. Medium Nusselt number as a function of medium Rayleigh number P_{rp} and inverse conductivity ratio for Rayleigh-Bénard equivalent convection in an enclosure filled with copper and RVC foam [37].

means of heat transfer enhancement is by conduction. At the high Rayleigh numbers, advection enhancement of up to 20% is observed. The effect of dispersion on heat transfer is estimated to be on the order of 1% of total heat transfer and is considered negligible. No other explanation is provided as to why metal foams would enhance advection heat transfer over a water layer alone.

Davidson et al. [37] expanded the work of Kathare et al. [13] to include low conductivity reticulated vitreous carbon (RVC) foam with $k_m \approx 0.7$ W/mK. The RVC foam yields lower Nusselt numbers as conduction is relatively weak in the solid phase. By introducing the ratio of medium to fluid conductivities, the copper foam results of Kathare et al. [13] ($k_m \approx 9$ W/mK) and Davidson et al. [37] were collapsed to a single correlation (Figure 2.10).

2.4. Rayleigh-Bénard Equivalent Convection Heat Transfer in Saturated Porous Media with a Superposed Fluid Layer

Rayleigh-Bénard convection heat transfer in an enclosure partially filled with porous media, such as that shown in Figure 2.11, offers unique challenges not found in forced convection systems or enclosures fully filled with porous media. If the enclosure is not fully filled with porous media, convection cells developed in the fluid region may or may not penetrate through the porous layer. Without penetration a stagnant region exists in the porous layer [16, 18, 19]. An enclosure partially filled with metal foam also limits the impact of the highly conductive foam by removing the direct conduction path between the two boundaries. Despite the potential hurdles, high conductivity metal foams saturated in water may significantly enhance heat transfer in partially filled enclosures because of their high permeability and large ratio of solid conductivity to fluid conductivity, k_s/k_f.

Kathare et al. [14] studied natural convection heat transfer in an enclosure partially filled with copper foam of porosity $\phi = 0.92$ and 10 PPI pore density. Shown in Figure 2.12, the researchers tested two configurations: (a) foam on the hot boundary alone and (b) foam on both the hot and cold boundary. Two experiments were performed for each configuration where $\eta = H_p/H$ was varied between experiments. All four experiments were conducted at a similar fluid Rayleigh number, $Ra_H \approx 10^8$. The authors use the enhancement factor defined in Eq. (2.11) to estimate enhancement in heat transfer with a foam layer over water alone. A summary of the experiments is shown in Table 2.2. For 10 PPI foam only on the hot boundary, configuration (a), enhancements of $E = 1.12$ and 1.15 were achieved for $\eta = 0.33$ and 0.66, respectively. When half the total

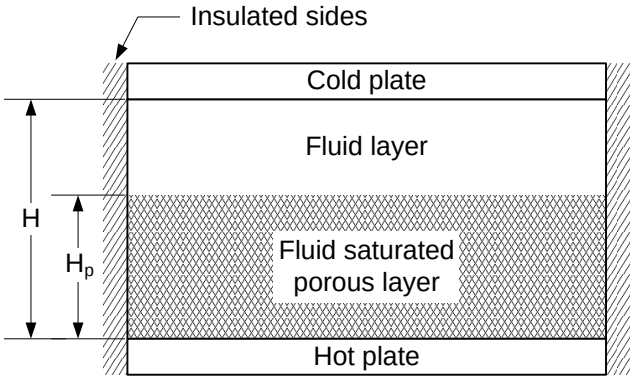

Figure 2.11. Apparatus for studying Rayleigh-Bénard equivalent convection in an enclosure partially filled with porous media.

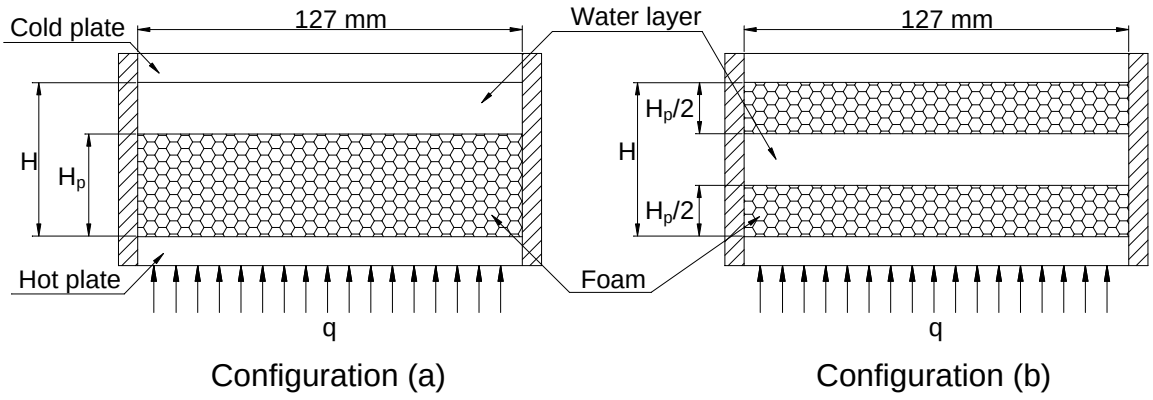

Figure 2.12. Two configurations of the experimental apparatus of Kathare et al. [14].

Table 2.2. Results of Kathare et al. [14] for natural convection in saturated copper foam with an overlying fluid layer. Configuration is referenced to Figure 2.12.

Exp. #	Configuration	Ra_H (10^{-8})	η	E
1	(a)	1.6	0.33	1.12
2	(a)	1.6	0.66	1.15
3	(b)	3.1	0.5	1.35
4	(b)	1.2	0.66	1.47
5	foam filled	2.5	1	1.48
6	foam filled	1.0	1	1.58

foam layer is placed on the cold boundary and half on the hot boundary, as in configuration (b), an enhancement of E = 1.35 was achieved for $\eta = 0.5$ and E = 1.47 with $\eta = 0.66$. Note that the enhancement with $\eta = 0.66$ and foam on both boundaries, E = 1.47, is similar to the two foam filled enclosure cases, E = 1.48 and E = 1.58.

With foam on one boundary, doubling the foam layer from $\eta = 0.33$ to $\eta = 0.66$ provides little additional enhancement, E = 1.12 to E = 1.15. However, keeping η fixed at 0.66 and changing the configuration, from foam on one boundary to foam on both boundaries, a significant increase in enhancement, from E = 1.15 to E = 1.47, is observed. The significant differences in enhancement with regard to configuration lead the authors to conclude that the boundary phenomenon is more important to heat transfer than the bulk phenomenon and an optimal foam thickness, on the order of the thermal boundary layer, exists. This prior study indicates that a relatively thin layer of foam may provide similar enhancement in heat transfer as a larger foam layer, or an enclosure completely filled with foam, depending on the configuration.

To my knowledge, the work of Kathare et al. [14] is the only published research for Rayleigh-Bénard equivalent convection in an enclosure partially filled with metal foam with an overlying fluid layer. Chen and Chen [15, 16], Kim and Choi [17], and Poulikakos et al. [18, 19] numerically investigated this problem for low conductivity porous media, such as glass beads, saturated in water or a mix of water and glycol. All of the numerical studies assume local thermal equilibrium between the solid and fluid phases. Prasad et al. [20 - 22] experimentally investigated natural convection with glass, acrylic and aluminum beads saturated in silicon and glycol, and Chandra [23] experimentally investigated glass beads saturated in water. As discussed in Section 2.3,

Kathare et al. [13] showed that the Rayleigh-Bénard equivalent convection heat transfer behavior of water-saturated copper foam, for an enclosure completely filled with foam, does not follow known heat transfer correlations for packed beds of spheres. Regardless, the porous media literature provides insight on the factors affecting natural convection heat transfer in water-saturated high conductivity foams with an overlying fluid layer.

In two papers, Chen and Chen [15 - 16] numerically investigated the onset of convection and supercritical convection in saturated porous media with a superposed fluid layer. Experiments and calculations are based on 3 mm diameter glass beads saturated in water or a mixture of water and glycerin. The porosity was fixed at 0.389, $Da = K/H_p^2 \approx 9 \times 10^{-6}$. The thermal diffusivity ratio, α_f/α_m, is 0.73. The authors applied the Darcy and Darcy-Brinkman-Forchheimer formulations for the momentum equation in porous media. The wavelength of the convection cells was fixed to the size of the convection cells at the onset of convection. Chen and Chen observe that convection is dominated in the fluid layer and almost completely absent in the porous layer for $\eta = H_p/H < 0.9$. This result is shown in Figure 2.13 for a medium Rayleigh number 20 times the critical medium Rayleigh number ($Ra_m = 0.162$) and $\eta = 0.5$. The plot on the left shows streamlines and the plot on the right shows isotherms. Very little flow is observed to penetrate the porous media and heat transfer in the porous layer is via conduction. When the enclosure is nearly filled with foam ($\eta \approx 0.9$), convection is initiated, and dominant in the porous layer. The effect of η on flow penetration is shown in Figure 2.14. For an enclosure completely filled or nearly filled with porous media ($\eta = 1$ and $\eta \approx 0.9$, respectively), convection exists throughout the enclosure and Nusselt

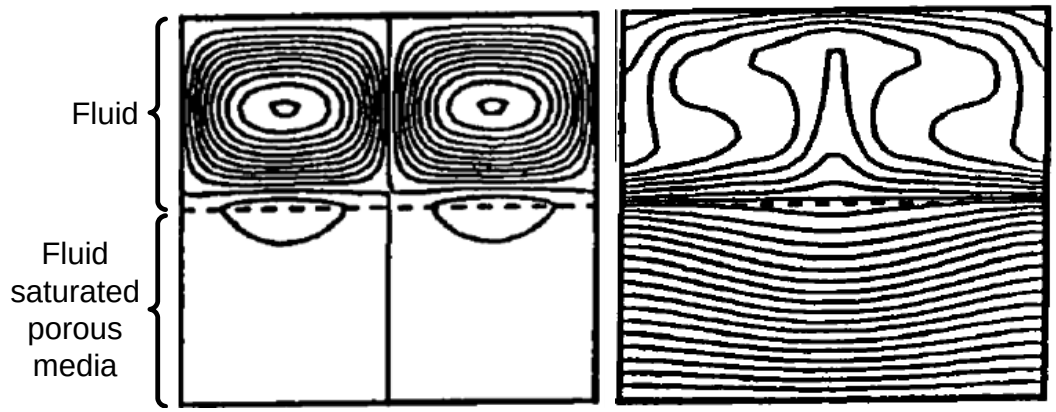

Figure 2.13. Representative streamline pattern and isotherms for $\eta < 0.9$. For the case shown, $\eta = 0.5$, $Ra_m = 20 \times Ra_{m,c}$ [16].

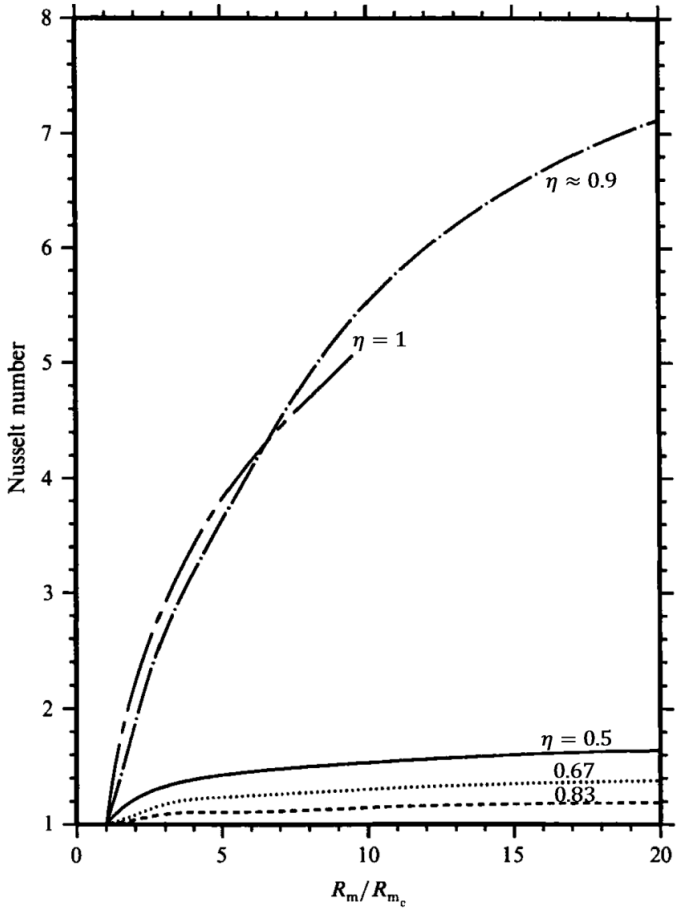

Figure 2.14. Nusselt number variation with dimensionless porous height and medium Rayleigh number [16]. Numerical results are for an enclosure filled and partially filled with 3 mm diameter glass beads saturated in water or a mixture of water and glycerin.

numbers are relatively high and increase with increasing Rayleigh numbers. For $0 < \eta < 0.83$, a sharp drop in the Nusselt number is observed compared to the completely or nearly filled case. The flow is mostly stagnant in the porous layer, and heat from the lower boundary is not advected to the upper boundary. The authors varied the Prandtl number but observed very little change in Nusselt number with Prandtl number.

Kim and Choi numerically investigated saturated porous media with a superposed fluid layer with the Darcy-Forchheimer-Brinkman momentum equation governing the porous layer [17]. The characteristics of the porous media are the same as in the Chen and Chen investigation [16]. Kim and Choi modified the aspect ratio (height/width, H/L) for each η to ensure the enclosure was wide enough to avoid restricting the convection cells. The results are very similar to the Chen and Chen investigation except the monotonic increase in Nusselt number with increasing Rayleigh number, shown in Figure 2.15, is not observed for $\eta \approx 0.9$. The Nusselt number fluctuates due to a changing number and size of convective cells with increasing Rayleigh number.

Poulikakos [18] numerically investigated natural convection in porous media with a superposed fluid layer in a square enclosure using a Darcy-Forchheimer-Brinkman form of the momentum equation for the porous layer. He combined the porous medium and fluid momentum equations into a single equation using a binary parameter that sets the porous media variables to zero in the fluid layer. Poulikakos et al. [19] investigated the same problem using the Darcy formulation and separate momentum equations for the porous and fluid layers. For both studies, $Pr = 7$ and $\alpha_f/\alpha_m = 1$. The authors state that the majority of convection takes place in the fluid region though more flow penetration is

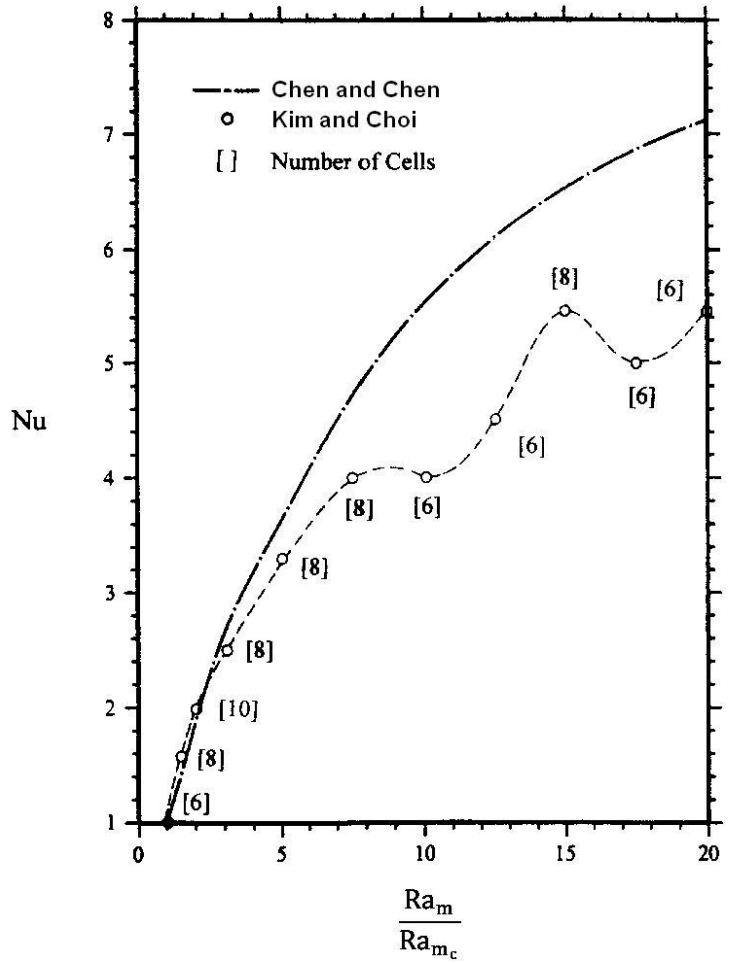

Figure 2.15. Variation in Nusselt number for increasing medium Rayleigh number [17]. Dimensionless porous height is fixed at $\eta \approx 0.9$. Numerical results are for an enclosure filled and partially filled with 3 mm diameter glass beads saturated in water or a mixture of water and glycerin.

observed than in the studies by Chen and Chen [16] and Kim and Choi [17]. This result is seen in Figure 2.16, which shows a plot of streamlines and isotherms for $Ra_H = 10^5$ ($\approx 10 \times Ra_{Hc}$), $Da = K/H^2 = 10^{-4}$, and $\eta = 0.5$. With the enclosure half filled with porous media, the flow penetrates into the porous layer with two symmetric convection cells. Convection is strongest and centered in the upper, fluid layer. For the isotherm plot there is a significantly larger stagnant region, where heat transfers mostly by conduction, in the porous layer than in the fluid layer.

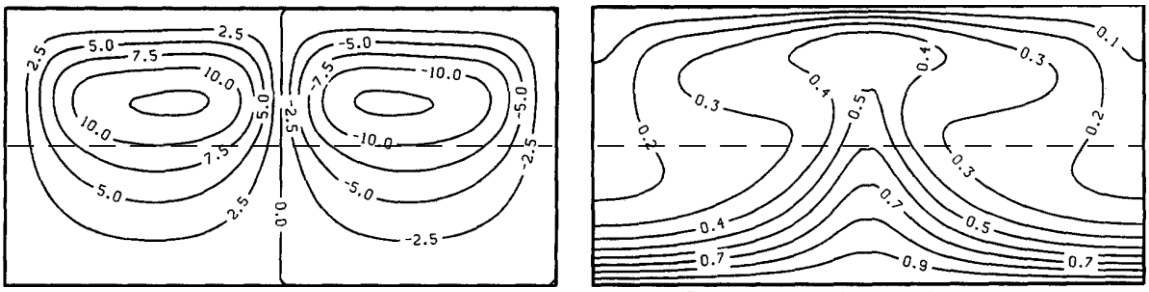

Figure 2.16. Streamlines and isotherms for $Ra_H \approx 10^5$, $Da = K/H^2 = 10^{-4}$. The enclosure is half filled with porous media. The numerical study considers low conductivity porous media saturated in water ($Pr = 7$ and $\alpha_f/\alpha_m = 1$). From Poulikakos [18].

The results of Poulikakos [18] also show the effect of changing porous height. Shown in Figure 2.17, the Nusselt number monotonically decreases with increasing porous height as flow is squeezed into a progressively smaller region near the top. The removal of heat from the base becomes more dependent on conduction through the porous layer and as η increases, the Nusselt number decreases. The flow becomes completely stagnant at $\eta \geq 0.75$ and heat is removed by conduction. The increase in Nusselt number for porous layer height above $\eta > 0.9$, when flow becomes dominate in the porous region, as observed by Chen and Chen [15, 16] and Kim and Choi [17], is not discussed in this paper.

The effect of the increasing Rayleigh number and Darcy number on Nusselt number, for a fixed dimensionless porous height, $\eta = 0.5$, is shown in Figure 2.18. For varying Rayleigh number (bottom scale), the Darcy number is $K/H^2 = 10^{-4}$. The Rayleigh number is 10^5 for varying Darcy number (top scale). The Nusselt number increases with increasing Rayleigh and Darcy numbers. Increasing the Darcy number reduces resistance to flow in the porous layer and the convection cell penetrates deeper into the porous

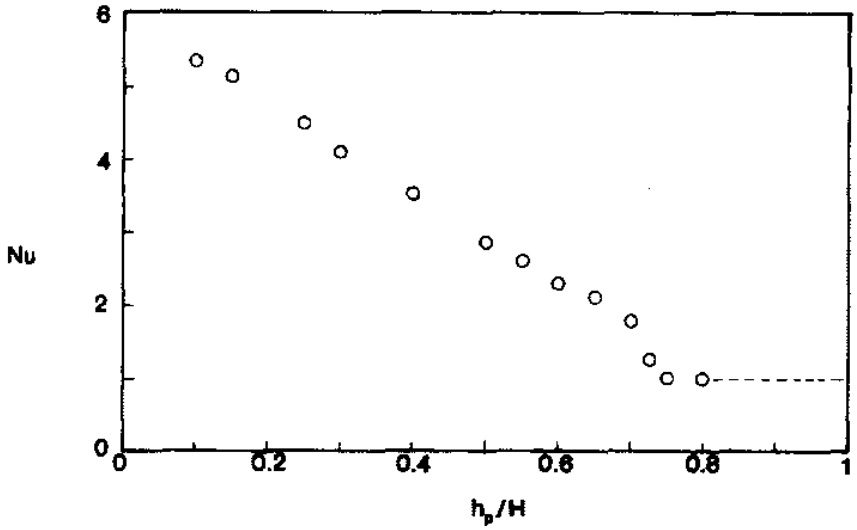

Figure 2.17. Effect of porous layer height on Nusselt number. $Ra_H = 10^5$, H/L = 0.5, $Da = K/H^2 = 10^{-4}$. The numerical study considers low conductivity porous media saturated in water (Pr = 7 and $\alpha_f/\alpha_m = 1$) [18].

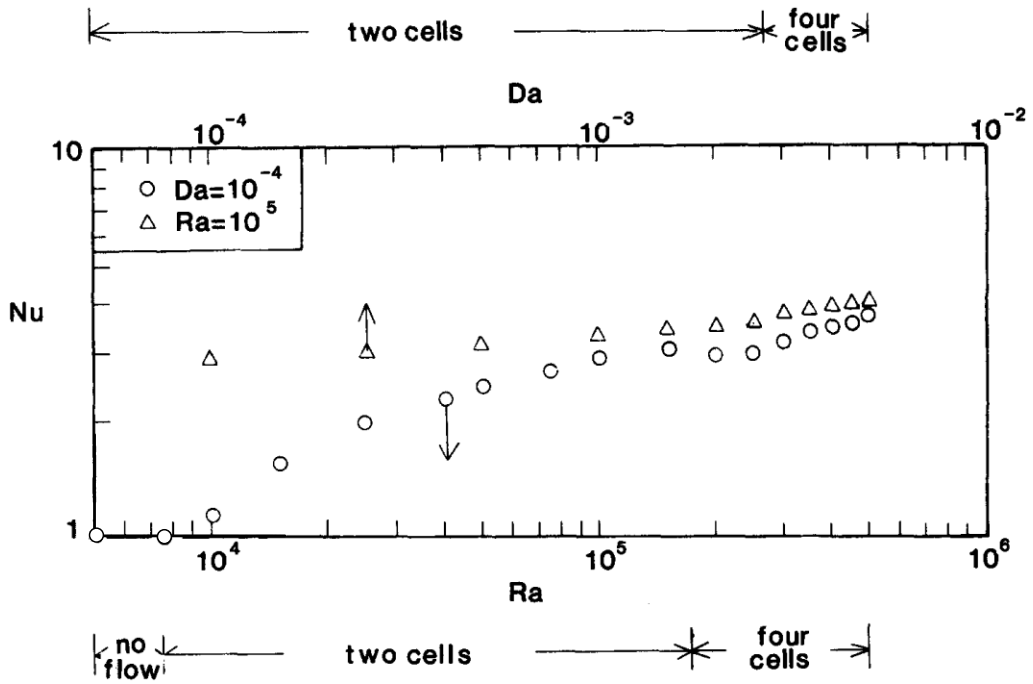

Figure 2.18. Effect of Rayleigh number on heat transfer. H/L = 0.5, $\eta = 0.5$. The numerical study considers low conductivity porous media saturated in water (Pr = 7 and $\alpha_f/\alpha_m = 1$) [18].

layer, enhancing heat transfer. At higher Rayleigh number the convection cells have higher velocity and penetrate deeper into the porous layer. The trend of increasing Nusselt number with increasing Rayleigh and Darcy numbers is not monotonic, however. When the Rayleigh number reaches $\sim Ra = 2 \times 10^5$ (for varying Rayleigh number and fixed Darcy number) and when the Darcy number reaches $\sim Da = 3 \times 10^{-3}$ (for varying Darcy number and fixed Rayleigh number), the number of convection cells double from two to four. However, after the cells double, each cell is less strong and penetrates less deeply into the porous region than before, resulting in a slight decrease in Nusselt number for increasing Rayleigh number or Darcy number. As the Rayleigh number or Darcy number continue to increase, the four cells increase in strength and the Nusselt number begins to increase again.

The Nusselt number decreases with increasing aspect ratio, A = H/L. However, the severity of the decrease in Nusselt number with increasing aspect ratio differs between the studies of Poulikakos [18] and Poulikakos et al. [19]. For both studies, $Ra_H = 10^5$ and $\eta = 0.5$. The difference in the two studies is the Darcy number. For [18], $Da = K/H^2 = 10^{-4}$. For [19], $Da = 10^{-6}$. Poulikakos [18] shows a slight, non-monotonic decrease in the Nusselt number with increasing aspect ratio as shown in Figure 2.19. Note that for a fixed number of convection cells, the Nusselt number reaches a maximum as the aspect ratio changes. At aspect ratios above each maximum value, the convection cells are compressed, increasing friction between the cells. Below this value, the convection cells are stretched, creating regions of relative stagnation. Continuing to

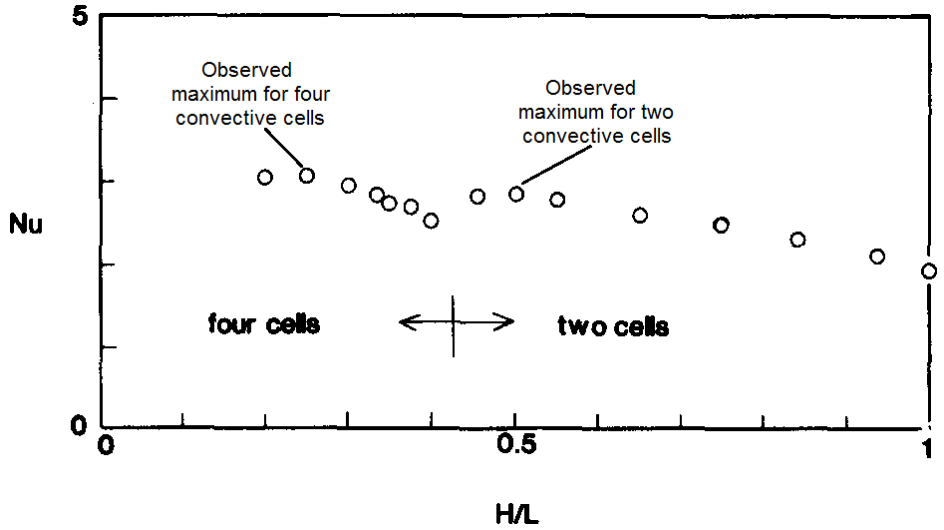

Figure 2.19. Effect of aspect ratio on Nusselt number. $Ra_H = 10^5$, $\eta = 0.5$, $Da = K/H^2 = 10^{-4}$. The numerical study considers low conductivity porous media saturated in water ($Pr = 7$ and $\alpha_f/\alpha_m = 1$). [18].

decrease the aspect ratio results in cell multiplication. Shown in Figure 2.20, Poulikakos et al. [19] observe a continual decrease in Nusselt number with increasing aspect ratio. The authors note that at H/L = 0.4, the rate of decrease in the Nusselt number becomes more dramatic as the side walls are close enough to interfere with, and slow down convection.

In three papers, Prasad et al. [20 - 22] present an experimental investigation of natural convection in porous media with superposed fluid layers consisting of glass, acrylic, and aluminum beads saturated in two types of silicon or glycol. The experiments were conducted in a cylindrical enclosure with a diameter of 178 mm and height of 89 mm (A = H/D = 0.5). The bead diameters ranged from 3 mm to 25.4 mm. For the 25.4 mm beads ($\gamma = d/H = 0.29$) four layers of beads completely fill the enclosure. A

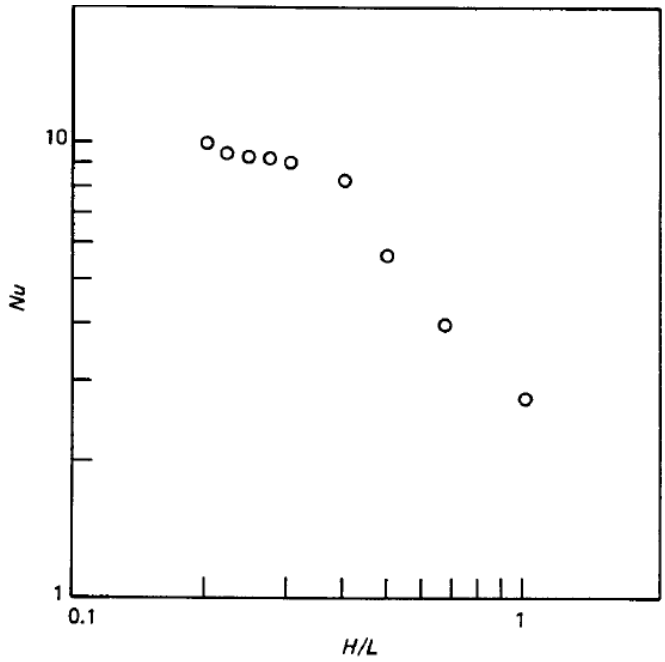

Figure 2.20. Effect of aspect ratio on Nusselt number. $Ra_H = 10^5$, $\eta = 0.5$, $Da = K/H^2 = 10^{-6}$. The numerical study considers low conductivity porous media saturated in water ($Pr = 7$ and $\alpha_f/\alpha_m = 1$) [19].

single layer of beads was used for the lowest dimensionless porous height. Experiments were also conducted with the enclosure containing fluid alone and completely filled with porous media. When the enclosure is completely filled, the porous medium Rayleigh number is below the critical Rayleigh number ($Ra_{m,c} = 40$) and heat transfer is via conduction. For their experiments with $\eta < 1$, an estimate of the Rayleigh number for the overlying fluid layer is always significantly above the critical fluid Rayleigh number for the onset of convection and convection is assumed to always be present in the fluid layer.

Utilizing flow visualization, the authors observe jet-like penetration into the porous layer. They note that as soon as convection is initiated in the fluid layer, the convection will interact with the porous layer, meaning distinct regions of conduction in the porous layer, and convection in the fluid layer, are not possible. Similar to the

findings of Poulikakos [18], Prasad and coworkers observe an increase in the number of convection cells with increasing porous layer height.

For glass and acrylic beads saturated in silicon and glycol ($\lambda = k_f/k_m = 0.34 – 1.0$), the Nusselt number decreases as a layer of particles is introduced. The reduction is more significant at lower heater power (lower Rayleigh numbers) and for the smaller beads that have lower permeability. For small beads (3 and 6 mm DIA), the Nusselt number decreases monotonically with increasing porous height. However, for beads larger than 6 mm DIA, the relationship between increasing porous layer height and Nusselt number is more complex. For a fixed heater power (results not shown for fixed Rayleigh number), with increasing porous height, the Nusselt number decreases to a minimum value then increases to a maximum and then possibly decreases further, depending on the bead material, size, saturating fluid and heater power. A representative sample of this variation is shown in Figure 2.21 for 12.7 and 25.4 mm DIA acrylic beads saturated in silicon. For 12.7 mm DIA balls (solid line), the Nusselt number decreases to a minimum value with increasing porous layer height and then begins to increase, though the value for the enclosure completely filled with porous media is less than that for fluid alone. Slight variation is also observed for 25.4 mm spheres, though a consistent behavior is not identified. The deviation is less dramatic and tends to be within the experimental error of 6 – 8%. The non-monotonic variation in Nusselt number is attributed to an increase in the number of convective rolls for increasing porous layer height. Increasing Nusselt number for large η could also be the result of a transition to convection dominated in the porous region as discussed by Chen and Chen [15].

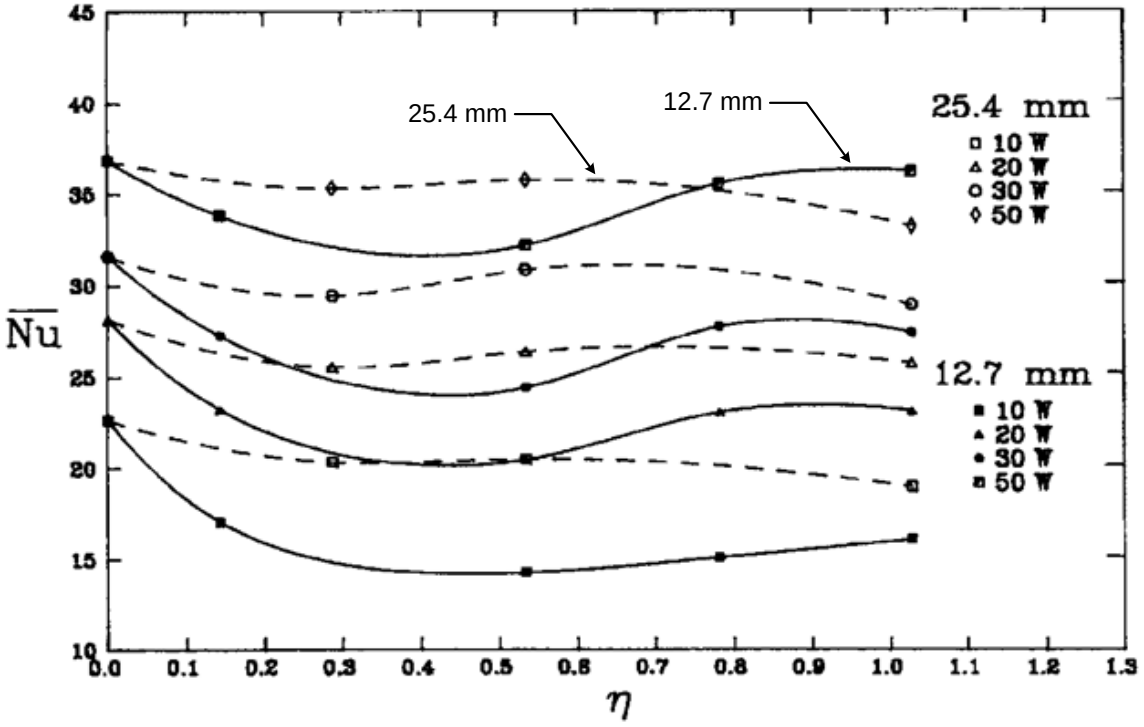

Figure 2.21. Effect of porous layer height on Nusselt number, 12.7 and 25.4 mm acrylic beads saturated in silicon [20].

Only 25.4 mm DIA beads were used when the porous medium was aluminum ($0.07 > \lambda > 0.08$). For $\eta > 0$, the relationship between Nusselt number and Rayleigh number, for a given η, is similar regardless of saturating fluid. This result is shown in Figure 2.22 for aluminum beads with $\eta = 0.53$ (here the Rayleigh number is based on heat flux, Ra* = Ra Nu) as all data points, regardless of saturating fluid fall on a single line. Note that the experiments with silicon saturating fluid are run at different Rayleigh numbers than the experiments for "matching" silicon or glycol. This result is consistent with the numerical findings of Chen and Chen [16], who found little change in Nusselt number with Prandtl number because the flow does not penetrate into the porous layer where Prandtl number dependence, outside of what is included in the Rayleigh number, has been shown to occur.

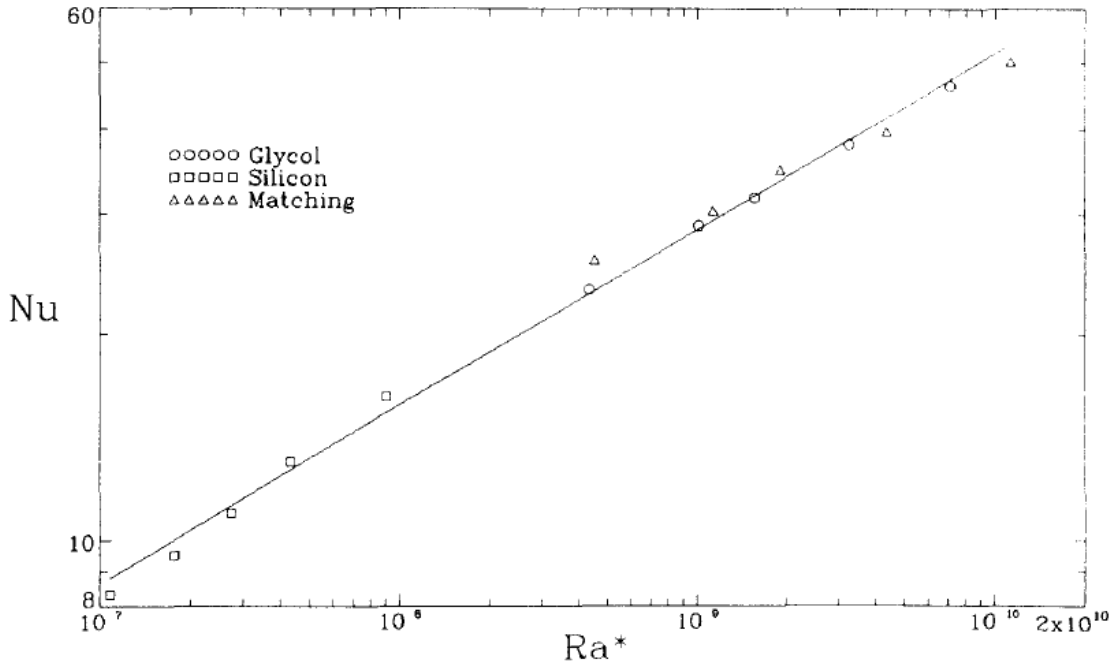

Figure 2.22. Variation in heat transfer with Prandtl number for an enclosure partially filled with aluminum beads saturated in glycol, silicon, and "matching" silicon [22].

When the enclosure is partially filled with aluminum beads, $0 > \eta > 1$, the Nusselt number versus Rayleigh number relationship changes very little with increasing porous layer height. The clearest example of this trend is shown in Figure 2.23 for 25.4 mm DIA aluminum beads saturated in glycol. For a given Rayleigh number, and $0 < \eta < 1$, the Nusselt number is relatively constant with increasing porous height and no clear trend of Nusselt number increasing or decreasing with porous height is observed. For $0 < \eta < 1$, the enhanced diffusion of the high conductivity aluminum beads appears to offset the suppression of advection with the addition of porous media, and the relationship between Nusselt number and Rayleigh number changes very little with the addition of porous media. Trends similar to those shown in Figure 2.23 are observed when the aluminum

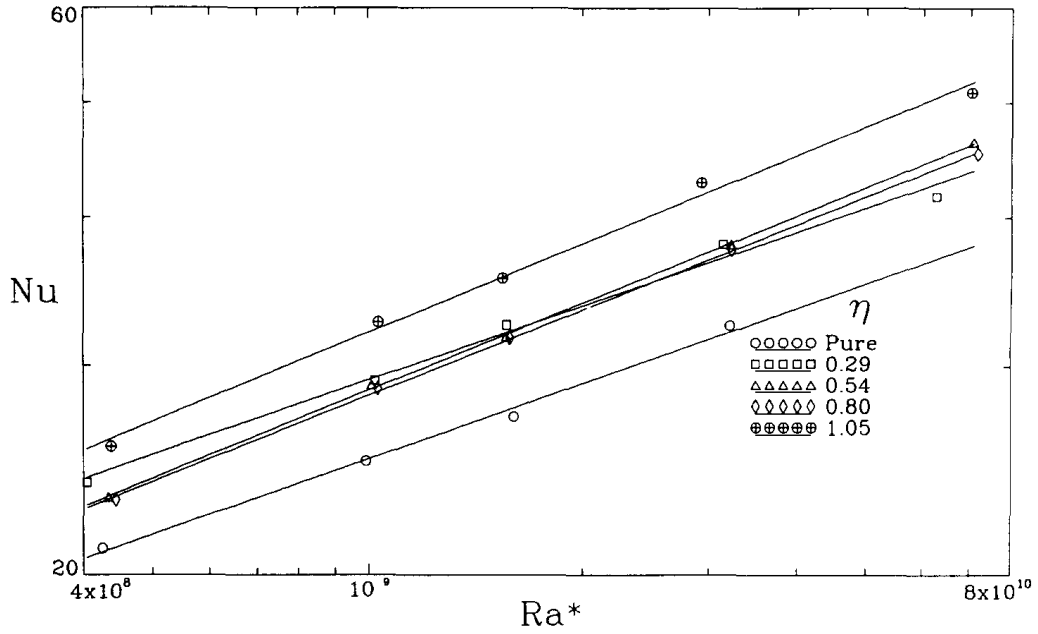

Figure 2.23. Nusselt number versus Rayleigh number for 25.4 mm aluminum beads saturated in glycol. In the plot "pure" is when $\eta = 0$ and $\eta = 1.05$ is for a fully filled enclosure. From Prasad [22].

beads are saturated in matching silicon fluid, though more spread is observed in the data (plots not shown). For aluminum beads saturated in glycol ($Pr \approx 350$) or matching silicon ($Pr \approx 185$), the Nusselt number increases with the addition of aluminum beads. However, for silicon fluid ($Pr \approx 6000$), the Nusselt number decreases with the addition of aluminum beads.

Chandra [23] experimentally investigated natural convection heat transfer in layers of water-saturated 6 mm diameter glass beads with an overlying water layer. Experiments were performed in a tall cylinder with $A = H/D = 1.9$. Because of the high aspect ratio, experiments for water alone did not follow previously published data. Shown in Figure 2.24, a significant drop in heat transfer is observed with the addition of a thin layer of porous media ($\eta \approx 0.1$). For fixed fluid Rayleigh number, the Nusselt

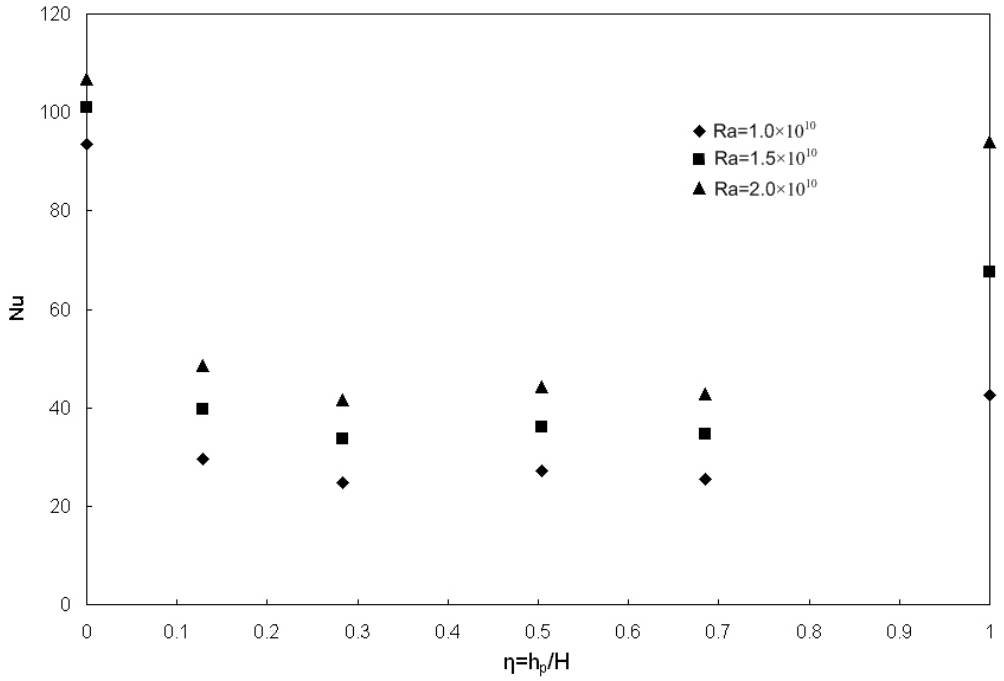

Figure 2.24. Nusselt number variation with porous height for a cylindrical enclosure partially filled with glass beads saturated in water [23].

number decreases slightly for increasing porous height until the enclosure is completely filled with porous media, at which point the Nusselt number increases to a value still below that for a fluid layer alone. The lack of variation with increasing porous height for $0 < \eta < 1$ is inconsistent with the experimental results of Prasad et al. [20] who observed a monotonic decrease in Nusselt number with the addition of 6 mm low conductivity spheres.

2.5. Summary of Literature Review

The literature review discussed Rayleigh-Bénard equivalent convection heat transfer in saturated porous media and in saturated porous media with a superposed fluid layer. Natural convection in a horizontal layer of metal foam in an infinite domain was

also discussed to provide additional background on the behavior of metal foam in natural convection heat transfer.

Rayleigh-Bénard equivalent convection with a horizontal layer of low conductivity porous media with a superposed fluid layer yields reduced Nusselt numbers compared to an enclosure completely filled with porous media or with fluid alone. Convection is mostly confined to the fluid layer, creating a region of relative stagnation in the porous layer, reducing heat transfer. The depth of penetration into the porous layer was not consistent among the numerical studies as Chen and Chen [15, 16] and Kim and Choi [17] observed limited flow penetration while Poulikakos [18] and Poulikakos et al. [19] observed greater penetration into the porous layer. Poulikakos found the Nusselt number, as well as flow penetration into the porous layer, to increase with increasing fluid Rayleigh number and Darcy number.

Natural convection heat transfer in a horizontal layer of high conductivity porous media with a superposed fluid layer is a balance between enhanced thermal diffusion and decreased fluid advection with the addition of the porous media. For large aluminum beads ($\gamma = 0.29$), Prasad et al. [22] found the Nusselt number increases with the addition of aluminum beads for the lower Prandtl number fluids (matching silicon and glycol with $Pr \approx 350$ and 185) and decrease with silicon saturating fluid, $Pr \approx 6000$. Kathare et al. [14] investigated natural convection in a cylindrical enclosure with a horizontal layer of copper metal foam and an overlying fluid layer heated from below. Heat transfer enhancement was found to depend on the placement of the foam layers. With foam on the hot boundary alone, the authors observed enhancement in heat transfer rates of 12 and 15% for an enclosure filled 33 and 66% with foam, respectively. With foam on both

boundaries, enhancements of 35 and 47% were observed for an enclosure filled 50 and 66% with foam, respectively.

The studies of natural convection in superposed fluid layers of low conductivity porous media, with $k_f/k_m \approx 1$, do not encounter the trade-off between increased diffusion and decreased advection encountered with high conductivity porous media. With four layers of aluminum beads filling the enclosure in the work of Prasad et al. [22], it is difficult to conclude the that beads behave like porous media. Indeed, with small, low conductivity beads, Prasad at al. [22] observed a monotonic decrease in the Nusselt number with increasing porous height. With large beads, the relationship between Nusselt number and porous height was complex, with the Nusselt number decreasing, increasing and then decreasing again with the addition of more porous media. The work of Kathare et al. [14], with a fluid superposed layer of copper foam, was limited to four experiments. The present study expands on the work of Kathare et al. [14] to provide a more complete set of experiments, including the variation of Nusselt number with Rayleigh number, porous height, pore density and foam placement. The results are compared to the foam filled enclosure results of Kathare et al. [14] to determine if a partially filled enclosure can provide similar enhancement in heat transfer over a water layer alone.

CHAPTER 3 DESIGN OF EXPERIMENTS

3.1. Experimental Scope

The present study investigates Rayleigh-Bénard equivalent convection heat transfer with copper foam and a superposed fluid layer to determine whether a partially filled enclosure performs comparably to an enclosure fully filled with foam. The properties of the water-saturated foam, including effective conductivity, porosity, permeability, and drag coefficient are measured. Heat transfer is quantified through the enhancement factor defined in Eq. (2.11), which compares heat transfer with foam to that of a water layer. In the first set of experiments the enclosure contains water alone. For experiments with foam, effects on heat transfer from changing foam height, permeability, foam placement and Rayleigh number are investigated. Metal foams of 5 and 10 PPI are used with bulk porosity ranging from $0.88 - 0.92\%$. In the second and third sets of experiments, 5 and 10 PPI foam is placed on the hot boundary as in Figure 3.1 (a). In the fourth set of experiments, 10 PPI foam is placed on both boundaries as in Figure 3.1 (b). When foam is placed on both boundaries, a 4.67 mm acrylic ring holds the top layer of foam in place. For each set of experiments with foam, at a fixed dimensionless foam height, $\eta = H_p/H$, a series of experiments are conducted over a range of Rayleigh numbers: $2 \times 10^6 < Ra_H < 5 \times 10^8$ with foam on the hot boundary and $1 \times 10^7 < Ra_H < 3 \times 10^8$ with foam on both boundaries. In this way the Nusselt number as a function of Rayleigh number is determined for each dimensionless foam height and each set of experiments. The procedure is repeated for dimensionless foam heights of $\eta = 0.25$, 0.5, and 0.75 when foam is only on the hot boundaries, and for $\eta = 0.5$ and 0.75 when foam is on both boundaries. Table 3.1 provides a summary of experiments.

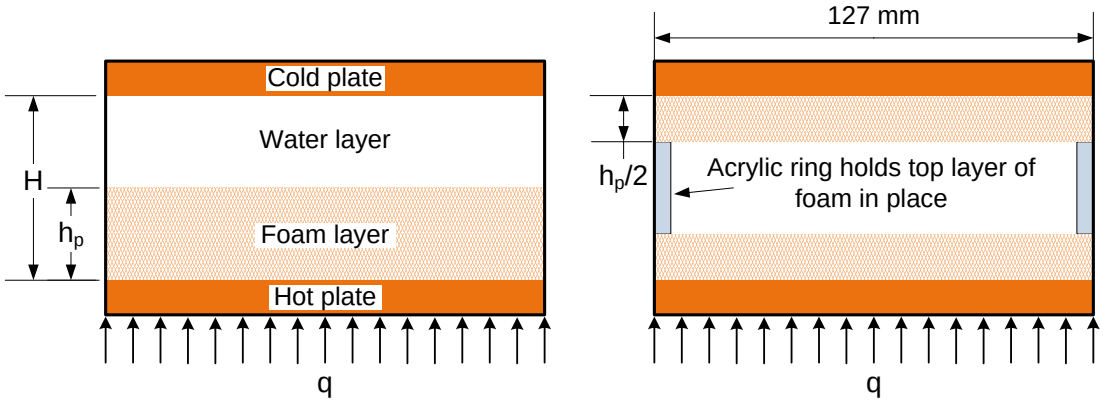

a) Foam on hot boundary b) Foam on both boundaries

Figure 3.1. Sketch of experimental apparatus showing two foam configurations, foam on the hot boundary (a), and foam on both boundaries (b).

Table 3.1. Summary of experiments.

Set	Foam placement	Pore density	Porosity	$\eta = H_p/H$	$A = H/D$	Ra_H
1	Water alone	---	---	0	0.2 – 0.8	$9\times10^5 – 3\times10^8$
2	Type (a)	10 PPI	0.88 – 0.92	0.25, 0.5, 0.75	0.1 – 0.8	$2\times10^6 – 5\times10^8$
3	Type (a)	5 PPI	0.89	0.25, 0.5, 0.75	0.1 – 0.8	$2\times10^6 – 5\times10^8$
4	Type (b)	10 PPI	0.88 – 0.92	0.5, 0.75	0.3 – 0.8	$1\times10^7 – 3\times10^8$

3.2. Experimental Apparatus

3.2.1. Apparatus Overview

A cross sectional view of the experimental apparatus is shown in Figure 3.2. The cylindrical, 127 mm diameter test section rests between two isothermal copper plates, the upper plate hotter than the lower plate. The diameter of the test section is limited to 0.127 m by the maximum size of copper foam disks available from the manufacturer (ERG Aerospace [25]). The metal foam is made of C10100 copper alloy. The apparatus

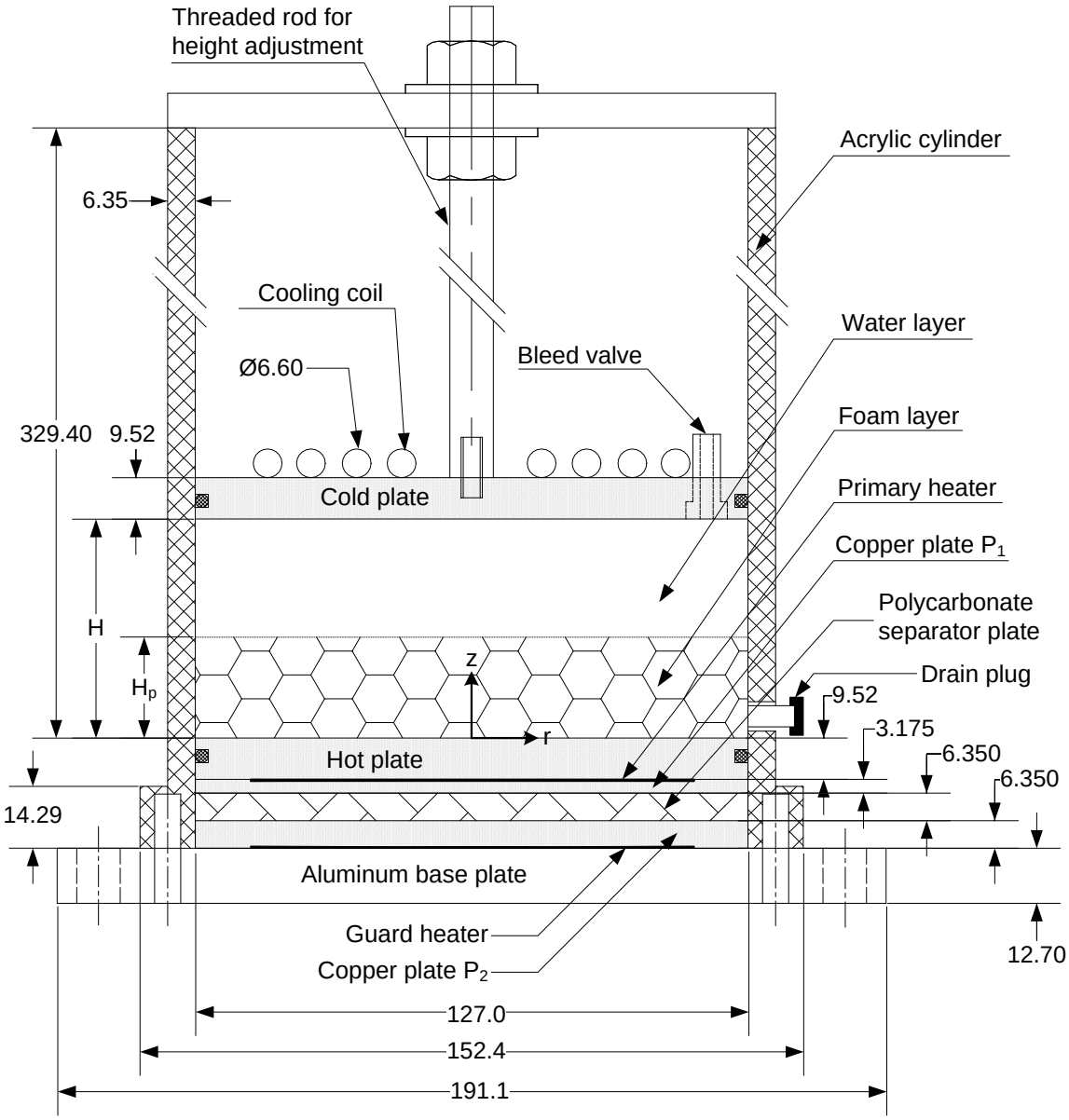

Figure 3.2. Cross sectional view of experimental apparatus for heat transfer experiment (adapted from [32]).

utilizes a threaded rod and nut assembly to modify the height of the test section. The apparatus rests on an aluminum base plate that is attached to a wood base through a bolt and nut assembly (wood base not shown in Figure 3.2). The nuts are adjustable to allow leveling of the apparatus. The upper cool plate is maintained at a constant temperature by

flowing tap water through a copper tube brazed to the upper surface. The primary heater located below the lower "hot" plate provides a constant heat flux. The lower plate is thick enough to provide a constant temperature boundary condition. A guard heater is utilized to minimize loss through the base of the apparatus by setting the heat flux to minimize the temperature difference across a 6.35 mm thick polycarbonate disk ("separator plate") that separates the primary and guard heaters. Heat loss through the base of the apparatus is quantified by measuring the temperature difference across the separator plate. The test section is enclosed by a 6.35 mm thick acrylic tube that is wrapped in fiberglass insulation to minimize heat loss. A drain plug located near the base of the test section is used to fill and drain water before and after experiments. A bleed valve is inserted into the cold, upper plate to allow for the removal of air.

3.2.2. Temperature and Power Measurement

Temperatures are measured with 30 gauge type-T thermocouples. The thermocouples are calibrated with reference to a Class A RTD. The largest thermocouple bias error was 0.25 °C. Thermocouple calibration is discussed in Appendix A. The temperature of the upper and lower isothermal boundaries is measured by embedding thermocouples into each of the 9.5 mm thick copper plates with OmegaBond 101 thermally conductive epoxy (k = 1 W/mK). The isothermal plates and thermocouple locations are shown in Figure 3.3. The thermocouples are fixed at two radial locations, r = 12.7 mm and r = 38.1 mm, measured from the center of the plate. At each radial location thermocouples are separated by 120°. Only the three outer thermocouples, at r = 38.1 mm, were used for the hot plate. The thermocouples are embedded 0.53 mm

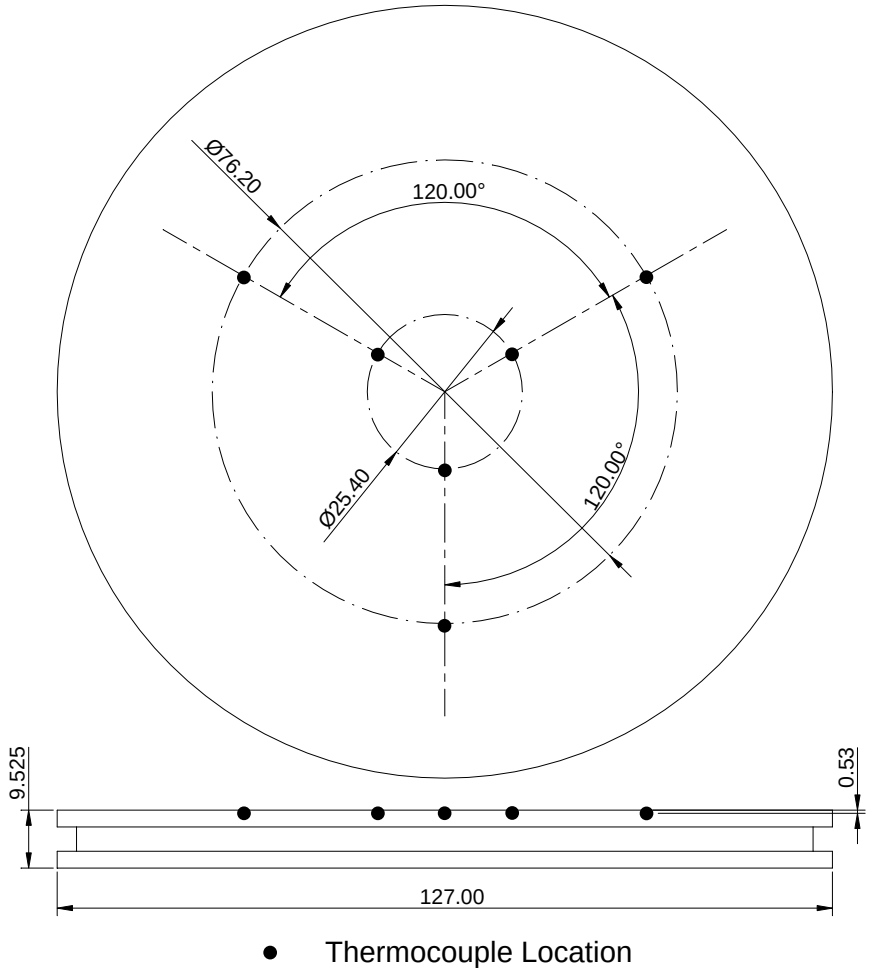

Figure 3.3. Thermocouple locations on the isothermal plates. Only the outer thermocouples (D = 76.2 mm) were used on the hot plate. The cold plate used both the outer and inner sets of thermocouples. Dimensions are in mm. Figure from [32].

below the surface of the isothermal plates. The embedding is achieved on the upper plate by drilling a small hole 0.53 mm into the top surface (the surface facing away from the test section) and adhering the junction in the hole using thermally conducting epoxy. This method is not possible for the lower plate as the surface facing away from the test section is in contact with the copper plate P_1, as shown in Figure 3.2. Thus for the hot plate, 0.53 mm deep grooves are cut out of the underside of the plate to allow

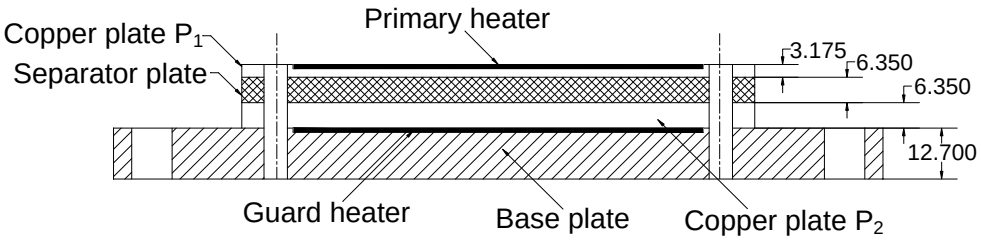

Figure 3.4. Separator plate assembly. Dimensions are in mm. Figure from [32].

thermocouple wire to be routed to the edge of the plate and then through the sub assembly and out of the apparatus.

Shown in Figure 3.4, the separator plate assembly consists of the two heaters, copper plates P_1 and P_2, the polycarbonate separator plate, and the aluminum base plate. The separator plate assembly provides heat input to the system and is used to measure heat loss through the base of the apparatus. The temperature across the 6.35 mm polycarbonate plate (k = 0.195 W/mK) is measured with thermocouples embedded in the plates, P_1 and P_2, adjacent to the upper and lower surface of the polycarbonate plate. Six total thermocouples are embedded in each plate. The thermocouples are embedded in the copper plates in a similar manner as the hot plate thermocouples. Three thermocouples at two radial locations (r = 25.4 mm and r = 50.8 mm) are separated by 120° each. Radial grooves are cut to allow the thermocouple wire to be routed to the edges and out of the apparatus (see Figure 3.5).

Thermocouples on the outer surface of the acrylic cylinder, used for measuring heat loss, are bonded to the cylinder using aluminum tape. The thermocouples on the

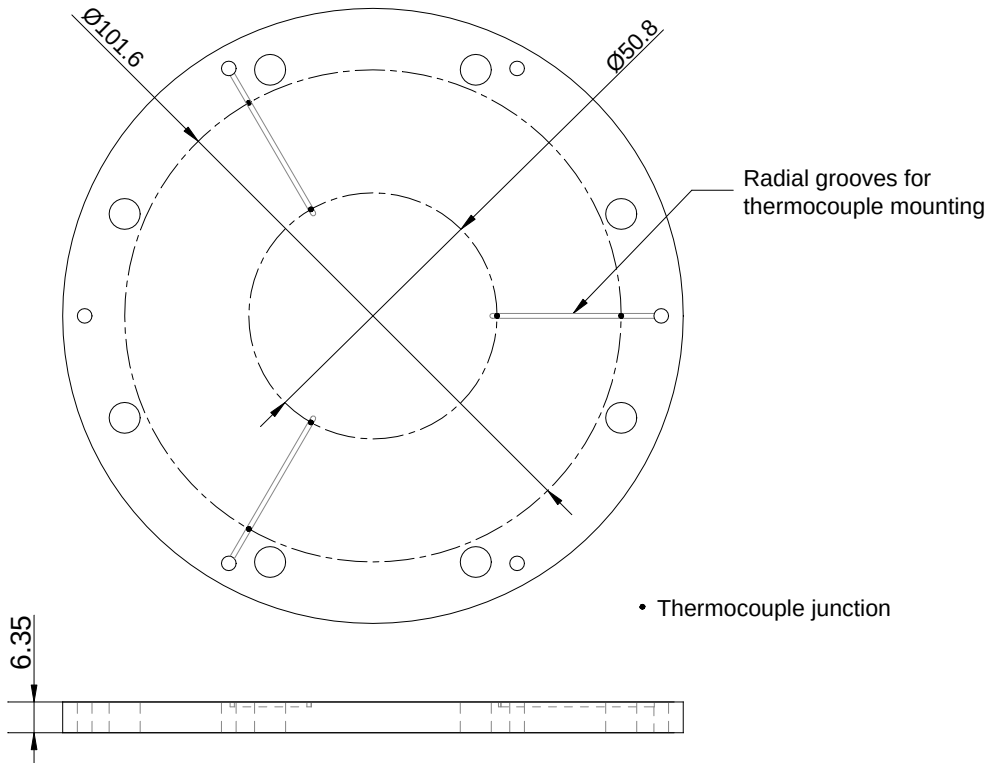

Figure 3.5. Copper plate P_2 showing radial grooves for thermocouple mounting. Dimensions in mm. Figure from [32].

outer surface of the acrylic cylinder, used to measure heat loss, are separated by 180°. Table 3.2 shows the thermocouple locations referenced to the coordinates of Figure 3.2.

As shown in Figure 3.4, a shallow, circular recess is cut in the copper plate P_1 and the aluminum base plate to allow mounting of the primary and guard heaters. The AC resistive heaters have a 65 W power rating, a resistance of 218.9 Ω, a 0.1016 m diameter, and a thickness of 1.397 mm. Variable autotransformers are used to vary the voltage to the heaters, allowing control of the heater power.

3.2.5. Pressure Drop Apparatus for Measuring Permeability and Drag Coefficient

Pressure drop experiments to measure permeability and drag coefficient are conducted in the apparatus shown in Figure 3.6. Flow rate is measured with a Merian

Table 3.2. Thermocouple locations.

Thermocouple is embedded in	Temperature measured	Number of thermocouples at location	Thermocouple location	
			z (mm)	r (mm)
Cold Plate	T_c	3	H+ 0.530	12.7
		3	H+ 0.530	38.1
Hot Plate	T_h	3	-0.530	38.1
Copper plate P_1	T_{s1}	3	-12.700	25.4
		3	-12.700	50.8
Copper plate P_2	T_{s2}	3	-19.05	25.4
		3	-19.05	50.8
Acrylic cylinder	T_{mo}	2	H/2	69.85
Acrylic cylinder	T_{ho}	2	-4.76	69.85
Acrylic cylinder	T_{so}	2	-17.46	76.2

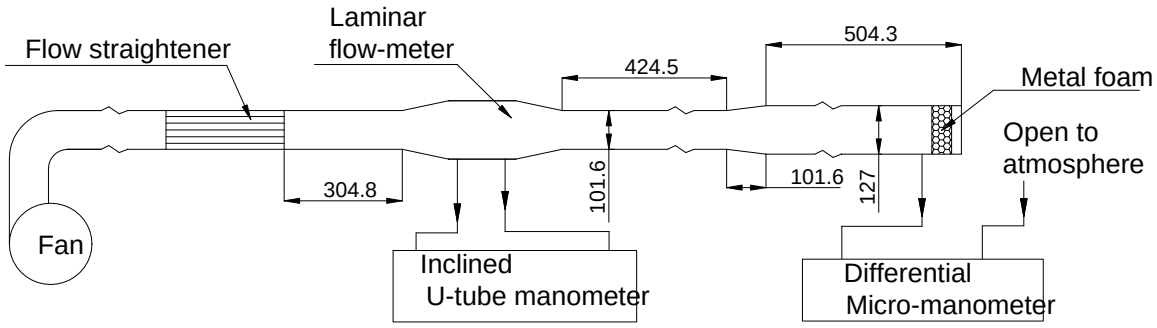

Figure 3.6. Pressure drop apparatus for measuring permeability and drag coefficient. From [32].

model 50MC2-4 laminar flow meter (accuracy of ±0.72% of reading) and a Dwyer incline manometer with 0.02 inches of water column resolution). The pressure drop across the foam is measured with a Dwyer Microtector micro-manometer with resolution of 0.0005 inches of water column.

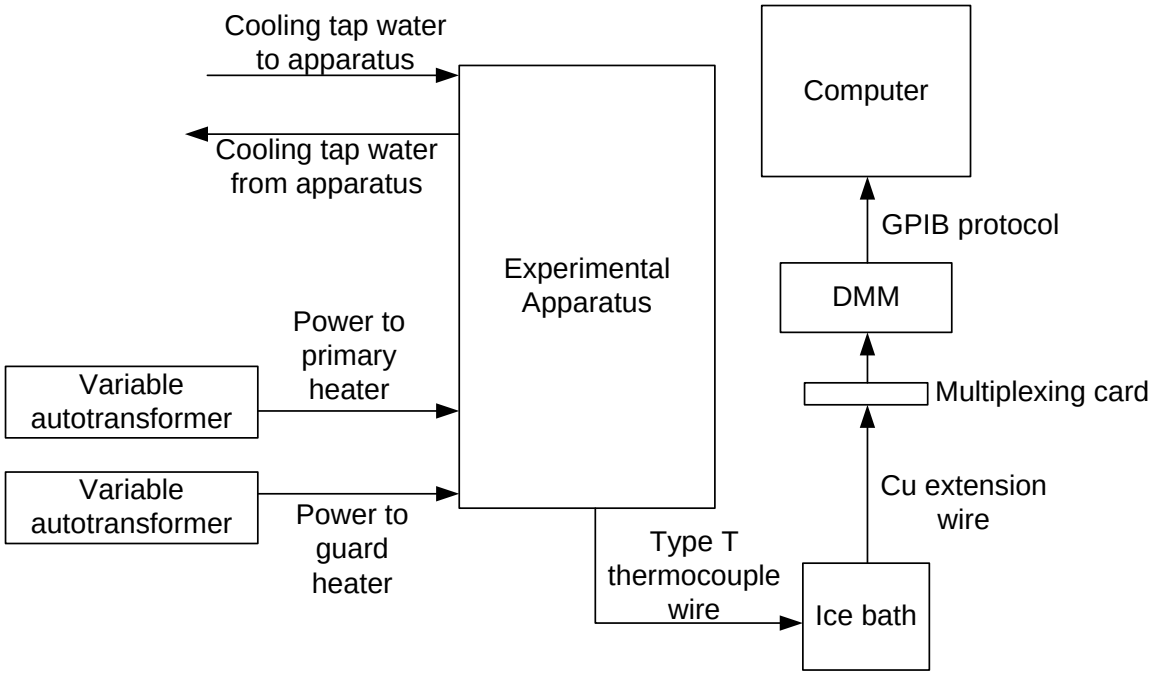

Figure 3.7. Flow chart of energy and data acquisition system.

3.3. Data Acquisition

Data acquisition is accomplished using a Keithley DMM, model 2700, with a Keithley 7708 multiplexer card. Communication between the computer and DMM is through an IEEE-488 GPIB interface and GPIB protocol. The data acquisition system is controlled with a Microsoft Excel add-on supplied by Keithley (ExceLINX-1A). There are approximately three seconds between data points. The thermocouple emf is converted to temperature using the standard NIST ITS-90 thermocouple database. The average thermocouple temperatures are later corrected based on calibration against a Class A RTD. An ice bath (0 °C) is used as a reference temperature. A schematic of the energy flow and data acquisition of the system is shown in Figure 3.7.

3.4. Experimental Procedure

A thin layer of thermally conducting paste (Omegatherm 201, 2.3 W/mK) is applied to the isothermal plate(s) to attach the metal foam. Metal foam of the desired thickness is then inserted into the apparatus as shown in Figure 3.1 (a) and (b). When foam is touching both boundaries, as in Figure 3.1 (b), an acrylic annulus of thickness 4.67 mm is inserted between the metal foam layers to hold the top layer in place. Ultrapure water is degassed by boiling the water and letting it slowly cool. The water is added from below through the drain plug shown in Figure 3.2. Air bubbles are occasionally trapped in the metal foam and must be removed by tapping the acrylic cylinder or stirring the fluid. The cold plate assembly is then inserted into the apparatus at the desired height. The bleed valve is utilized to ensure all remaining air is removed from the apparatus. The apparatus is leveled and then fiberglass insulation ($R = 3.35$ K-m^2/W) is wrapped around the apparatus.

The upper plate is maintained at a constant temperature by flowing tap water ($\approx$ 6 liters/min) through a 6.60 mm diameter circular copper coil that is brazed to the top of the plate as shown in Figure 3.2. The flow rate is sufficiently high such that the plate maintains spatially uniform temperature. The primary and guard heaters are then turned on. The guard heater voltage is adjusted to minimize the temperature difference across the acrylic separator plate (to minimize heat loss). Once the experiment is set up, data collection is initiated. A transient period is approximately four hours. The top of the separator plate is the last location to reach steady state. Experiments end after all plate temperatures have been steady for approximately two hours. Upon completion of an

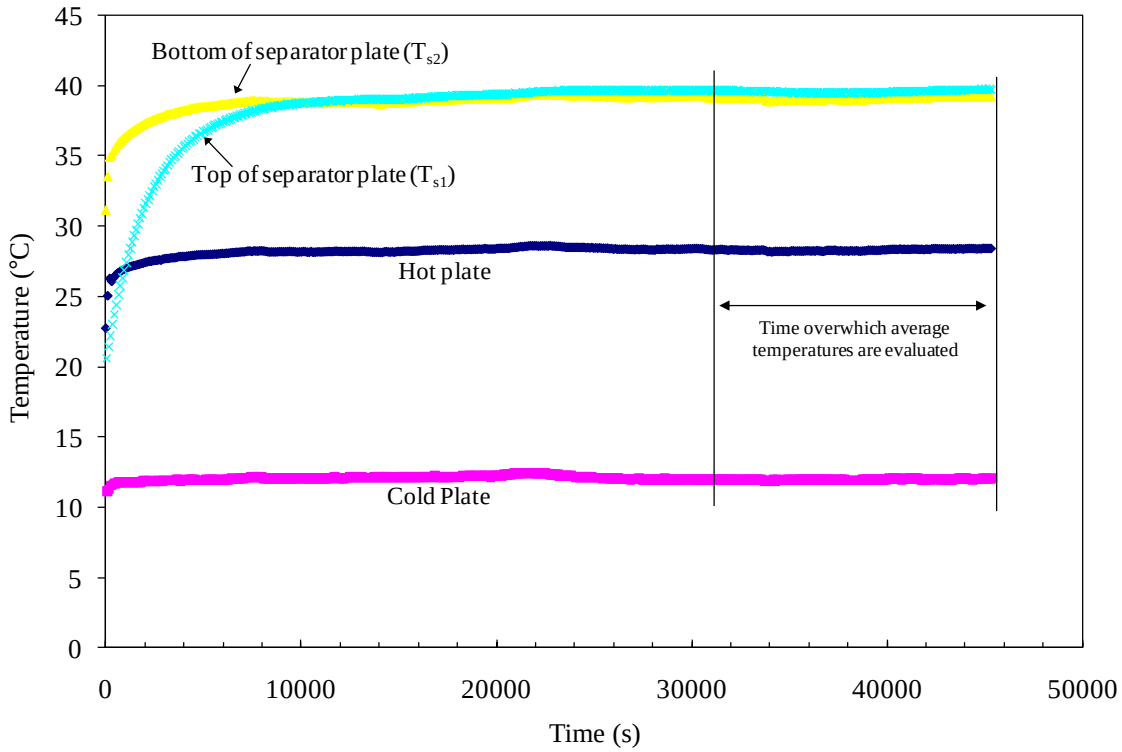

Figure 3.8. Experimental data showing transient and steady regions.

experiment, a data file is saved and data analysis is performed as outlined in the following section. A representative plot of the transient and steady data is shown in Figure 3.8.

3.5. Data Analysis

This section describes how the foam properties, average temperatures, heat input, heat loss, the Nusselt and Rayleigh numbers and enhancement in heat transfer are analyzed. Fluid properties are calculated at the mean of the hot and cold plate temperatures. Engineering Equation Solver (V8.422-3D) is used to determine fluid properties. The curve coefficients are provided in Appendix E.

3.5.1. Foam Porosity, Effective Conductivity, Drag Coefficient and Permeability

The porosity is defined as the ratio of void volume to total volume

$$\phi = \frac{\text{Void Volume}}{\text{Total Volume}} = \frac{\text{Total Volume} - \text{Solid Volume}}{\text{Total Volume}} \tag{3.1}$$

The total volume is calculated as the cross sectional area multiplied by the thickness. If the mass of the air inside the voids is assumed to be negligible, the solid volume is the total mass of the block divided by the density of the copper alloy. The porosity is then

$$\phi = \frac{(\pi R^2 \cdot t) - \frac{m_{foam}}{\rho_{copper}}}{\pi R^2 \cdot t} \tag{3.2}$$

where R and t are the radius and thickness of the foam sample, m_{foam} is the mass of the foam, and ρ_{copper} is the density of the copper alloy (8930 kg/m^3). Dimensions are measured with a digital caliper (±0.02 mm). Mass is measured with a digital balance (±0.01 g). Porosity measurements have a relative uncertainty of less than 0.15%.

An effective thermal conductivity of the copper foam saturated in water is measured with the test section completely filled with foam at a pre-convection Rayleigh number. Experiments are run over a range of Rayleigh numbers to ensure that no convection is taking place in the test section. To validate the results, an experiment is also performed with heating from above to create a stable temperature gradient. The effective thermal conductivity of the water-saturated copper foam is

$$k_m = \frac{QH}{A_c\,(T_h - T_c)} \tag{3.3}$$

where Q is the power, H is the height of the test section, and T_h and T_c are the hot and cold plate temperatures.

The permeability and drag coefficient are determined using the simplified momentum equation provided in Eq. (2.4) and repeated below.

$$\frac{\Delta P}{H_p} = -\frac{\mu_f}{K} U - \frac{C_F}{K^{1/2}} \rho_f U^2 \tag{2.4}$$

Measuring the flow rate and pressure drop across the foam, with known fluid properties, the permeability and drag coefficient are determined by plotting $\Delta P/H_p$ versus U and fitting a second order polynomial to the data.

3.5.2. Temperature Measurement

Multiple thermocouples are used to determine the average temperatures of the hot, cold, and separator plates, and the regions on the outer portion of the cylinder used for measuring heat loss. The mean temperature of each thermocouple, $\overline{T}_j$, is the arithmetic mean of the temperatures measured by each thermocouple during steady operation,

$$\overline{T}_j = \frac{1}{M} \sum_{i=1}^{M} T_{ji} \tag{3.4}$$

where M is the total number of measurements for each thermocouple. The mean temperature of each plate is determined by averaging the mean of the individual thermocouple measurements,

$$\overline{T} = \frac{1}{N} \sum_{j=1}^{N} \overline{T}_j \tag{3.5}$$

where N = 3 for the hot plate, N = 6 for the cold plate and the top and bottom of the separator plate, and N = 2 for each of the three locations at which heat loss is measured (T_h, T_c, T_{s1}, T_{s2}, T_{mo}, T_{ho}, T_{so}).

3.6.2. Heat Transfer

The power from the primary heater is,

$$Q_p = \frac{V_p^2}{R} \tag{3.6}$$

where V_p is the voltage of the primary heater and R is the resistance of the primary heater (218.9 Ω). The primary heater voltage, V_p, is measured using the same DMM and multiplexing card as temperature measurements. The total heat input, Q, is the difference between the primary heater power and the heat loss,

$$Q = Q_p - Q_L \tag{3.7}$$

As shown in Figure 3.9, the heat loss, Q_L, is calculated assuming one dimensional heat transfer in four regions: through the base of the apparatus (Q_1), and radial loss in the region of the test section (Q_2), hot plate (Q_3), and separator plate (Q_4). A detailed explanation of heat loss calculations is found in Appendix B.

$$Q_L = Q_{L_1} + Q_{L_2} + Q_{L_3} + Q_{L_4} \tag{3.8}$$

3.6.3. Dimensionless Variables

The fluid Rayleigh number and fluid Nusselt number are based on the total height of the test section, H, and the properties of water. The fluid Rayleigh number is,

$$Ra_H = \frac{g\beta(T_h - T_c)H^3}{\alpha_f \nu_f} \tag{3.9}$$

where g is the acceleration due to gravity, β is the volumetric expansion coefficient, α_f is the thermal diffusivity of water, and ν_f is the momentum diffusivity of water.

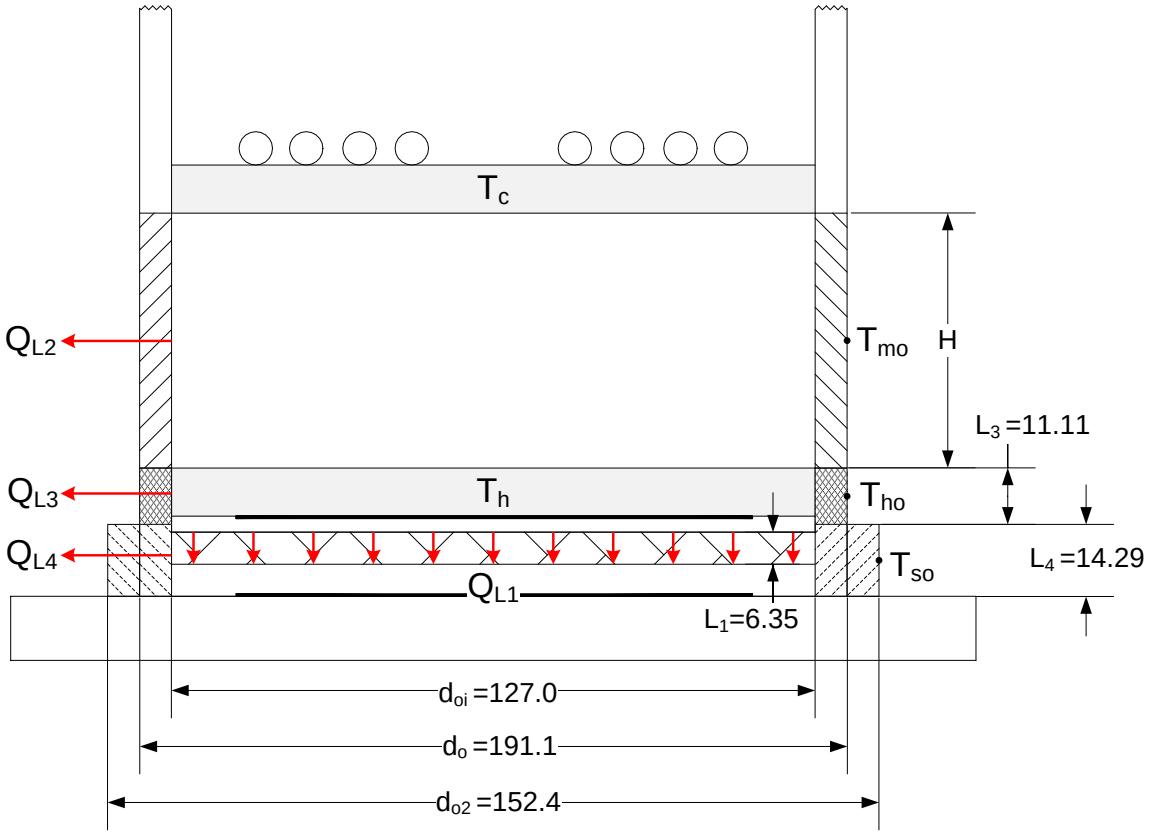

Figure 3.9. Experimental apparatus showing four locations where one dimensional heat loss is assumed. Figure adapted from [32].

The fluid Nusselt number is,

$$Nu_H = \frac{hH}{k_f} = \frac{Q}{A_c(T_h - T_c)} \cdot \frac{H}{k_f} \tag{3.10}$$

where k_f is the thermal conductivity of water and Q is the total power input as calculated in Eq. (3.6).

As discussed by Wang and Bejan [34], the medium Rayleigh number, Darcy number, and dimensionless group Pr_p fall out of the porous media momentum equation when pressure, velocity, height, and temperature are non-dimensionalized as: $P^* = P/(\mu\alpha_e/K)$, $u^* = u/(\alpha_e/H_p)$, $y^* = y/H_p$, $T^* = (T-T_c)/(T_h-T_c)$. The effective thermal

diffusivity, α_e, is the medium thermal diffusivity $\alpha_m = k_m/\rho_f c_f$. The medium Rayleigh and Nusselt numbers are based on the height and temperature difference across the foam layer. The medium Rayleigh number is,

$$Ra_m = \frac{g\beta(T_h - T_i)KH_p}{\alpha_m \nu_f} \tag{3.11}$$

where T_i is the temperature of the interface between the foam and the fluid. The interface temperature is not measured and must be estimated. The medium Nusselt number for convective heat transfer in the foam layer is

$$Nu_m = \frac{hH_p}{k_m} = \frac{Q}{A_c(T_h - T_i)} \cdot \frac{H_p}{k_m} \tag{3.12}$$

The Darcy number of the porous layer is

$$Da = K/H_p^2 \tag{3.13}$$

The porous medium Prandt number is

$$Pr_m = \frac{\mu c_f}{k_m} \tag{3.14}$$

The dimensionless group Pr_p is,

$$Pr_p = \frac{Pr_m}{C_F\sqrt{Da}} \tag{3.15}$$

where C_F is the drag coefficient in the Forchheimer term of the porous media momentum equation.

If the porous medium momentum equation is used to describe the behavior of the composite system ($0 < \eta \leq 1$), the same non-dimensionalization is used as before with the

total height, H, substituted for the porous height, H_p, and the effective thermal diffusivity is based on the average conductivity of the composite system, $\alpha_{m,s} = k_{m,s}/\rho_f c_f$. Because the foam and water are in series, the average conductivity of the composite system, $k_{m,s}$, is $\frac{H}{k_{m,s}} = \frac{H_p}{k_m} + \frac{H-H_p}{k_f}$. In terms of η, the average conductivity for the composite system is

$$\frac{1}{k_{m,s}} = \frac{\eta}{k_m} + \frac{(1-\eta)}{k_f} \tag{3.16}$$

The medium Rayleigh number for the composite system is

$$Ra_{m,s} = \frac{g\beta(T_h - T_c)KH}{\alpha_{m,s}\nu_f} \tag{3.17}$$

The medium Nusselt number for the composite system is

$$Nu_{m,s} = \frac{hH}{k_{m,s}} = \frac{Q}{A_c(T_h - T_c)} \cdot \frac{H}{k_{m,s}} \tag{3.18}$$

The Darcy number for the composite system is

$$Da_s = K/H^2 \tag{3.19}$$

The porous medium Prandtl number for the composite system is

$$Pr_{m,s} = \frac{\mu c_f}{k_{m,s}} \tag{3.20}$$

The dimensionless group $Pr_{p,s}$ for the composite system is

$$Pr_{p,s} = \frac{Pr_{m,s}}{C_F\sqrt{Da_s}} \tag{3.21}$$

3.6.7. Heat Transfer Enhancement

The heat transfer rate with foam is compared to that in a water layer with the enhancement factor,

$$E = \frac{Q_{foam}}{Q_{water}}\bigg|_{Ra_H=constant} = \frac{Nu_{H,foam}}{Nu_{H,water}}\bigg|_{Ra_H=const}$$

or equivalently,

$$E = \frac{Nu_{H,foam}}{0.125Ra_H^{0.297}}\bigg|_{Ra_H=constant} \tag{3.22}$$

where $Nu_{H,water} = 0.125Ra_H^{0.297}$ is defined in Section 4.2, Eq. (4.1). Advection enhancement is defined,

$$E_{adv} = \frac{(Q - Q_{cond})_{foam}}{(Q - Q_{cond})_{water}}\bigg|_{Ra_H=constant}$$

$$E_{adv} = \frac{Q - \dfrac{A_c\Delta T}{\dfrac{H_p}{k_m} + \dfrac{(H - H_p)}{k_f}}}{(0.125Ra_H^{0.297} - 1)\,\dfrac{k_f A_c \Delta T}{H}}\bigg|_{Ra_H=constant} \tag{3.23}$$

where Q is the measured heat transfer rate with foam defined in Eq. (3.6), A_c is the cross sectional area of the test section, ΔT is the difference between the hot and cold plates, k_m is the medium conductivity of the foam layer, k_f is the conductivity of water, H_p is the height of the foam layer, and H is the total height of the test section.

CHAPTER 4 RESULTS AND DISCUSSION

In this chapter, results are presented for the measurement of porosity, effective conductivity, permeability and drag coefficient. Heat transfer results are then presented for an enclosure partially filled with 5 and 10 PPI foam placed on the hot boundary, and 10 PPI foam on both boundaries. The heat transfer results are compared to the fully filled enclosure results of Kathare et al. [13].

4.1. Foam Properties

To reduce contact resistance between the isothermal boundaries and the metal foam, a thin layer of thermally conducting paste (Omegatherm 201, 2.3 W/mK) is applied to the isothermal plates before the foam is inserted into the test apparatus. The thermally conducting paste provides a fixed thermal resistance which reduces the measured effective conductivity. This thermal resistance is estimated by measuring the thermal paste (0.25 mm thick). The effect of the paste is accounted for in the calculation of effective thermal conductivity (Appendix C). The present results are shown and compared to previously reported results, along with the theoretical upper and lower bounds, in Table 4.1. The present results are lower than the values predicted by the models of Calmidi et al. [29], and Bhattacharya et al. [30], but align well with the measured data of Kathare [32] (see Appendix C for equations, and discussion of previous work). The present results fall within the upper and lower bounds. The models of [29] and [30] used experimental results to determine curve fit parameters. The foam samples in their experimental results were brazed to the boundaries to eliminate the contact resistance between the boundaries and the foam. There are two potential explanations for

Table 4.1. Comparison of present results with the upper and lower theoretical limits, the models of Calmidi and Mahajan [29], Bhattacharya et al. [30], and the experimental work of Kathare [32].

Method	k_m, W/mK	
	$\phi = 0.92$	$\phi = 0.89$
Upper bound (parallel model)	33.4	45.3
Lower bound (series model)	0.6	0.7
Model of Calmidi et al. [29]	12.1	15.1
Model of Bhattacharya et al. [30]	12.1	16.3
Kathare [32]	8.8 ± 0.4	-----
Present study (25.4 mm)	8.9 ± 0.6	11 ± 1

the present results showing lower effective conductivity than the models of [29] and [30]: (1) In the present study, the actual paste thickness was larger than the measured value and the contact resistance due to the thermal paste was not completely corrected for, and (2) the braze material used by [29] and [30] increased the effective conductivity of their foam sample. A detailed discussion on the measurement of the effective conductivity, with results for individual experiments, and the method of correcting measured values, is provided in the Appendix C.

If the foam is assumed to be homogeneous and isotropic, foam samples with the same pore density and porosity have the same microstructure and will have the same permeability and drag coefficient. Three groups of foam samples were used in the present experiments: 10 PPI foam with 89 and 92% porosity, and 5 PPI foam with 89% porosity. The foam sample of greatest thickness was tested from each group as a representative sample. The results of the representative sample were applied to the

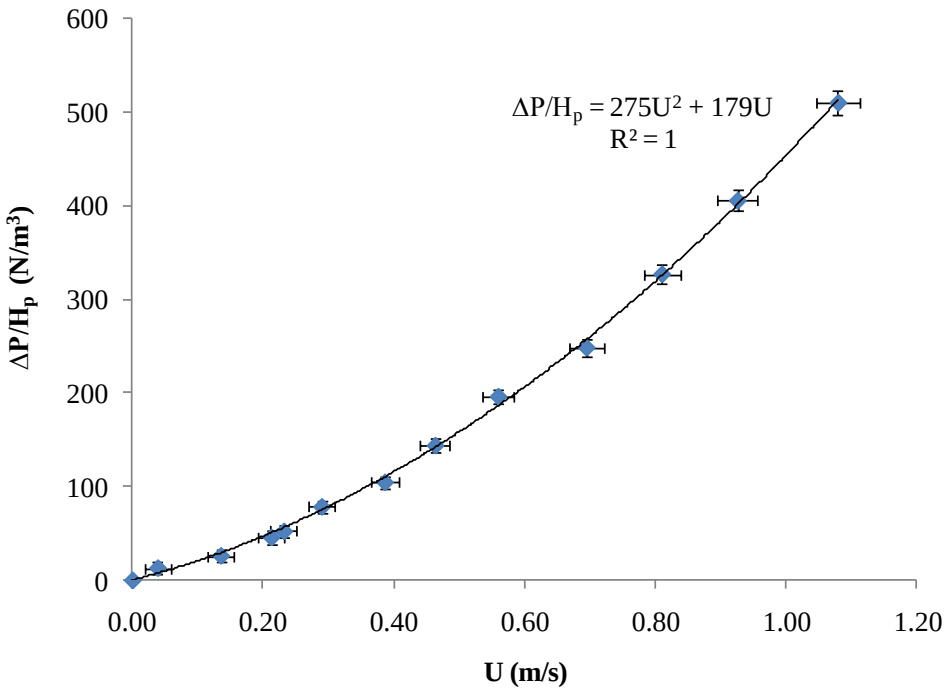

Figure 4.1. Pressure drop results for 0.75 inch thick 10 PPI copper foam with $\phi = 0.88$.

remaining samples in the group. The three foam samples tested were: A 19.1 mm thick 10 PPI foam sample with $\phi = 0.88$, a 25.4 mm thick 10 PPI foam sample with $\phi = 0.92$, and a 25.4 mm thick 5 PPI foam sample with $\phi = 0.89$. The results are plotted in Figures 4.1 – 4.3. Table 4.2 lists the foam sample tested, the group of foam samples for which the results are applied, the pressure drop versus velocity correlation and the coefficient of determination for each test. Using Eq. (2.4) and the properties of air during testing (P = 97.5 kPa and T = 24.0 °C), the permeability and drag coefficient for each case is determined. Table 4.3 compares the present results to previously published data. Bhattacharya and Mahajan [9], and Phanikumar and Mahajan [10] performed pressure drop experiments on the same foam samples with varying results. For the 5 PPI foam, the present results match the previously published permeability of [9], though the present

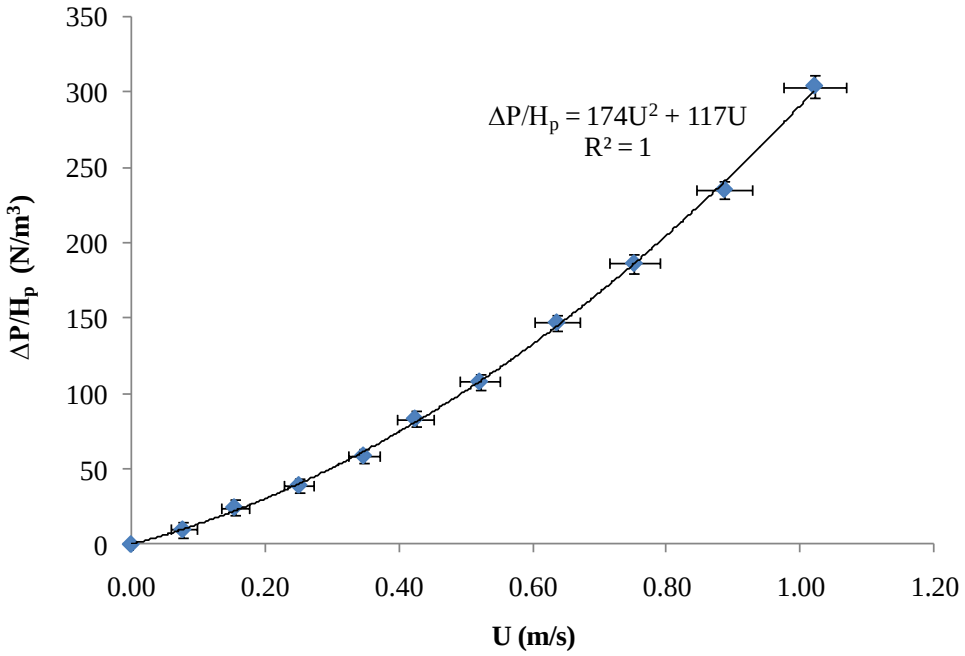

Figure 4.2. Pressure drop results for 1 inch thick 10 PPI copper foam with $\phi = 0.92$.

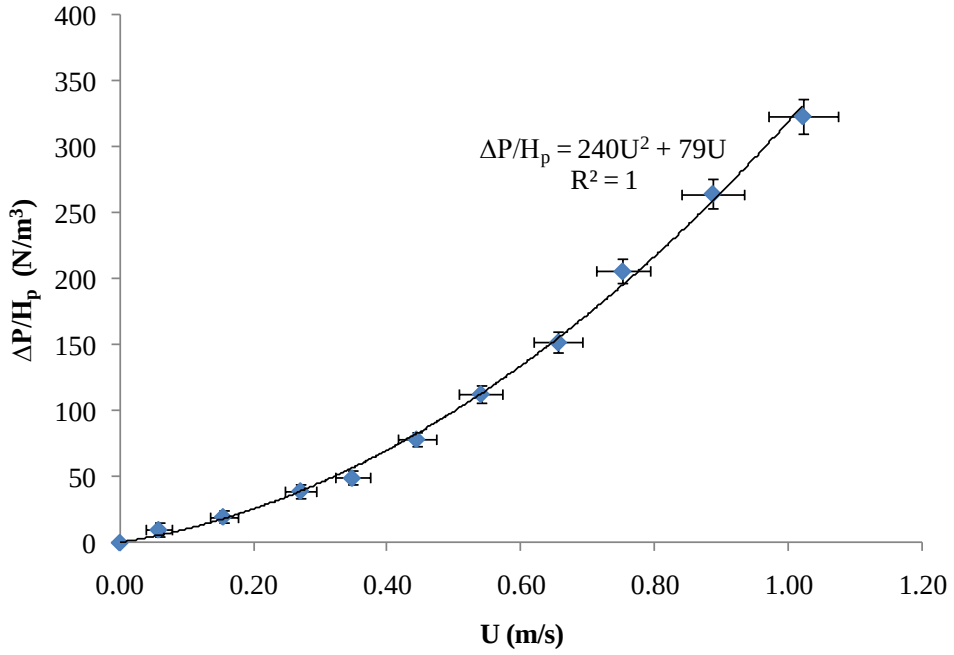

Figure 4.3. Pressure drop results for 1 inch thick 5 PPI copper foam with $\phi = 0.89$.

Table 4.2. Summary of pressure drop testing and foam samples for which the results of each test are used.

Sample tested	Samples for which results are used	$\Delta P/H_p$ vs. U correlation	R^2
19.1 mm thick, 10 PPI, $\phi = 0.88$	19.1 mm and 12.7 mm thick, 10 PPI samples with $\phi \approx 0.88$	$\Delta P/H_p = 275U^2 + 179U$	1.00
25.4 mm thick, 10 PPI, $\phi = 0.92$	25.4 mm thick, 10 PPI samples with $\phi \approx 0.92$	$\Delta P/H_p = 174U^2 + 117U$	1.00
25.4 mm thick, 5 PPI $\phi = 0.89$	All 5 PPI samples	$\Delta P/H_p = 240U^2 + 79U$	1.00

Table 4.3. Comparison of current permeability and drag coefficient with previously published values.

	Porosity	PPI	K x 10^7 (m^2)	C_F
Bhattacharya et al. [9]	0.899	5	2.28	0.075
Phanikumar et al. [10]	0.899	5	1.99	0.0802
Present study	0.89	5	2.3 ± 0.8	0.10 ±0.03
Bhattacharya et al. [9]	0.908	10	1.62	0.078
Phanikumar et al. [10]	0.908	10	1.075	0.0687
Present study	0.88	10	1.0 ± 0.1	0.077 ± 0.009
Kathare et al. [13]	0.92	10	1.6	0.068
Present study	0.92	10	1.6 ±0.2	0.061 ± 0.007

results are greater than the previously published drag coefficients of [9] and [10] by 35 and 25%. For 10 PPI foam with $\phi = 0.88$, the present results match closely with the permeability of [10] and the drag coefficient of [9]. For 10 PPI foam with $\phi = 0.88$, the permeability and drag coefficient closely match the results of Kathare et al. [13]. Table 4.4 is a summary of foam properties.

Table 4.4. Summary of copper metal foam properties.

Sample	Thickness (mm)	Pore density (PPI)	Porosity	Effective conductivity, k_e (W/mK)	Permeability, $K \times 10^7$ (m^2)	Drag coefficient, C_F
1	25.4	10 PPI	0.914	8.9 ± 0.6	1.6 ±0.2	0.061 ± 0.007
2	19.05		0.881	10 ± 1	1.0 ± 0.1	0.077 ± 0.009
3	12.7		0.880	10 ± 1	1.0 ± 0.1	0.077 ± 0.009
4	25.4		0.918	8.9 ± 0.6	1.6 ±0.2	0.061 ± 0.007
5	19.05		0.881	10 ± 1	1.0 ± 0.1	0.077 ± 0.009
6	12.7		0.881	10 ± 1	1.0 ± 0.1	0.077 ± 0.009
7	25.4	5 PPI	0.893	11 ± 1	2.3 ± 0.8	0.10 ±0.03
6	19.05		0.893	10 ± 1	2.3 ± 0.8	0.10 ±0.03
9	12.7		0.888	10 ± 1	2.3 ± 0.8	0.10 ±0.03

4.2. Rayleigh-Bénard Convection Heat Transfer in a Water Layer

Experiments are performed with water to determine a correlation for Rayleigh-Bénard convection of the form $\mathrm{Nu} = \mathrm{C}\,\mathrm{Ra}^{\mathrm{n}}$. Shown in Figure 4.4, the results are correlated and compared to the results of Kathare et al. [13] and Garon and Goldstein [38] for Rayleigh-Bénard convection in a cylindrical enclosure using water. The correlation of Kathare et al. [13] was obtained using the same apparatus as the current experiments. Table 4.5 provides a summary of the current correlation and the correlations of Kathare et al. [13], and Garon and Goldstein [38]. The experimental apparatus and procedure are validated by close matching of the three correlations. The correlation for the present study, Eq. (4.1), is used to determine enhancement in heat transfer.

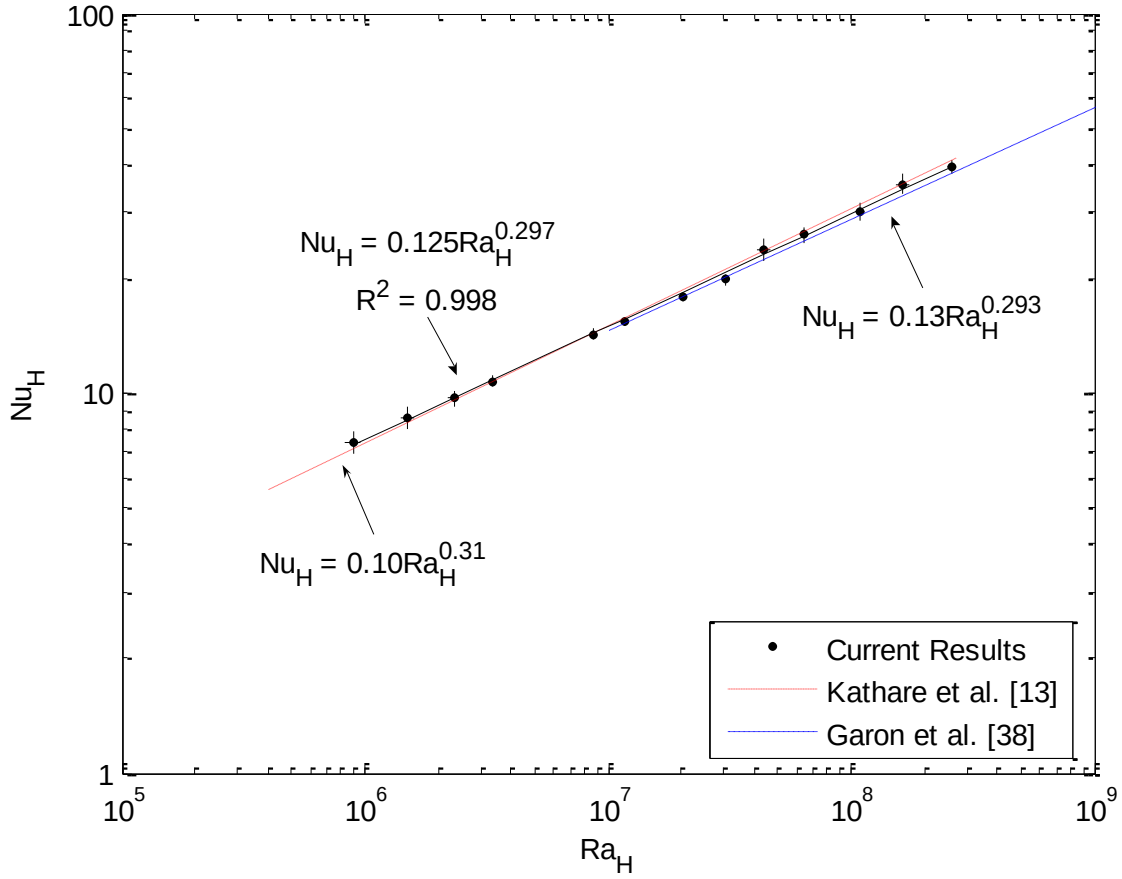

Figure 4.4. Nusselt number versus Rayleigh number for Rayleigh-Bénard convection in a cylindrical enclosure using water.

Table 4.5. Comparison of Nu_H, Ra_H, correlation for Rayleigh-Bénard convection, in a cylindrical enclosure filled with water, to [13] and [38].

	Correlation	Ra_H	H/D	Eq. #
Present study	$Nu_H = 0.125Ra_H^{0.297}$	$8.9 \times 10^5 - 2.6 \times 10^8$	0.2 – 0.8	(4.1)
Kathare et al. [13]	$Nu_H = 0.10Ra_H^{0.31}$	$4.0 \times 10^5 - 2.7 \times 10^8$	0.2 – 0.8	(4.2)
Garon and Goldstein [38]	$Nu_H = 0.13Ra_H^{0.293}$	$1.4 \times 10^7 - 3.3 \times 10^9$	0.2 – 0.4	(4.3)

4.3. Natural Convection Heat Transfer in Water-Saturated Copper Foam with an Overlying Water Layer

4.3.1. Foam on the Hot Boundary

4.3.1.1. Heat Transfer Results and Nu_H, Ra_H Correlations

A plot of fluid Nusselt number versus Rayleigh number for 5 and 10 PPI foam on the hot boundary, and $\eta = 0.25,\ 0.5,\ 0.75$ is shown in Figure 4.5. A Nusselt number correlation for water alone, Eq. (4.1), determined in the same apparatus as the experiments with foam, is shown as a solid line. The correlation for 5 PPI foam is a dashed line. The correlation for 10 PPI foam is a dash-dotted line. The results of Kathare et al. [14] for 10 and 20 PPI copper foam with $\eta = 1$ and 10 PPI foam with $\eta = 0.66$ and 0.33 are also shown. The variation in the data of Kathare et al. [13] for $\eta = 1$ is a function of the Darcy number as shown in Figure 2.8. The average uncertainty in the Nusselt number is 5% and is as high as 10%. The uncertainty in the Nusselt number is primarily due to the uncertainty in the temperature difference, T_h-T_c.

The present results with $\eta < 1$ consistently fall below the results of Kathare et al. [13] for a copper foam filled enclosure. The reduction in Nusselt number for the present results with $0.25 \leq \eta \leq 0.75$ compared to the results of Kathare et al. [13] for $\eta = 1$ is attributed to limited flow penetration into the foam layer and reduced thermal diffusion compared to an enclosure fully filled with foam. As discussed in [15 - 19], when an enclosure is partially filled with porous media, convection cells are confined primarily to the fluid layer, creating regions of stagnant fluid in the porous layer. The Nusselt number is reduced relative to an enclosure filled with porous media where convection exists throughout the enclosure. Moreover, when an enclosure is partially filled with foam, heat

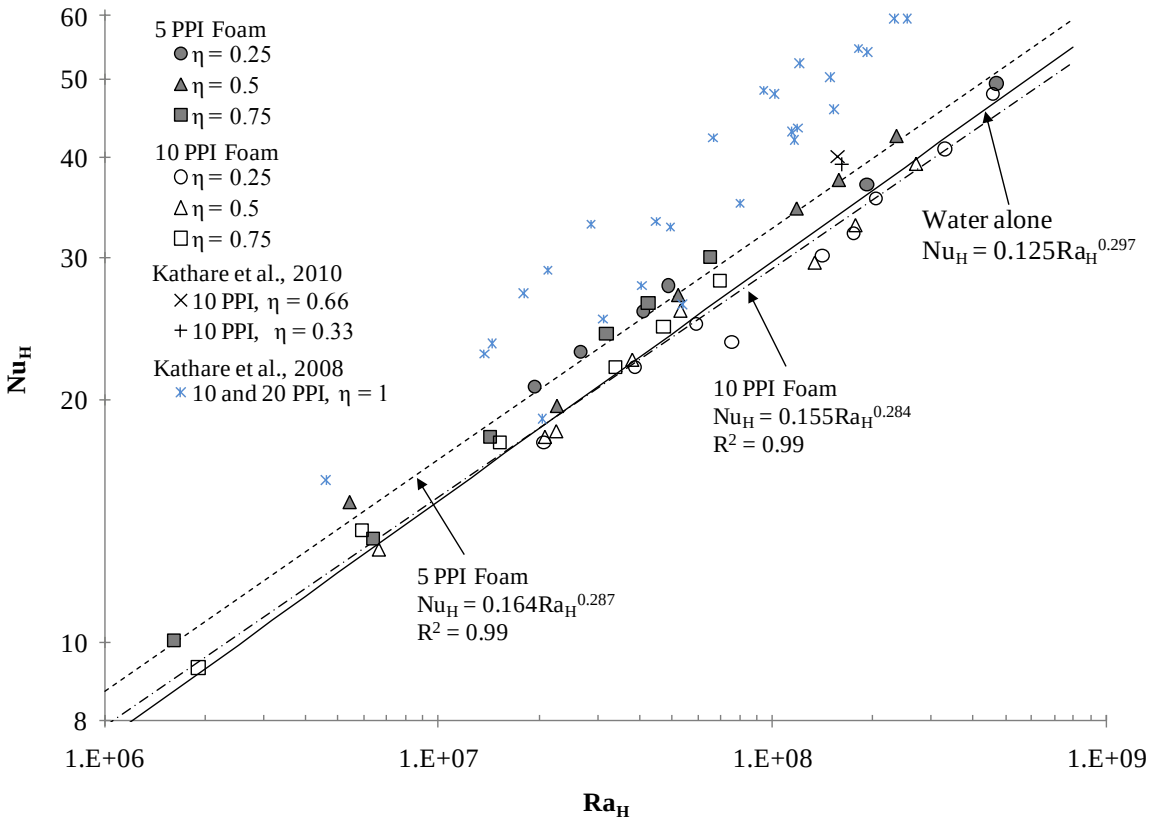

Figure 4.5. Nusselt vs. Rayleigh number for 5 and 10 PPI foam on the hot boundary alone as a function of η. Shown with data of Kathare et al. for η = 1 [13], 0.66 and 0.33 [14]. Solid line is a correlation for water alone developed in the current study. Dashed line is a correlation for 5 PPI foam. Dash-dot line is a correlation for 10 PPI foam.

diffuses in series from the foam to the fluid layer, substantially reducing the apparent conductivity of the two layer system. For example, using Eq. (3.16) with $\eta = 0.5$, $k_f = 0.6$ W/mK and $k_m = 10$ W/mK the apparent conductivity of the two layer system is 1 W/mK, an order of magnitude less than if the enclosure was fully filled with porous media. Conversely, when the enclosure is filled with a conductive foam, such as copper, a direct conduction path exists from the hot and cold boundary and the apparent conductivity is equal to the medium conductivity, 10 W/mK.

Power law correlations for 5 and 10 PPI foam, where data for all η is included in each correlation, are shown below. The correlations are also shown in Figure 4.5. The

correlation for 5 PPI foam is

$$\mathrm{Nu_H} = 0.164\mathrm{Ra_H^{0.287}} \tag{4.4}$$

with $R^2 = 0.99$ and for $1.6 \times 10^6 < \mathrm{Ra_H} < 4.7 \times 10^8$.

The correlation for 10 PPI foam is

$$\mathrm{Nu_H} = 0.155\mathrm{Ra_H^{0.284}} \tag{4.5}$$

with $R^2 = 0.99$ and for $1.9 \times 10^6 < \mathrm{Ra_H} < 4.6 \times 10^8$. The confidence interval, $\mathrm{SEE} \cdot t_{\alpha,\nu}/\sqrt{N}$, of both fits is 2%. A data point is considered an outlier if its standard residual is greater than the t-statistic evaluated at a 95% confidence level ([actual Nusselt number – predicted Nusselt number]/SEE > $t_{\alpha,\nu}$). Because the residuals are assumed to be normally distributed, if the residual divided by the standard error is greater than the t-statistic, then it lies outside of the 95% confidence bound for the distribution of the residuals. The 10 PPI data point at $\mathrm{Ra_H} = 7.6 \times 10^7$, $\mathrm{Nu_H} = 24$, is determined to be an outlier. The outlier is not included when determining the correlation. The two correlations have similar exponents (0.287 for 5 PPI, and 0.284 for 10 PPI), though the pre-exponential factor for the 5 PPI foam, 0.164, is larger than that for 10 PPI foam, 0.155 showing that the 5 PPI foam offers an approximately constant advantage over 10 PPI foam. The data also show this trend with a single exception for the two $\eta = 0.75$ experiments at $\mathrm{Ra_H} \approx 6 \times 10^6$. The 5 PPI foam has greater permeability than the 10 PPI foam. For the same η, 5 PPI foam has a larger Darcy number ($\mathrm{Da} = K/H_p^2$) than the 10 PPI foam and offers less resistance to flow, allowing the convection cells to penetrate deeper into the porous layer, increasing heat transfer for the 5 PPI foam.

Hypothesis testing is performed to determine if the variation in the data with respect to η is statistically significant. Separate correlations were determined for each η and PPI, where the exponent is set equal to exponent for the correlation that includes all data for each PPI. The individual correlations were then compared to the correlation that includes all data to determine if the difference is statistically significant. The correlations and the results of the hypothesis testing are shown in Table 4.6. The 5 PPI foam is not a function of η. The variation in the 10 PPI, η = 0.25 and 0.5 data is not significant. The pre-exponential factor for η = 0.75 is 4% higher than the pre-exponential factor for the correlation that considers all η, which is significant to a 95% confidence level (p_{value} = 0.03). Detailed results of the hypothesis testing are provided in Appendix D.

Variation in Nusselt number with changing η is a balance between enhanced thermal diffusion and suppressed fluid advection. As the foam thickness increases, the apparent conductivity of the composite system increases and more heat is removed from the hot boundary by conduction. Increasing η also inhibits the removal of heat from the hot boundary by advection in two ways. Increasing η effectively reduces the Rayleigh number for the fluid region as the interface temperature between the porous layer and the fluid layer decreases and the height of the fluid layer decreases. With a lower fluid Rayleigh number, advection is weaker and the flow penetrates less deeply into the porous layer. When the foam layer thickness is increased, the fluid region is also moved further from the hot boundary. Both of these effects mean a greater portion of the foam layer is stagnant for a given Rayleigh number. This trend was predicted by Poulikakos [18] as increasing porous layer height reduced flow penetration into the porous layer and reduced

Table 4.6. Result of hypothesis testing to determine if variation in Nusselt number with changing η is statistically significant.

Case	Correlation	R^2	Difference between case including all η and case for a single η significant (95% confidence)?
5 PPI, all η	$Nu_H = 0.164Ra_H^{0.287}$	0.99	----
5 PPI, η = 0.25	$Nu_H = 0.165Ra_H^{0.287}$	0.98	No
5 PPI, η = 0.5	$Nu_H = 0.164Ra_H^{0.287}$	0.99	No
5 PPI, η = 0.75	$Nu_H = 0.164Ra_H^{0.287}$	0.98	No
10 PPI, all η	$Nu_H = 0.155Ra_H^{0.284}$	0.99	----
10 PPI, η = 0.25	$Nu_H = 0.151Ra_H^{0.284}$	0.97	No
10 PPI, η = 0.5	$Nu_H = 0.153Ra_H^{0.284}$	0.99	No
10 PPI, η = 0.75	$Nu_H = 0.161Ra_H^{0.284}$	0.99	Yes

Nusselt number for low conductivity porous media. For the present results, the tradeoff between increased diffusion and decreased advection, with the addition of metal foam, appear to be balanced as the relationship between the Nusselt and Rayleigh numbers changes very little with changing porous height.

Figure 4.6 is a plot of enhancement in heat transfer with metal foam over water alone, E, defined in Eq. (3.22), as a function of Rayleigh number for 5 and 10 PPI foam. The enhancement observed by Kathare et al. [13] for an enclosure fully filled with 10 and 20 PPI copper foam is also shown. The 10 PPI results of Kathare et al. [13] show enhancement ranging from 1.2 to 1.6. The variation in enhancement is due to variation in Darcy number (Figure 2.9). For the present data, the average enhancement factor for 5 and 10 PPI foam is 1.1 and 0.98 respectively. For 10 PPI foam, enhancement is a slight function of η where the average enhancement for each η is respectively 1.11, 1.11, 1.12, for η = 0.25, 0.5, 0.75. The plot of enhancement confirms the trends observed in

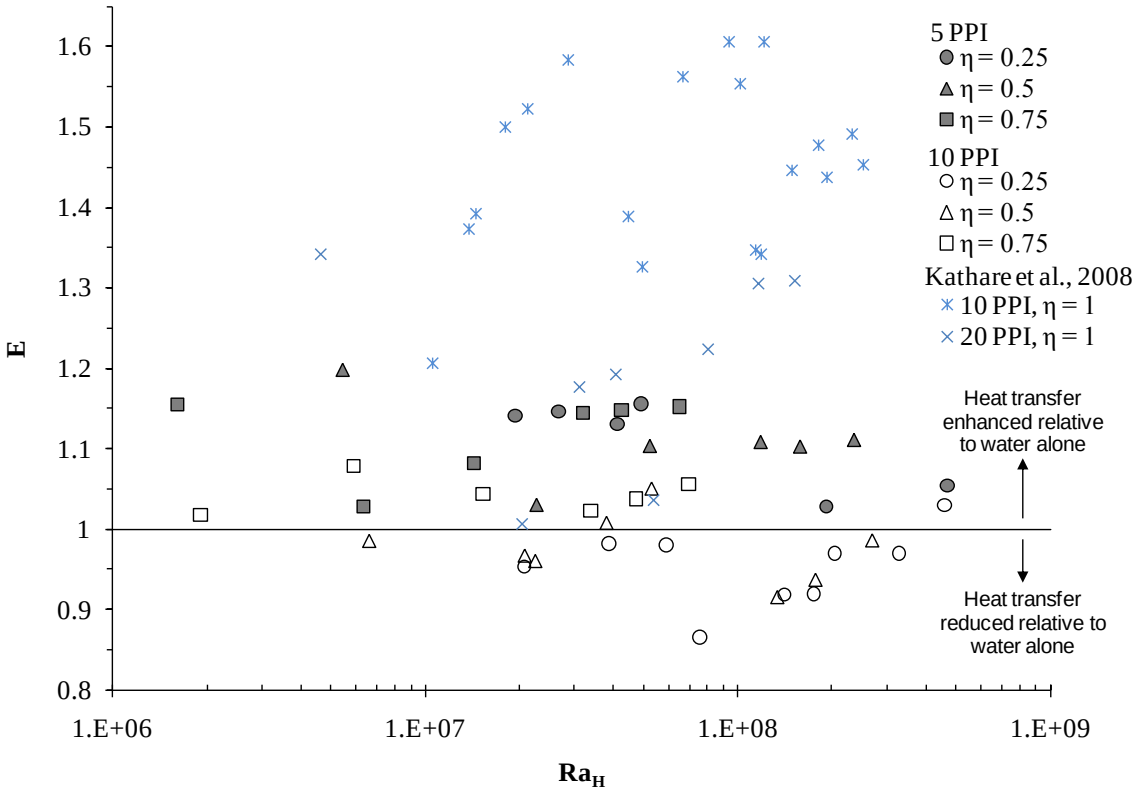

Figure 4.6. Enhancement in heat transfer as a function of Rayleigh number for 5 and 10 PPI foam with $\eta = 0.25$, 0.5, and 0.75 on the hot boundary alone. Data of Kathare et al. [13] for $\eta = 1$ with 10 and 20 PPI copper foam also shown.

Figure 4.5 with the results of Kathare et al. [13] offering consistently higher enhancement than the present results and the 5 PPI foam providing more enhancement in heat transfer than the 10 PPI foam.

Figure 4.7 is a plot of advection enhancement, E_{adv}, defined in Eq. (3.23). As expected, the 5 PPI foam, with greater permeability than the 10 PPI foam, provides greater enhancement in advection in all cases with the exception of $\eta = 0.75$ at $Ra_H \approx 6 \times 10^6$. Figure 4.7 shows that the 10 PPI, $\eta = 1$ case provides greater enhancement in advection than the 10 PPI, $0.25 \leq \eta \leq 0.75$, cases. This result supports

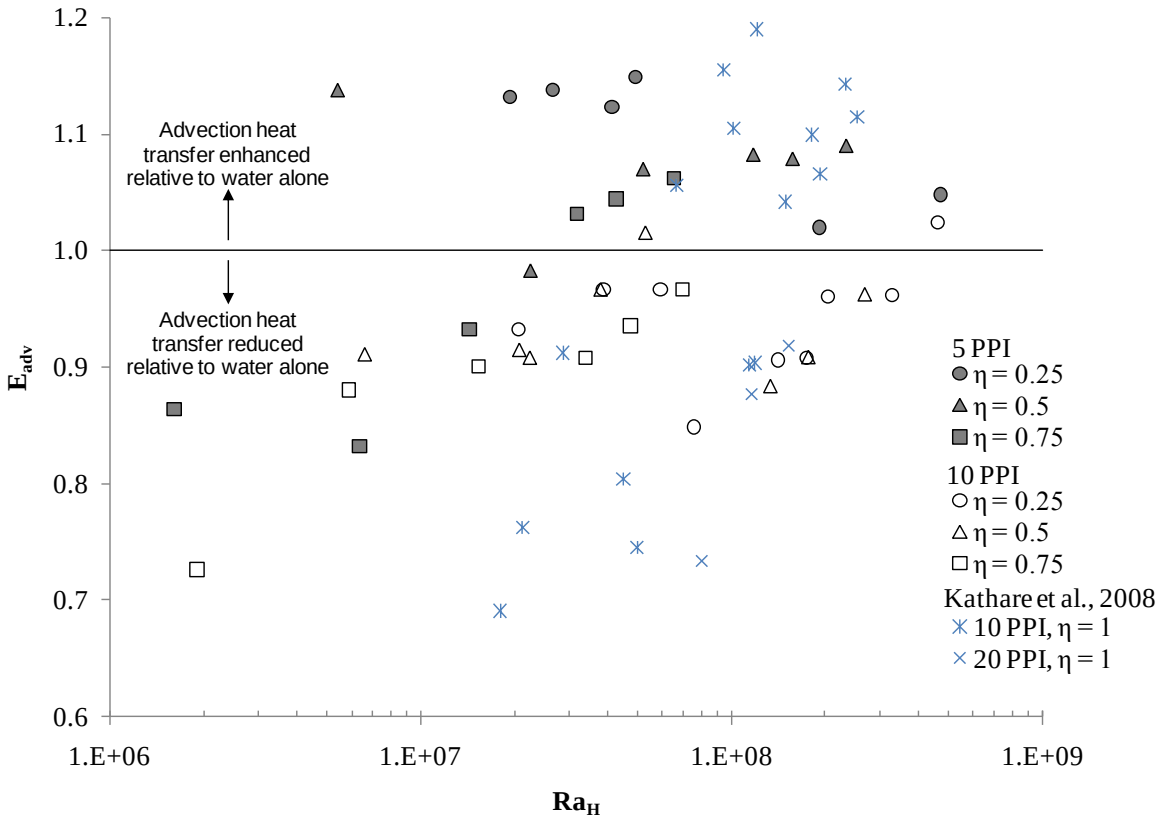

Figure 4.7. Advection enhancement as a function of Rayleigh number for 5 and 10 PPI foam on the hot boundary alone with η = 0.25, 0.5, and 0.75. Data of Kathare et al. [13] for η = 1 with 10 and 20 PPI copper foam also shown.

the suggestion that the Nusselt number for the partially filled enclosure case is reduced, compared to a foam filled enclosure, because of suppression of advection associated with limited flow penetration into the porous layer.

4.3.1.2. Heat Transfer Correlations for Foam on the Hot Boundary Alone

Based on their experiments for natural convection with a horizontal layer of metal foam in an infinite domain, Bhattacharya and Mahajan [5] suggest a correlation of the form $Nu_H = CRa_H^m Da^n$ where the exponent for the Rayleigh number is for the case with no foam, m = 0.297 for the present experiments, and the Darcy number is $Da = K/H_p^2$. This correlation is appropriate for natural convection velocities where the Darcy drag

dominates over the Forchheimer drag as the Forchheimer term is not accounted for in the correlation. For natural convection in an enclosure with a horizontal layer of copper foam, Kathare et al. [13] found Darcy drag to dominate over Forchheimer drag with the ratio of Forchheimer drag to Darcy drag not exceeding 0.18. With limited Forchheimer drag relative to Darcy drag, the correlation proposed by Bhattacharya and Mahajan [5] may be appropriate. The 5 and 10 PPI foam are shown correlated together in Figure 4.8. The correlation is,

$$\mathrm{Nu_H} = 0.155\mathrm{Ra_H^{0.297}Da^{0.021}} \tag{4.6}$$

with $R^2 = 0.97$ and for $6.8 \times 10^{-5} < \mathrm{Da} < 1.4 \times 10^{-3}$ and $1.6 \times 10^{6} < \mathrm{Ra_H} < 4.7 \times 10^{8}$. The confidence interval of the fit is 2.3%. The 10 PPI data point at $\mathrm{Ra_H} = 7.6 \times 10^{7}$, $\mathrm{Nu_H} = 24$ is determined to be an outlier. The correlation collapses the data at the high and low Rayleigh numbers though the data in the middle Rayleigh number range are still segregated by foam type with 5 PPI noticeably higher than the 10 PPI data. The Darcy number dependence is weak with a Darcy term exponent of 0.021. With the correlated data segregated by pore density, the correlation suggested by Bhattacharya and Mahajan [5] does not accurately represent the present data.

Experiments with foam on the hot boundary are also correlated using porous media variables. The form suggested by the dimensional analysis of Wang and Bejan [34] and utilized by Kathare et al. [13] for Rayleigh-Bénard equivalent convection in an enclosure filled with copper foam is used for the present results. Porous media variables are defined for the entire test section of the composite system with $\mathrm{Ra_{m,s}}$, $\mathrm{Nu_{m,s}}$, and $\mathrm{Pr_{p,s}}$

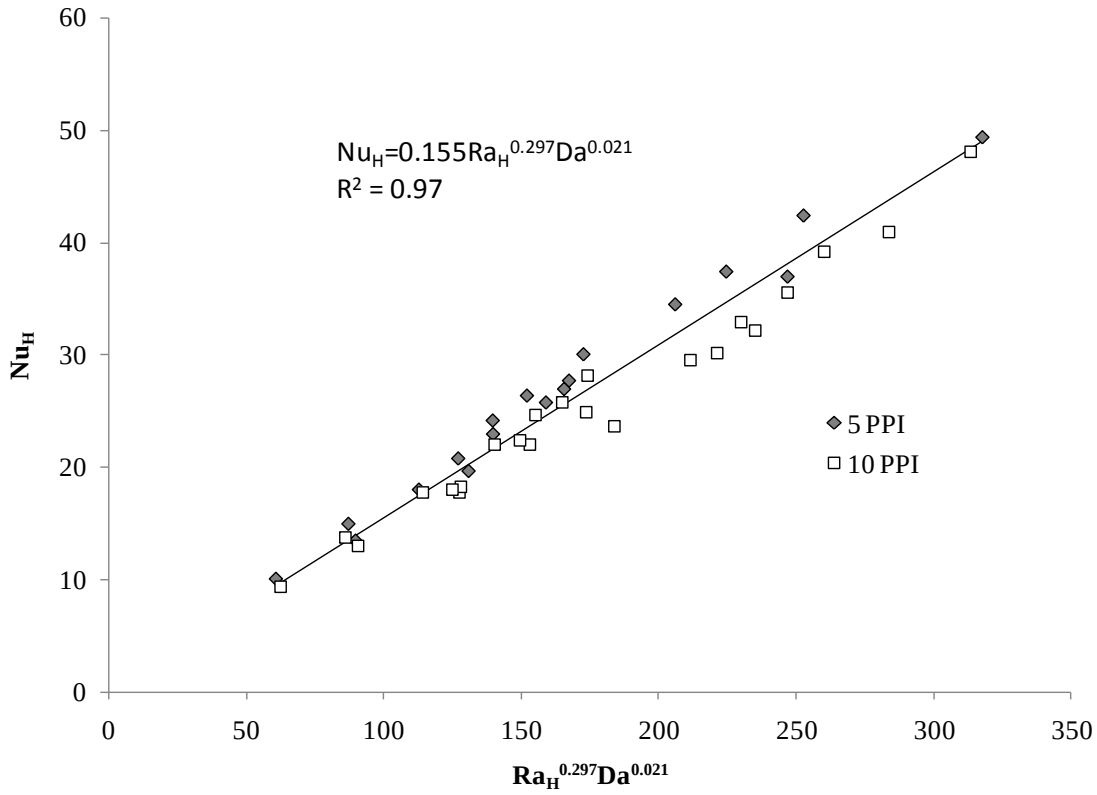

Figure 4.8. Nusselt number versus product of Rayleigh number and Darcy number for 5 and 10 PPI foam on the hot boundary. Solid line is a correlation considering all data. The dashed lines show the confidence interval of the correlation.

defined in Eqs. (3.17), (3.18) and (3.21). When $\eta = 1$, $Ra_{m,s} = Ra_m$, $Nu_{m,s} = Nu_m$, and $Pr_{p,s} = Pr_p$. The results shown in Figure 4.9 are well correlated as

$$Nu_{m,s} = 0.013 Ra_{m,s}^{0.506} Pr_{p,s}^{0.376} \tag{4.7}$$

for $202 < Ra_{m,s} < 8079$ and $579 < Pr_{p,s} < 19655$. The data are correlated with a confidence interval of 3% and $R^2 = 0.98$. The 10 PPI data point at $Ra_{m,s} = 631$, $Nu_{m,s} = 14$ is determined to be an outlier. With differing correlations, the results of Kathare et al. [13], with copper foam and $\eta = 1$, do not follow the present results for $0.25 < \eta < 0.75$. Though the modified porous media equations account for differences in

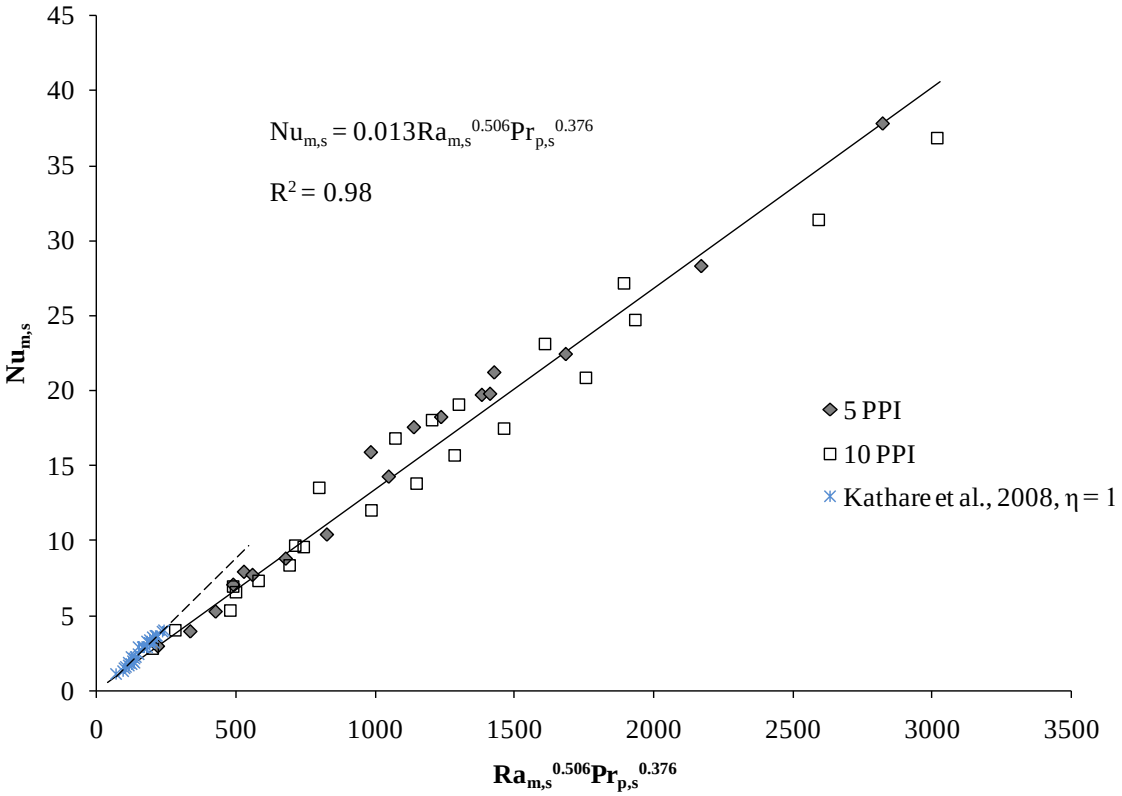

Figure 4.9 Medium Nusselt number as a function of medium Rayleigh number and $Pr_{p,s}$ for 5 and 10 PPI copper foam on the hot boundary with a superposed fluid layer. Shown with the data of Kathare et al. [13] for 10 and 20 PPI copper foam filled enclosure. The dashed line is the trendline for the data of Kathare et al. [13].

apparent conductivity, based on the discussion of the previous section, it is not unexpected that the present results differ from the results of Kathare et al. [13], as the two cases have significantly different flow fields.

4.3.2. Foam on Both Boundaries

A plot of Nusselt number versus Rayleigh number for 10 PPI foam on both boundaries for $\eta = 0.5,\ 0.75$ is shown in Figure 4.10. Eq. (4.1), a Nusselt number correlation for water alone, determined in the same apparatus as the experiments with foam, is shown as a solid line. The results of Kathare et al. [13] for copper foam with

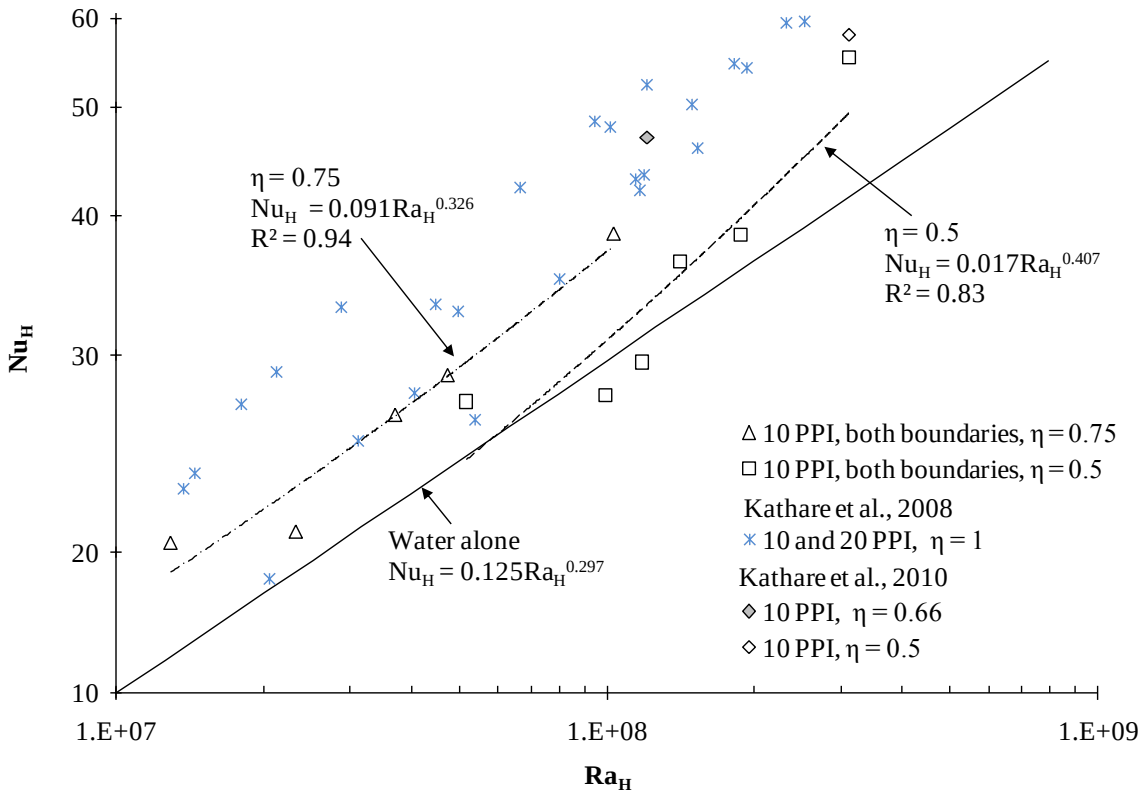

Figure 4.10. Nusselt number versus Rayleigh number for 10 PPI foam on both boundaries as a function of η with data of Kathare et al. for η = 1 [13], 0.66 and 0.5 [14]. The correlation for water alone is shown as a solid line. The correlation for 10 PPI foam on both boundaries and η = 0.5 is shown with a dash-dot line. The correlation for 10 PPI foam on both boundaries and η = 0.75 is shown as a dashed line.

η = 1, and the both boundary results of Kathare et al. [14] for copper foam η = 0.66 and 0.5, are also shown in Figure 4.10. The Nusselt number of Kathare et al. [14] for 10 PPI copper foam and η = 0.5, $Nu_H = 57.9$, is similar to the value of $Nu_H = 55.3$ in the present study for η = 0.5 at the same Rayleigh number, $Ra_H = 3 \times 10^8$. The Nusselt number of Kathare et al. [14] for η = 0.66 at $Ra_H = 2 \times 10^8$ is 47.0. Experiments were not performed at η = 0.66 in the present experiments, but the value of Kathare et al. [14] for η = 0.66 is significantly above $Nu_H = 38.6$ for η = 0.75 at $Ra_H = 1 \times 10^8$ in the present experiments.

For each η, increasing Rayleigh number from 5×10^7 to 1×10^8 for $\eta = 0.5$ and 1×10^7 to 2×10^7 for $\eta = 0.75$, yields no increase in the Nusselt number, suggesting the test section may be stagnant at the lowest Rayleigh numbers. If the temperature at the foam-fluid interface is estimated by assuming one-dimensional conduction through the foam layers, fluid Rayleigh numbers can be estimated for the fluid region ($H - 2H_p$). The lowest estimates for the Rayleigh numbers of the fluid region are $Ra_{(H-2Hp)} = 1 \times 10^6$ and $Ra_{(H-2Hp)} = 2 \times 10^4$ for $\eta = 0.5$ and 0.75, respectively. In both cases, the Rayleigh number estimate is well above the onset of Rayleigh-Bénard for fluid alone, $Ra_H = 1708$. The estimate of the fluid Rayleigh number for the fluid region of the test section suggests the test section at the lowest Rayleigh number for each η may be experiencing convection. The lack of increase in Nusselt number may be due to a changing number of convection cells as observed by Prasad [22] and Poulikakos [18] for the case with porous media on the hot boundary alone, or an increase in aspect ratio (H/D) from 0.4 to 0.6 for $\eta = 0.5$ and from 0.27 to 0.4 for $\eta = 0.75$.

The present results are segregated with respect to η. The $\eta = 0.5$ and 0.75 data are correlated separately in the form $Nu_H = CRa_H^{\eta}$. The correlation for $\eta = 0.5$ is

$$Nu_H = 0.017 Ra_H^{0.407} \tag{4.8}$$

with a confidence interval of $\frac{+15\%}{-13\%}$, $R^2 = 0.83$, for $5.2 \times 10^7 < Ra_H < 3.1 \times 10^8$. The correlation for $\eta = 0.75$ is

$$Nu_H = 0.091 Ra_H^{0.326} \tag{4.9}$$

with a confidence interval of $\frac{+11\%}{-10\%}$, $R^2 = 0.94$, for $1.3 \times 10^7 < Ra_H < 1.0 \times 10^8$. The

limited number of data points and spread in the data lead to large confidence intervals for both fits. The data, however, do show a clear segregation between $\eta = 0.5$ and $\eta = 0.75$. Over the range of Rayleigh numbers when the two sets of data overlap, the $\eta = 0.75$ experiments yield higher Rayleigh numbers. However, the $\eta = 0.5$ Nusselt numbers increase more quickly with Rayleigh number than the $\eta = 0.75$ data. As the correlations follow from the data, the $\eta = 0.75$ correlation has a greater pre-exponential factor, and the $\eta = 0.5$ correlation has a greater exponent. The balance between the suppression of advection and enhancement of conduction with the addition of high conductivity copper foam is apparent in the correlations for $\eta = 0.5$ and 0.75. An enclosure with $\eta = 0.75$ has more high conductivity foam and greater enhancement in heat transfer due to increased thermal diffusion, but the additional foam also provides increased suppression of advection. At low Rayleigh numbers when conduction provides a greater portion of the heat transfer, an enclosure with $\eta = 0.75$ will yield higher Nusselt numbers, but at higher Rayleigh numbers when advection is more significant, an enclosure with $\eta = 0.5$ will provide more heat transfer.

Figure 4.11 is a plot of enhancement versus Rayleigh number. Enhancement is shown for $\eta = 0.5$ and 0.75 for 10 PPI foam on the hot boundary and on both boundaries, as well as enhancement for 10 and 20 PPI with $\eta = 1$ from Kathare et al. [13]. For the 10 PPI foam on both boundaries and $\eta = 0.5$ and 0.75, if the data points at the lowest Rayleigh number for each η are neglected, enhancement strongly increases with increasing Rayleigh number. The hot boundary enhancement decreases slightly with increasing Rayleigh number. Spreading the total amount of foam on the two boundaries

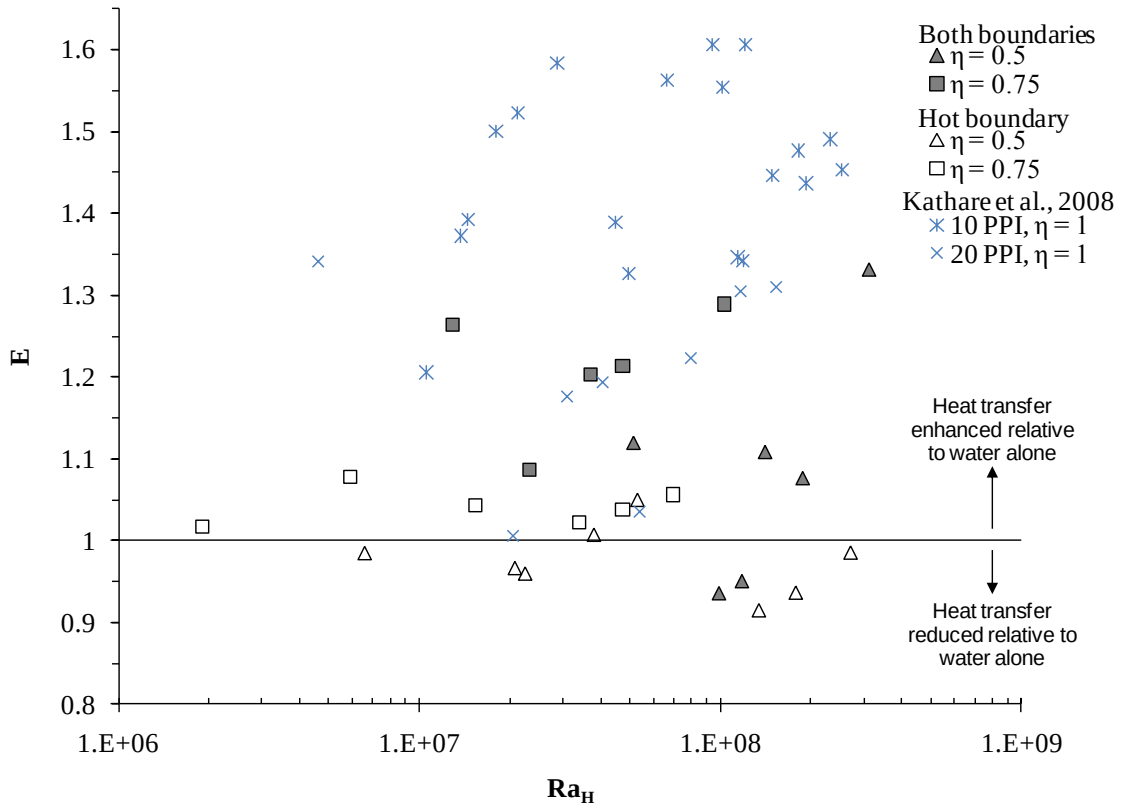

Figure 4.11. Enhancement in heat transfer as a function of Rayleigh number for η = 0.5 and 0.75 for 10 PPI foam on both boundaries. Data of Kathare et al. [13] for η = 1 with 10 and 20 PPI copper foam also shown.

does not affect heat transfer for a stagnant enclosure as the apparent conductivity of the two cases is the same. The effect may also be minimal for lower Rayleigh numbers when conduction heat transfer is still comparable to advection heat transfer. At higher Rayleigh numbers when advection dominates, placing the foam on both boundaries appears to provide less resistance to flow, increasing advection heat transfer. Compared to foam on one boundary, there is half the amount of foam on each boundary for a given η. With the foam split between the two boundaries, the total penetration into the foam layer may increase, decreasing the amount of stagnant fluid in the enclosure. The

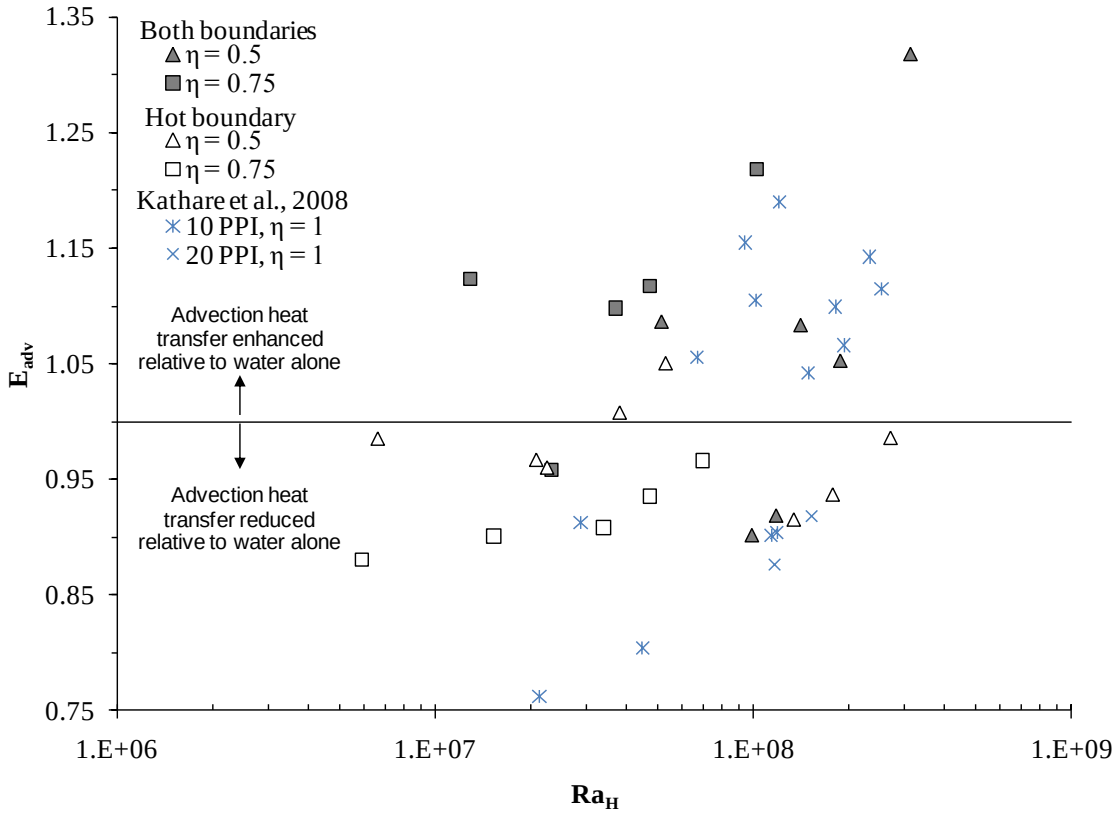

Figure 4.12. Advection enhancement as a function of Rayleigh number for 5 and 10 PPI foam with η = 0.25, 0.5, and 0.75. Data of Kathare et al. [13] for η = 1 with 10 and 20 PPI copper foam also shown.

enhanced penetration at higher Rayleigh numbers leads to more fluid participating in advection and higher Nusselt numbers. This trend is shown in Figure 4.12, which is a plot of the advection enhancement as a function of Rayleigh number. The advection enhancement is similar to the total enhancement. With foam on the hot boundary, neglecting the data point at the lowest Rayleigh number for each η, advection enhancement increases rapidly with increasing Rayleigh number, while advection enhancement does not vary with Rayleigh number for foam on the hot boundary.

As shown in Figure 4.12, the advection enhancement of 10 PPI foam on both boundaries and an enclosure filled with 10 PPI foam is similar. However, the direct conduction path offered by the fully filled enclosure means the total enhancement (Figure 4.11) for the fully filled case is larger than the case with foam on both boundaries. In Figure 4.11, the enhancement with foam on both boundaries reaches ≈ 1.3 for both η, while the enhancement for a fully filled enclosure reaches ≈ 1.6 at a similar Rayleigh number.

As with foam on the hot boundary alone, data with foam on both boundaries are correlated using porous media variables. The results are shown in Figure 4.13 and Eq. (4.10)

$$\mathrm{Nu}_{m,s} = 0.037\mathrm{Ra}_{m,s}^{0.559}\mathrm{Pr}_{p,s}^{0.234} \tag{4.10}$$

for $271 < \mathrm{Ra}_{m,s} < 2537$ and $2231 < \mathrm{Pr}_{p,s} < 14104$. The data are well correlated with a confidence interval of ±5% and $R^2 = 0.99$. The correlation is extended with a dashed line to cover the data range of Kathare et al. [13], with η = 1. The data of Kathare et al. [13], with η = 1, are accurately explained by the correlation, Eq. (4.10). Plotting the two sets of data in porous media variables accounts for the differences in apparent conductivity. The close matching of the two sets of data when plotted with porous media variables verifies the similarities in the advection heat transfer that were shown in the advection enhancement plot, Figure 4.12.

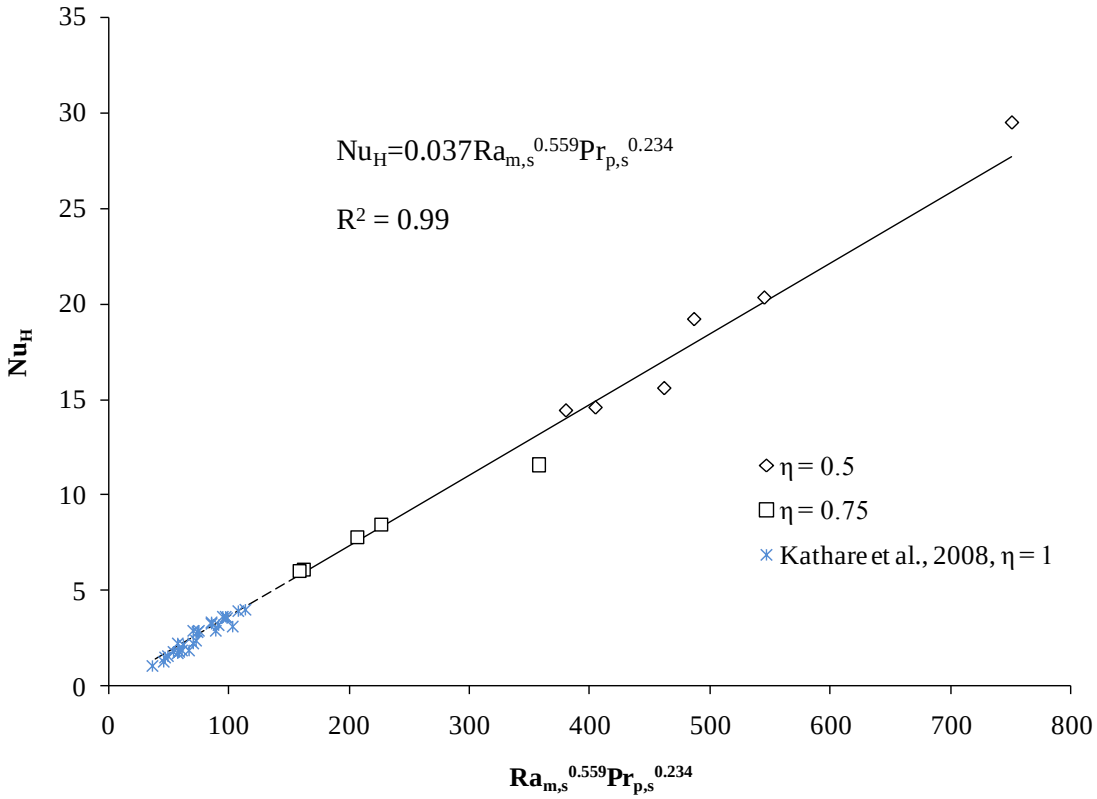

Figure 4.13. Medium Nusselt number as a function of medium Rayleigh number and $Pr_{p,s}$ for 10 PPI on both boundaries. Only the data with $\eta = 0.5$ and 0.75 are included in the correlation. The correlation is extended with the dashed line to cover the data range of Kathare et al. [13], with $\eta = 1$.

CHAPTER 5 CONCLUSIONS AND RECOMMENDATIONS

In 2007, Kathare et al. [14] briefly studied Rayleigh-Bénard equivalent convection with copper foam and a superposed layer of water. Their results were limited to four experiments, two with foam on the hot boundary alone and two with foam on both boundaries. The results showed that in the same circumstances, an enclosure partially filled with copper foam may provide similar enhancement in heat transfer over a water layer alone to an enclosure fully filled with copper foam. The present results expand the work of Kathare et al. [14] to provide a more complete set of experiments, including the variation of Nusselt number with Rayleigh number, porous height, pore density and foam placement. Four sets of heat transfer experiments are performed: (1) Rayleigh-Bénard convection in a water filled enclosure for $9 \times 10^5 < Ra_H < 3 \times 10^8$, (2) and (3) Rayleigh-Bénard equivalent convection with 5 and 10 PPI copper foam adjacent to the hot boundary with a superposed fluid layer for $\eta = 0.25$, 0.5 and 0.75, and $2 \times 10^6 < Ra_H < 5 \times 10^8$, and (4) 10 PPI foam adjacent to both boundaries, with a layer of water in the center of the enclosure, for $\eta = 0.5$ and 0.75, and $1 \times 10^7 < Ra_H < 3 \times 10^8$.

The porosity of the copper foam samples ranges from 0.880 to 0.918. The effective conductivity of the foam samples ranged from 8.9 ± 0.6 to 11 ± 1 W/mK. For the 10 PPI foam samples with porosity of 0.916, the permeability and drag coefficient are 1.6×10^{-7} m^2 and 0.061, respectively. For the 10 PPI foam samples with porosity of 0.88, the permeability and drag coefficient are 1.0×10^{-7} m^2 and 0.077, respectively. For the 5 PPI foam samples with porosity of 0.89, the permeability and drag coefficient are 2.3×10^{-7} m^2 and 0.10, respectively.

Heat transfer correlations are developed for cases with foam on the hot boundary and foam on both boundaries. For 5 PPI foam on the hot boundary alone, the data are well correlated as

$$\mathrm{Nu_H} = 0.164\mathrm{Ra_H^{0.287}} \tag{4.4}$$

with $R^2 = 0.99$, and for $1.6 \times 10^6 < \mathrm{Ra_H} < 4.7 \times 10^8$. For 10 PPI foam, the data are well correlated as

$$\mathrm{Nu_H} = 0.155\mathrm{Ra_H^{0.284}} \tag{4.5}$$

with $R^2 = 0.99$, and for $1.9 \times 10^6 < \mathrm{Ra_H} < 4.6 \times 10^8$. There are two key findings associated with these correlations. First, because the correlations have similar exponents, but the 5 PPI foam has a larger pre-exponential factor, the 5 PPI foam offers an approximately 6% advantage over the 10 PPI foam. Because the two foams have similar effective conductivities, the ~6% advantage is attributed to the greater permeability of the 5 PPI foam. Higher permeability allows convection cells to penetrate deeper into the foam layer, reducing the suppression of advection associated with the addition of porous media. Second, the correlations are not a function of the foam height. The addition of more copper foam does not provide additional enhancement in heat transfer for $0.25 \leq \eta \leq 0.75$. This result suggests that for copper foam on one boundary, and $0.25 \leq \eta \leq 0.75$, the increased thermal diffusion associated with the addition of copper foam is balanced by the increased suppression of advection with the addition of more foam.

Comparing enhancement in heat transfer over a water layer, the results show that placing the foam on both boundaries provides more enhancement than when foam is placed on the hot boundary alone. Furthermore, while the enhancement with foam on the hot boundary decreases slightly with increasing Rayleigh number, the enhancement with foam on both boundaries increases with increasing Rayleigh number. Because the total amount of foam is the same, this difference is attributed to a decrease in the suppression of advection when foam is placed on both boundaries. With the foam split between the two boundaries, the total penetration into the foam layer may increase, decreasing the amount of stagnant fluid in the enclosure and increasing the Nusselt number.

With foam on both boundaries, the Nusselt number depends on the porous layer height. The correlation for $\eta = 0.5$ is

$$\mathrm{Nu_H} = 0.017\mathrm{Ra_H^{0.407}} \tag{4.8}$$

with $R^2 = 0.83$, for $5.2 \times 10^7 < \mathrm{Ra_H} < 3.1 \times 10^8$. The correlation for $\eta = 0.75$ is

$$\mathrm{Nu_H} = 0.091\mathrm{Ra_H^{0.326}} \tag{4.9}$$

with $R^2 = 0.94$, for $1.3 \times 10^7 < \mathrm{Ra_H} < 1.0 \times 10^8$. Because the suppression of advection is less severe with foam on both boundaries, the porous height has a greater effect on the heat transfer than with foam on the hot boundary alone. At low Rayleigh numbers when conduction provides a greater portion of heat transfer, an enclosure with $\eta = 0.75$ will yield higher Nusselt numbers, but at higher Rayleigh numbers when advection is more significant, an enclosure with $\eta = 0.5$ will provide more heat transfer.

The 10 PPI foam on the hot boundary does not enhance heat transfer with an average enhancement factor of 0.98. The 5 PPI foam on the hot boundary enhances heat transfer by 10% on average. With foam on both boundaries, enhancement is a function of Rayleigh number and porous height. Enhancement increases with Rayleigh number. Over the range of Rayleigh numbers tested, enhancement for $\eta = 0.5$ ranged from 0.93 at $Ra_H = 1 \times 10^8$, to 1.33 at $Ra_H = 3 \times 10^8$. For $\eta = 0.75$, enhancement ranged from 1.09 at $Ra_H = 2 \times 10^7$, to 1.29 at $Ra_H = 1 \times 10^8$. When the enclosure was filled with foam, in the experiments of Kathare et al. [13], enhancement is not a strong function of Rayleigh number with enhancement from 1.2 to 1.6, though enhancement is typically above 1.35. A partially filled enclosure provides significantly less enhancement in heat transfer compared to a fully filled enclosure. With heat diffusing in series from the foam layer(s) to the water layer, the apparent conductivity of the composite system is ≈ 0.8, 1, and 2 W/mK for $\eta = 0.25$, 0.5 and 0.75, while the apparent conductivity of the foam filled case is equal to the medium conductivity, ≈ 10 W/mK. The increased thermal diffusion is the primary reason the filled enclosure case provides better heat transfer than the partially filled case. When foam is on the hot boundary, limited penetration into the porous layer provides an additional penalty to heat transfer, further reducing the benefit of the metal foam.

Correlations are also presented using porous media variables to describe the system with an enclosure partially filled with foam. With foam on the hot boundary, the data are well correlated as

$$\mathrm{Nu}_{m,s} = 0.013 \mathrm{Ra}_{m,s}^{0.506} \mathrm{Pr}_{p,s}^{0.376} \tag{4.7}$$

for $202 < Ra_{m,s} < 8079$ and $579 < Pr_{p,s} < 19655$ and $R^2 = 0.98$. The dimensionless groups $Nu_{m,s}$, $Ra_{m,s}$, and $Pr_{p,s}$, are the porous media variables modified to account for the lower apparent conductivity of the composite system. The results for $\eta = 1$ do not fall on to the line produced by this correlation. With foam on both boundaries, the results are correlated as

$$Nu_{m,s} = 0.037 Ra_{m,s}^{0.559} Pr_{p,s}^{0.234} \tag{4.10}$$

for $271 < Ra_{m,s} < 2537$ and $2231 < Pr_{p,s} < 14104$ and $R^2 = 0.99$. The results of Kathare et al. [13], with $\eta = 1$, fall on the line of the above correlation.

A more extensive experimental study or a combined experimental and numerical study is necessary to better understand the physical mechanisms behind the present results. With foam on one boundary, it is necessary to investigate porous heights below 0.25 or above 0.75 to find the transition from water-like behavior to partially filled enclosure behavior or from fully filled enclosure behavior to partially filled enclosure behavior. With limited foam samples, the results for foam on both boundaries are limited. Experimentation is necessary over a greater range of Rayleigh numbers, dimensionless porous heights and pore densities. Finally, an experimentally validated numerical model will help to understand the physical basis for the results in this study.

REFERENCES

[1] V. V. Calmidi and R. L. Mahajan, "Forced convection in high porosity metal foams," *ASME Journal of Heat Transfer*, vol. 122, pp. 557-565, 2000.

[2] W. Lu and C. Y. Zhao, "Thermal analysis on metal-foam filled heat exchangers. Part I: Metal-foam filled pipes," *International Journal of Heat and Mass Transfer*, vol. 49, pp. 2751-2761, 2006.

[3] C. Y. Zhao and W. Lu, "Thermal analysis on metal-foam filled heat exchangers. Part II: Tube heat exchangers," *International Journal of Heat and Mass Transfer*, vol. 49, pp. 2762-2770.

[4] C. Y. Zhao, T. Kim, T. J. Lu, and H. P. Hodson, "Thermal transport in high porosity cellular metal foams," *Journal of Thermophysics and Heat Transfer*, vol. 18, no. 3, pp. 309-317, 2004.

[5] A. Bhattacharya and R. L. Mahajan, "Finned metal foam heat sinks for electronics cooling in forced convection," *Journal of Electronic Packaging*, vol. 124, no. 3, pp. 155-163, 2002.

[6] K. Boomsma, D. Poulikakos, and F. Zwick, "Metal foams as compact high performance heat exchangers," *Mechanics of Materials*, vol. 35, no. 12, pp. 1161-1176, December 2003.

[7] W. H. Shih, W.C. Chiu, and W.H. Hsieh, "Height effect on heat-transfer characteristics of aluminum-foam heat sinks," *Journal of Heat Transfer*, vol. 128, no. 6, pp. 530-537, 2006.

[8] S. Mahjoob and K. Vafai, "A synthesis of fluid and thermal transport models for metal," *International Journal of Heat and Mass Transfer*, vol. 51, pp. 3701-3711, 2008.

[9] A. Bhattacharya and R. L. Mahajan, "Metal foam and finned metal foam heat sinks for electronics cooling in buoyancy-induced convection," *Journal of Electronic Packaging*, vol. 128, pp. 259-266, 2006.

[10] M. S. Phanikumar and R. L. Mahajan, "Non-Darcy natural convection in high porosity metal foams," *International Journal of Heat and Mass Transfer*, vol. 45, pp. 3781-3793, June 2002.

[11] C. Y. Zhao, T. J. Lu, and H. P. Hodson, "Natural convection in metal foams with open cells," *International Journal of Heat and Mass Transfer*, vol. 48, pp. 2452-2463, 2005.

[12] S. Krishnan, J. Y. Murthy, and S. V. Garimella, "A two temperature model for the analysis of passive thermal control systems," *Journal of Heat Transfer*, vol. 126, pp. 628-637, 2004.

[13] V. Kathare, J. H. Davidson, and F. A. Kulacki, "Natural convection in water-saturated metal foam," *International Journal of Heat and Mass Transfer*, vol. 51, no. 15-16, pp. 3794-3802, July 2008.

[14] V. Kathare, F. A Kulacki, and J. H. Davidson, "Buoyant convection in superposed metal foam and water layers," *Journal of Heat Transfer*, vol. 132, January 2010.

[15] F. Chen and C. F. Chen, "Onset of finger convection in a horizontal porous layer underlying a fluid layer," *Journal of Heat Transfer*, vol. 110, pp. 403-409, 1988.

[16] F. Chen and C. F. Chen, "Convection in superposed fluid and porous layers," Journal of Fluid Mechanics, vol. 234, pp. 97-119, 1992.

[17] S. J. Kim and Choi C. Y., "Convective heat transfer in porous and overlying fluid layers heated from below," *International Journal of Heat and Mass Transfer*, vol. 39, no. 2, pp. 319-329, 1996.

[18] D. Poulikakos, "Buoyancy-driven convection in a horizontal fluid layer extending over a porous substrate," *Physics of Fluids*, vol. 29, no. 12, pp. 3949-3957, 1986.

[19] D. Poulikakos, A. Bejan, B. Selimos, and K. R. Blake, "High Rayleigh number convection in a fluid overlaying a porous bed," *International Journal of Heat and Fluid Flow*, vol. 7, no. 2, pp. 109-116, 1986.

[20] V. Prasad and Q. Tian, "An experimental study of thermal convection in fluid-superposed porous layers heated from below," in *9th International Heat Transfer Conference*, Jerusalem, 1990, pp. 207-212.

[21] V. Prasad, K. Brown, and Q. Tian, "Flow visualization and heat transfer experiments in fluid-superposed packed beds heated from below," *Experimental Thermal and Fluid Science*, vol. 4, pp. 12-24, 1991.

[22] V. Prasad, "Flow instabilities and heat transfer in fluid overlying horizontal porous layers," *Experimental Thermal and Fluid Science*, vol. 6, no. 2, pp. 135-146, 1993.

[23] S. Chandra, "Experimental study of free convection in fluid porous layers heated from below," University of Minnesota, Minneapolis, Masters Thesis 2006.

[24] D. A. Nield and A. Bejan, *Convection in Porous Media*. New York: Springer-Verlag, 2006.

[25] ERG Aerospace. (2009, December) [Online]. http://www.ergaerospace.com

[26] S. Krishnan, J. Y. Murthy, and S. V. Garimella, "Direct simulation of transport in open-cell metal foam," *ASME Journal of Heat Transfer*, vol. 128, pp. 793-799, August 2006.

[27] M. Kaviany, *Principles of Heat Transfer in Porous Media*. New York: Springer-Verlag, 1995.

[28] K. Vafai and C. L. Tien, "Boundary and inertia effects on flow and heat transfer in porous media," *International Journal of Heat and Mass Transfer*, vol. 24, pp. 195-203, 1981.

[29] V. V. Calmidi and R. L. Mahajan, "The effective thermal conductivity of high porosity fibrous metal foams," *ASME Journal of Heat Transfer*, vol. 121, pp. 466-471, 1999.

[30] A. Bhattacharya, V. V. Calmidi, and R. L. Mahajan, "Thermophysical properties of high porosity metal foams," *International Journal of Heat and Mass Transfer*, vol. 45, pp. 1017-1031, 2002.

[31] K. Boomsma and D. Poulikakos, "On the effective thermal conductivity of a three-dimensionally structured fluid-saturated metal foam," *International Journal of Heat and Mass Transfer*, vol. 44, pp. 827-836, 2001.

[32] V. Kathare, "Natural convection in water-saturated metal foam," University of Minnesota, Minneapolis, Masters Thesis 2007.

[33] J. W. Elder, "Steady free convection in a porous medium heated from below," *Journal of Fluid Mechanics*, vol. 27, pp. 29-48, 1967.

[34] M. Wang and A. Bejan, "Heat transfer correlation for Bénard convection in a fluid saturated porous layer," I*nternational Communications in Heat and Mass Transfer*, vol. 14, pp. 617-626, 1987.

[35] E. R. Lapwood, "Convection of a fluid in a porous medium," *Proceedings of Cambridge Philosophical Society*, pp. 508-521, 1948.

[36] F. Incropera and D. DeWitt, *Fundamentals of Heat and Mass Transfer*, 5th ed. New York: John Wiley & Sons, 2002.

[37] J. H. Davidson, F. A. Kulacki, and D. Savela, "Natural convection in water-saturated reticulated vitreous carbon foam," *International Journal of Heat and Mass Transfer*, vol. 52, pp. 4479-4483, 2009.

[38] A. M. Garon and R. J. Goldstein, "Velocity and heat transfer measurements in thermal convection," *The Physics of Fluids*, vol. 16, pp. 1818-1825, 1973.

[39] R. S. Figliola and D. E. Beasley, *Theory and Design for Mechanical Measurements*, 2nd ed. New York: John Wiley and Sons, Inc., 1995.

[40] A. Hayter, *Probability and Statistics for Engineers and Scientists*, 3rd ed.: Thomson Higher Education, 2007.

[41] "ANSI/ASME Power Test Codes-PTC 19.1, Measurement uncertainty," American Society of Mechanical Engineers, New York, 1983.

[42] T. Jonsson and I. Catton, "Prandtl number dependence of natural convection in porous media," *ASME Journal of Heat Transfer*, vol. 109, pp. 371-377, May 1987.

[43] F. Chen and C. F. Chen, "Experimental investigation of convective stability in a superposed fluid and porous layer when heated from below," *Journal of Fluid Mechanics*, vol. 207, pp. 311-321, 1989.

[44] V.V. Calmidi and R.L. Mahajan, "The effective thermal conductivity of high porosity fibrous metal foams," *ASME Journal of Heat Transfer*, vol. 121, pp. 466-471, 1999.

[45] M. Wang and A. Bejan, "Heat transfer correlation for Bénard convection in a fluid saturated porous layer," *International Communications in Heat and Mass Transfer*, vol. 14, pp. 617-626, 1987.

APPENDIX A UNCERTAINTY ANALYSIS

Uncertainty analysis is based on the recommendations in [39]. In the discussion of uncertainty analysis the data are assumed to follow a normal distribution. A 95% confidence level is assumed for all uncertainty calculations. The uncertainty of fluid and solid properties is assumed to be zero. Elemental uncertainties are combined to determine the total uncertainty using the root-sum-squares (RSS) method. For a measurement x with elemental errors e_k, the total uncertainty in x is

$$u_x = \sqrt{\sum_{k=1}^{K} e_k^2} \tag{A.1}$$

For the relationship $y = f(x_1, x_2, x_3, \ldots)$, the uncertainty in y, U_y, is determined through propagation of errors using the RSS method

$$U_y = \sqrt{\left(\frac{\partial y}{\partial x_1}\right)^2 U_{x_1}^2 + \left(\frac{\partial y}{\partial x_2}\right)^2 U_{x_2}^2 + \left(\frac{\partial y}{\partial x_3}\right)^2 U_{x_3}^2 \ldots} \tag{A.2}$$

where U_{x_1}, U_{x_2}, and U_{x_3} are the uncertainties of x_1, x_2, and x_3. For functions that are composed only of a product of measured values, a special form of Eq. (A.2) can be used to determine the relative uncertainty. For the relationship $y = f(x_1, x_2, x_3, \ldots) = C x_1^a x_2^b x_3^c \ldots$, the relative uncertainty in y is

$$\frac{u_y}{y} = \sqrt{\left(\frac{a u_{x_1}}{x_1}\right)^2 + \left(\frac{b u_{x_2}}{x_2}\right)^2 + \left(\frac{c u_{x_3}}{x_3}\right)^2 \ldots} \tag{A.3}$$

A.1. Uncertainty in Temperature Measurement

Uncertainty in temperature measurement is determined from two sources: bias uncertainty associated with thermocouple calibration, and precision uncertainty associated with measurement of temperatures.

A.1.1. Estimate of Thermocouple Bias Error

The bias error in thermocouple measurements is determined through calibration against a three wire, Class A, platinum resistance temperature detector (RTD). Calibration occurs in a Julabo F12 water bath capable of maintaining a constant temperature to ±0.3 °C. An ice bath at 0 °C is used for the thermocouple reference temperature. The same Keithley 2700 DMM and 7708 multiplexing card used in the experiments, and two thermocouples used to measure heat loss during experiments, are used for calibration. The results of the calibration are shown in Table A.1 and Figure A.1. The average of a minimum of 16 measurements over a time of approximately 100 seconds is reported for each thermocouple, at each temperature. The RTD resistance was measured before (#1 in Table A.1) and after (#2) the thermocouple measurements were taken. The resistance of the RTD wires, which was subtracted from the RTD measured resistance, was measured before and after calibration.

The calibration is used to correct the indicated thermocouple measurements by assuming the temperature of the RTD is the true temperature. The relationship between thermocouple temperature and the RTD temperature is determined using ordinary least squares

$$T_{TC} = 0.995T_{RDT} + 0.0416 \quad \text{(A.4)}$$

Table A.1. Results of thermocouple calibration using platinum RTD as reference standard. RTD measurements are taken before (#1) and after (#2) thermocouple measurements. Two thermocouples, TC_1 and TC_2, were used for calibration.

T_{RTD}, #1 (°C)	T_{RTD}, #2 (°C)	T_{TC1} (°C)	T_{TC2} (°C)	T_{RTD}, Avg. (°C)	T_{TC} Avg. (°C)	$T_{TC} - T_{RDT}$ (°C)
4.74	4.75	4.77	4.77	4.74	4.77	0.025
9.73	9.72	9.72	9.71	9.72	9.72	-0.005
14.73	14.73	14.70	14.69	14.73	14.69	-0.036
19.74	19.73	19.68	19.68	19.73	19.68	-0.055
24.73	24.73	24.65	24.64	24.73	24.64	-0.087
29.73	29.73	29.62	29.60	29.73	29.61	-0.115
34.74	34.73	34.58	34.58	34.73	34.58	-0.151
39.73	39.72	39.59	39.56	39.73	39.58	-0.150
44.74	44.73	44.56	44.55	44.73	44.55	-0.183
49.74	49.74	49.54	49.54	49.74	49.54	-0.200

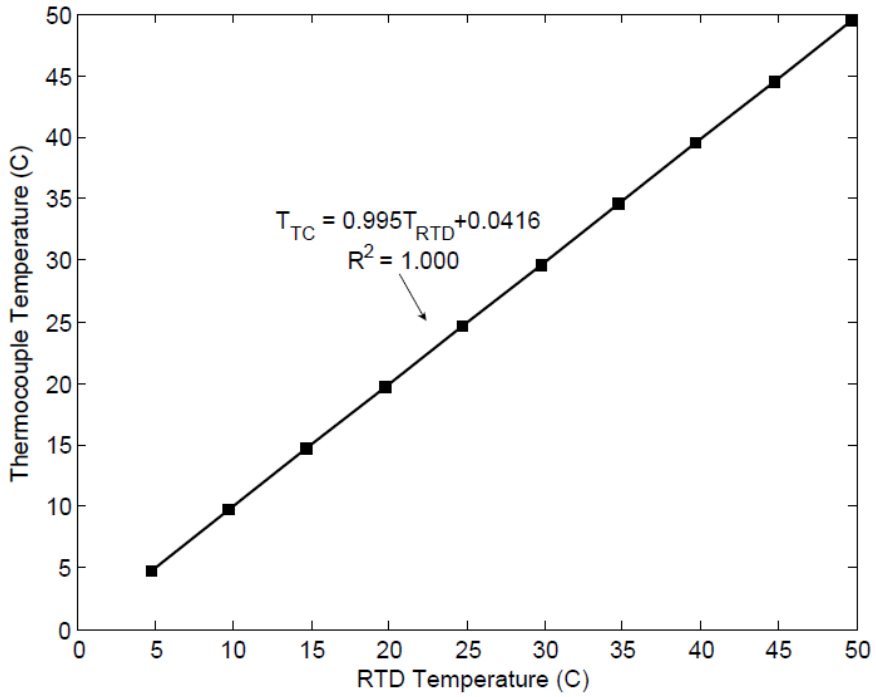

Figure A.1. Results of thermocouple calibration using platinum RTD as reference standard. Thermocouple temperature versus RTD temperature with equation of linear fit.

To correct thermocouple measurements the relationship is rearranged

$$T_{RTD} = T_{TC,corrected} = \frac{T_{TC} - 0.0416}{0.995} \tag{A.5}$$

The experimental thermocouple measurements are corrected to determine the true temperature using Eq. (A.5). The uncertainty in Eq. (A.5), considered the bias error in thermocouple measurements, has two components: uncertainty in the RTD measurement and uncertainty in the linear fit of Eq. (A.4).

The accuracy in the resistance measurement using a Keithely 2700 DMM, for the range of 100Ω, is $R \times 10^{-4} + 2 \times 10^{-3}$ (Ω) where R is the measured resistance. The resolution is 1×10^{-4} Ω. The uncertainty in the resistance, the RSS combination of accuracy and resolution error, is propagated through the equation for RTD temperature to determine the uncertainty in the RTD temperature due to uncertainty in measured resistance. The Class A RTD has a temperature accuracy of $0.15 + 0.002T_{RTD}$ (°C). The accuracy of the RTD and uncertainty in temperature due to uncertainty in resistance are combined using RSS to determine the total uncertainty in the RTD measurement.

The confidence interval associated with the linear fit of Eq. (A.4) , $SEE \cdot t/\sqrt{N}$, is 0.00649. This value is propagated through Eq. (A.5) to determine the uncertainty in Eq. (A.5) due to curve fitting. The total uncertainty of Eq. (A.5) is the RSS combination of the uncertainty due to curve fitting and the uncertainty in the RTD measurement. The total uncertainty of Eq. (A.5) is dominated by the accuracy of the RTD. Shown in

Figure A.2 the total uncertainty of Eq. (A.5) is a linear function of temperature.

$$\text{Bias Error in TC measurements} = 0.001997T_{TC,corrected} + 0.1505 \quad \text{(A.6)}$$

where $T_{TC,corrected}$ is the thermocouple measurement after correction using Eq. (A.5).

A.1.2. Estimate of Mean Temperatures

Multiple thermocouples are used to determine the average temperatures of the cold, hot and separator plates and the regions on the outer portion of the cylinder used for measuring heat loss. The mean temperature of each thermocouple, j, is

$$\overline{T}_j = \frac{1}{M}\sum_{i=1}^{M} T_{ji} \quad \text{(A.7)}$$

where M is the total number of measurements for each thermocouple. The mean temperature of each plate is determined by averaging the mean of the individual thermocouple measurements

$$\overline{T} = \frac{1}{N}\sum_{j=1}^{N} \overline{T}_j \quad \text{(A.8)}$$

where N is the number of thermocouples on each plate. Two sources of precision error are recognized during temperature measurement. First, though temperature data are acquired during steady operation, time variation in thermocouple measurements does exist, leading to scatter in the data at individual thermocouple locations. Second, spatial variation is observed at the various thermocouple locations on each plate and on the

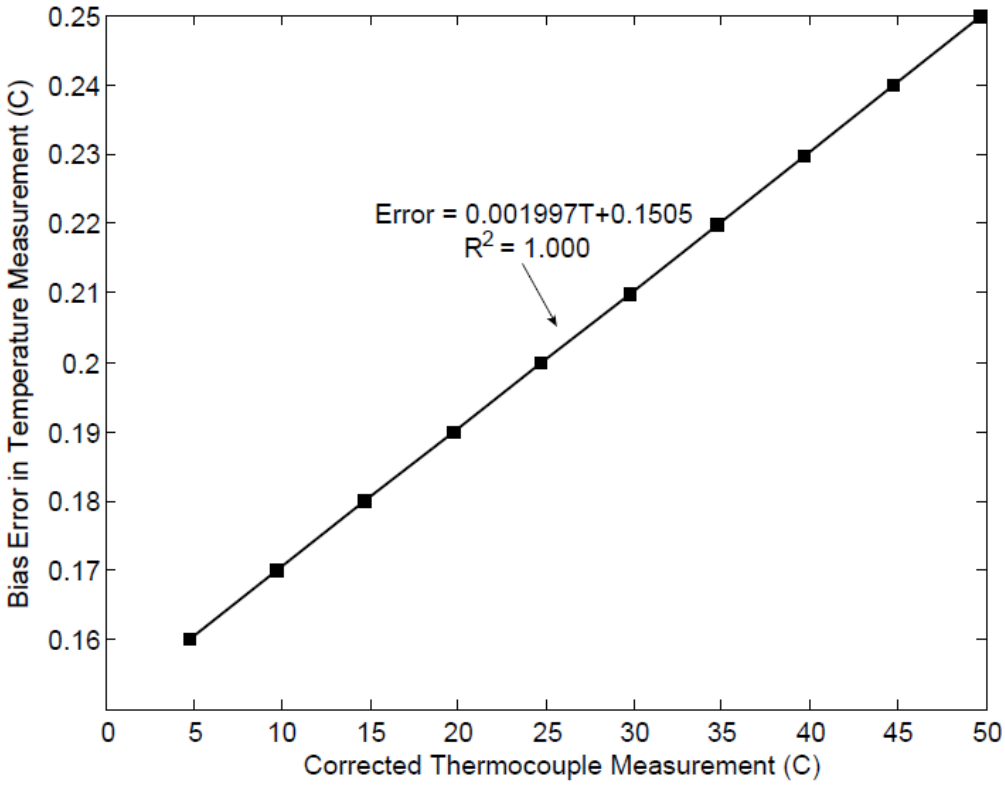

Figure A.2. Bias error in corrected thermocouple measurements as a function of corrected thermocouple temperature.

outside of the cylinder. The RSS method is used to combine the two sources of error to determine an overall precision error for steady temperature measurement. The spatial variation dominates the total uncertainty.

A.1.3. Temperature Uncertainty Associated with Temperature Measurement – Temporal Variations

Both the temperature of each thermocouple and the distribution of temperatures on each surface vary randomly in time. To account for both of these temporal variations, a pooled sample standard deviation is used. The pooled standard deviation can be thought of as an RSS average of the temporal variation in temperature of each

thermocouple embedded into a particular surface. The sample standard deviation for each thermocouple, j, is

$$S_{T_j} = \sqrt{\frac{1}{M-1}\sum_{i=1}^{M}\left(T_{ji} - \overline{T}_j\right)^2} \tag{A.9}$$

where $\overline{T}_j$ is the mean of the individual thermocouple and M is the number of samples obtained for each thermocouple. The pooled standard deviation of T is

$$\langle S_T \rangle = \sqrt{\frac{1}{N}\sum_{j=1}^{N} S_{Tj}^2} \tag{A.10}$$

where $\langle\ \rangle$ denotes a pooled quantity, and N is the total number of thermocouples on each plate. The sample standard deviation of T is a measure of the variation of individual measurements. Because the mean temperature measurement is used in data analysis, variation of the sample mean about the true mean is necessary. The variation of the sample mean about the true mean is characterized by the standard deviation of the sample mean, $S_{\overline{T}}$, which is a function of sample standard deviation, S_T, and number of samples. Again, pooled statistics are used. The pooled standard deviation of the mean of T is

$$S_{\overline{T},\text{temporal}} = \langle S_{\overline{T}} \rangle = \frac{\langle S_T \rangle}{(MN)^{1/2}} \tag{A.11}$$

where the degrees of freedom are $\nu_{\text{temporal}} = N\,(M-1)$.

A.1.4. Temperature Uncertainty Associated with Temperature Measurement – Spatial Variations

Spatial variation of temperature across the plate surface is characterized by the standard deviation of the average temperature at each thermocouple location

$$S_T = \sqrt{\frac{1}{N-1}\sum_{j=1}^{N}\left(\overline{T}_j - \overline{T}\right)^2} \tag{A.12}$$

where $\overline{T}$ is the average plate temperature from Eq. (A.7), $\overline{T}_j$ is the average steady temperature of each thermocouple and N is the number of thermocouples on each surface. Again, the standard deviation of the mean temperature is necessary

$$S_{\overline{T},spatial} = S_{\overline{T}} = \frac{S_T}{\sqrt{N}} \tag{A.13}$$

with degrees of freedom $\nu_{spatial} = N - 1$.

A.1.5. Temperature Uncertainty Associated with Temperature Measurement – Total Uncertainty

The overall standard deviation is

$$S_{\overline{T}} = \sqrt{\left(S_{\overline{T},temporal}\right)^2 + \left(S_{\overline{T},spatial}\right)^2} \tag{A.14}$$

Because the two sources of error have different degrees of freedom, the degrees of freedom used in evaluating the t-value is estimated using the Welch-Satterthwaite formula.

$$\nu = \frac{\left[\left(S_{\overline{T},temporal}\right)^2 + \left(S_{\overline{T},spatial}\right)^2\right]^2}{\left[\left(S_{\overline{T},temporal}\right)^4/\nu_{temporal}\right] + \left[\left(S_{\overline{T},spatial}\right)^4/\nu_{spatial}\right]} \tag{A.15}$$

The precision error in the average temperature of each plate is

$$P_T = t_{\nu,P} S_{\bar{T}} \tag{A.16}$$

where $t_{\nu,P}$, is the t-statistic from Student's t-distribution for normal distributions with finite sample sizes, ν is the degrees of freedom, P in the subscript is the confidence level at which the precision error is evaluated (95%).

The total uncertainty is the RSS of the precision and bias errors

$$U_T = \sqrt{{P_T}^2 + {B_T}^2} \tag{A.17}$$

A.1.6. Uncertainty in the Temperature Difference Across Hot and Cold Plate

The uncertainty in the temperature difference across the hot and cold plate, $\Delta T = T_h - T_c$, is

$$U_{\Delta T} = \sqrt{\left(U_{T_h}\right)^2 + \left(U_{T_c}\right)^2} \tag{A.18}$$

A.2. Uncertainty Power Input

The total power input is the difference between the power input by the primary heater and the loss through the base and sides of the apparatus.

$$Q = Q_p - Q_L \tag{A.19}$$

The uncertainty in the power is

$$U_Q = \sqrt{\left(U_{Q_p}\right)^2 + \left(U_{Q_L}\right)^2} \tag{A.20}$$

where U_{Q_p}, the uncertainty in the primary heat power, and U_{Q_L}, the uncertainty in the

Table A.2. Resolution and accuracy of voltage measurement.

Range (V)	Resolution (V)	Accuracy (V)
100	1×10^{-4}	$0.006(V_p) + 0.0008(100)$
750	0.001	$0.006(V_p) + 0.0008(750)$

heat loss are discussed in the following sections. The heat loss uncertainty was less than 2.7% for all experiments.

A.2.1. Uncertainty in Primary Heater Power

The uncertainty in the primary heater power is determined using propagation of error. The primary heater power is

$$Q_p = \frac{V_p^2}{R} \tag{A.21}$$

The uncertainty in the primary heater power is

$$U_{Q_p} = Q_p \sqrt{\left(\frac{2U_{V_p}}{V_p}\right)^2 + \left(\frac{U_R}{R}\right)^2} \tag{A.22}$$

where U_{V_p}, the uncertainty in the voltage measurement and U_R, the uncertainty in the resistance measurement are discussed below.

A.2.1.1. Voltage Measurement Uncertainty

The uncertainty in the voltage measurement using the Keithley model 2700 digital multimeter with a Keithley model 7708 multiplexing card is 0.6% of reading +.08% of the range for all ranges. For voltage measurements ranging from approximately 60 V to 115 V, two measurement ranges are encountered: 100 V and 750 V. Table A.2, lists the

Table A.3. Uncertainty associated with DAQ equipment for voltage measurement.

Range (V)	$u_{V,DAQ}$
100	$\sqrt{\left[\frac{1\times10^{-4}}{2}\right]^2+\left[0.006(V_p)+0.0008(100)\right]^2}$
750	$\sqrt{\left[\frac{0.001}{2}\right]^2+\left[0.006(V_p)+0.0008(750)\right]^2}$

uncertainty associated with the data acquisition system for each range. In Table A.2, V_p is the voltage of the primary heater. The uncertainties associated with data acquisition, the resolution error and the accuracy, are combined using the RSS method, shown in Table A.3. The precision error associated with temporal variation in steady state voltage measurement is

$$P_V = t_{\nu,P} S_{\overline{V}} \tag{A.23}$$

where $t_{\nu,P}$ is the t-value for degrees of freedom ν, evaluated at the probability P (95%) and $S_{\overline{V}}$ is the standard deviation of the means of the voltage. The total uncertainty of the voltage measurement is determined using the RSS method

$$u_V = \sqrt{(P_V)^2 + \left(u_{V,DAQ}\right)^2} \tag{A.24}$$

A.2.1.2. Heater Electrical Resistance Uncertainty

A Fluke 85 digital multimeter is used to measure the resistance. The accuracy of a Fluke 85 digital multimeter is $\pm(2\% + 0.2)\ \Omega$. For a primary heater resistance of $218.9\ \Omega$, the uncertainty of the resistance measurement is $u_R = 0.64\ \Omega$.

A.2.2. Uncertainty in Heat Loss Calculation

Neglecting the uncertainty in the radial heat loss, the uncertainty in the heat loss is estimated through the uncertainty in the loss through the separator plate. Neglecting uncertainty in dimensional measurements and polycarbonate conductivity heat loss, uncertainty is

$$U_{Q_L} \approx U_{Q_{L_1}} \approx \sqrt{\left(U_{T_{S_1}}\right)^2 + \left(U_{T_{S_2}}\right)^2} \tag{A.25}$$

A.3. Uncertainty in Porosity

The porosity is $\phi = \frac{V_t - V_s}{V_t}$, where V_t is the total volume of the cylinder of metal foam and V_s is the volume of the solid portion of the metal foam cylinder. The uncertainty in the measurement of porosity is,

$$U_\phi = \sqrt{\left[\left(\frac{1}{V_t} - \frac{V_t - V_s}{V_t^2}\right) U_{V_t}\right]^2 + \left[\frac{U_{V_s}}{V_t}\right]^2} \tag{A.26}$$

where the uncertainty in the total volume, U_{V_t}, and the uncertainty in the volume of the solid portion of the foam, U_{V_s}, is described next. The relative uncertainty in the porosity measurement was less than ±0.15%.

The total volume of the foam is

$$V_t = \frac{\pi D^2}{4} \cdot t \tag{A.27}$$

where D is foam diameter and t is foam thickness. The uncertainty in the total volume is

$$U_{V_t} = V_t \sqrt{\left(\frac{2U_D}{D}\right)^2 + \left(\frac{U_t}{t}\right)^2} \tag{A.28}$$

The diameter and thickness of the foam samples were measured with a Mitutoyo digital caliper (Model: CD-6" csx) with a resolution of 0.01 mm and an accuracy of 0.02 mm. Multiple measurements were obtained for each sample. The uncertainty in the thickness and diameter were calculated using

$$U_D, U_t = \sqrt{(U_{res})^2 + \left(U_{accuracy}\right)^2 + \left(U_{precision}\right)^2} \tag{A.29}$$

where U_{res} = resolution/2 = 0.005 mm, $U_{accuracy}$ is the accuracy of the caliper (0.02 mm) and $U_{precision}$ is the precision error associated with multiple measurements as in Eq. (A.16).

Ignoring the mass of the air filling the void space of the foam, the volume of the solid portion of the foam is,

$$V_s = \frac{m_{foam}}{\rho_{foam}} \tag{A.30}$$

where m_{foam} is the mass of the foam and, ρ_{foam} is the density of the copper alloy used to construct the foam. Neglecting the uncertainty in the density of the copper alloy, the uncertainty in the volume of the solid portion of the foam is

$$U_{V_s} = V_s \cdot \sqrt{\left(\frac{U_{m_{foam}}}{m_{foam}}\right)^2} = V_s \cdot \frac{U_{m_{foam}}}{m_{foam}} \tag{A.31}$$

The foam mass was measured using a OHAUS precision standard TS400D balance with resolution error of 5×10^{-6} kg, reproducibility error of 7×10^{-6} kg, and a linearity error of 1×10^{-5} kg. Multiple measurements were obtained with no variation, making the

precision error associated with multiple measurements zero. The total uncertainty in the mass measurement is the RSS of the individual errors.

A.4. Uncertainty in the Permeability and Forchheimer (Drag) Coefficient

To determine the permeability and drag coefficient, the pressure drop across a foam sample is measured as air of known velocity flows through the test section. Using a Meriam laminar flow meter, the volumetric flow rate of air (m^3/s) is

$$\vartheta = B \cdot \Delta P + C \cdot \Delta P^2 (181.8718/183.992) \tag{A.32}$$

where B = 52.4158, C = -0.151760 and ΔP is the pressure drop across the flow meter measured with an inclined manometer. The total uncertainty in volumetric flow rate is the RSS of accuracy of the flow meter (0.72% of reading) and the uncertainty due to the resolution of the manometer used to measure pressure drop across the flow meter. The uncertainty in the flow rate due to the resolution of the manometer is

$$U_\vartheta = \left[B + 2C\Delta P \left(\frac{181.8718}{183.992}\right)\right] U_{\Delta P} \tag{A.33}$$

where B and C are defined above and $U_{\Delta P}$=0.01. The velocity (m/s) is defined as

$$U = \frac{\vartheta}{\left(\frac{\pi D^2}{4}\right)} \tag{A.34}$$

The uncertainty in the velocity from the uncertainty in the volumetric flow rate is

$$\frac{U_U}{U} = \sqrt{\left(\frac{U_\vartheta}{\vartheta}\right)^2 + \left(\frac{2U_D}{D}\right)^2} \tag{A.35}$$

At the lowest velocity, the uncertainty in the measurement of velocity is at most ± 51%. At the highest velocity, the uncertainty is at most ± 5%.

The pressure drop across the foam sample is measured using a Dwyer micromanometer with a resolution of 0.0005 inches of water column. The uncertainty in the reading of the micromanometer is assumed to equal the resolution error of the micromanometer, $U_{\Delta P}$ =0.0005/2 inches of water column. The uncertainty of the pressure drop divided by foam thickness, $\Delta P/H_p$, is

$$\frac{U_{(\Delta P/H_p)}}{\Delta P/H_p} = \sqrt{\left(\frac{U_{\Delta P}}{\Delta P}\right)^2 + \left(\frac{U_{H_p}}{H_p}\right)^2} \tag{A.36}$$

At the lowest velocity, the uncertainty in the measurement of $\Delta P/H_p$ is at most ± 50%. At the highest velocity the uncertainty is at most ± 4%.

Eq. (2.4) is used to determine the permeability and drag coefficient

$$\frac{\Delta P}{H_p} = -\frac{\mu_f}{K}U - \frac{C_F}{K^{1/2}}\rho_f U^2 \tag{2.4}$$

Plotting $\frac{\Delta P}{H_p}$ vs. U, the terms $-\frac{\mu_f}{K}$ and $-\frac{C_F}{K^{1/2}}\rho_f$ are the coefficients a and b for a second order polynomial of the form

$$\frac{\Delta P}{H_p} = aU + bU^2 \tag{A.37}$$

The uncertainty in the coefficients a and b are 12 and 9%, respectively, for 10 PPI foam with ϕ = 0.88, 10 and 8%, respectively, for 10 PPI foam with ϕ = 0.92, and 33 and 14%,

respectively, for 5 PPI foam with $\phi = 0.89$. As a function of the coefficients a and b, the permeability and drag coefficient are

$$K = \frac{\mu_f}{a} \tag{A.38}$$

$$C_f = \frac{b\sqrt{K}}{\rho_f} \tag{A.39}$$

The uncertainty in the permeability and drag coefficient are

$$\frac{U_K}{K} = \frac{U_a}{a} \tag{A.40}$$

$$\frac{U_{C_f}}{C_f} = \sqrt{\left(\frac{U_b}{b}\right)^2 + \left(\frac{0.5U_K}{K}\right)^2} \tag{A.41}$$

Assuming the uncertainty in μ_f and ρ_f are zero, the uncertainty in K and C_f are both 12% for 10 PPI foam with $\phi = 0.88$, 10 and 11%, respectively, for 10 PPI foam with $\phi = 0.92$, and 33 and 27%, respectively, for 5 PPI foam with $\phi = 0.89$.

A.5. Uncertainty in Effective Thermal Conductivity

As outlined in Appendix C, multiple experiments are performed to determine the effective conductivity of each foam sample. The average of these experiments, for each foam sample, is presented as the effective conductivity. Each foam sample has two sources of uncertainty: the uncertainty associated with each experiment and the

confidence interval about the mean. The two sources of uncertainty are combined using RSS to determine the total uncertainty. The confidence interval is

$$CI = \frac{t_{0.05,N-1} S_{k_{eff}}}{\sqrt{N}} \tag{A.42}$$

where N is the number of samples, $t_{0.05,N-1}$ is the 95% t-statistic evaluated at degrees of freedom N-1, and $S_{k_{eff}}$ is the standard deviation of the effective conductivity measurements for each sample.

The uncertainty in each experiment when measuring the effective thermal conductivity, $k_m = QL/A\Delta T$, is

$$\frac{U_{k_m}}{k_m} = \sqrt{\left(\frac{U_Q}{Q}\right)^2 + \left(\frac{U_H}{H}\right)^2 + \left(\frac{U_A}{A}\right)^2 + \left(\frac{U_{\Delta T}}{\Delta T}\right)^2} \tag{A.43}$$

The uncertainty in the effective conductivity is at most 10%. The uncertainty in the power input is estimated from Eq. (A.20). The uncertainty in the measurement of the height is estimated as the average uncertainty in the foam samples of 25.4 mm height that were used to estimate the effective thermal conductivity ($u_H/H = 0.15\%$). The uncertainty in the measurement of the heat transfer area, $A = \pi D^2/4$, is

$$\frac{U_A}{A} = \sqrt{\left(\frac{2U_D}{D}\right)^2} = \frac{2U_D}{D} \tag{A.44}$$

where D is the inside diameter of the acrylic cylinder. The inside diameter of the cylinder is calculated by measuring the outside diameter and subtracting the wall thickness.

$$D = D_o - t \tag{A.45}$$

The outside diameter and thickness are measured with the digital caliper described in Section A.3. Uncertainty in Porosity. The uncertainty in the inside diameter is

$$U_D = \sqrt{\left(U_{D_o}\right)^2 + (U_t)^2} \tag{A.46}$$

A.6. Uncertainty in Nusselt number

Neglecting the uncertainty in fluid conductivity, the uncertainty in the fluid Nusselt number, $Nu_H = A\Delta TH/Qk_f$, is

$$\frac{U_{Nu_H}}{Nu_H} = \sqrt{\left(\frac{U_A}{A}\right)^2 + \left(\frac{U_{\Delta T}}{\Delta T}\right)^2 + \left(\frac{U_H}{H}\right)^2 + \left(\frac{U_Q}{Q}\right)^2} \tag{A.47}$$

The uncertainty in the Nusselt number averages 5% and is as high as 10%. The uncertainty is dominated by the uncertainty in the average temperature measurement.

A.7. Uncertainty in Rayleigh number

Neglecting the uncertainty in fluid properties and the acceleration due to gravity, the uncertainty in the Rayleigh number, $Ra_H = g\beta\Delta TH^3/\alpha\nu$, is

$$\frac{U_{Ra_H}}{Ra_H} = \sqrt{\left(\frac{U_{\Delta T}}{\Delta T}\right)^2 + \left(\frac{3U_H}{H}\right)^2} \tag{A.48}$$

The uncertainty in the Nusselt number averages 6% and is as high as 14%. The uncertainty is dominated by the uncertainty in the average temperature measurement when the test section height is large and is dominated by the uncertainty in the test section height when the test section height is small.

A.8. Uncertainty in Nusselt Number for Water Alone

The Nusselt number for water alone is determined using the correlation $\mathrm{Nu_{H,w}} = 0.13\mathrm{Ra_H^{0.296}}$. The uncertainty associated with the accuracy of the curve fit and the uncertainty of the independent variable used to evaluate the correlation are combined using RSS to determine the total uncertainty.

To determine the uncertainty in the Nusselt number for water associated with the independent variable, the uncertainty in the measured Rayleigh number is propagated through the curve fit equation

$$\left(\mathrm{U_{Nu_{H,w}}}\right)_{\substack{\text{independent}\\ \text{variable}}} = \mathrm{Nu_{H,w}}\sqrt{\left(\frac{0.296\mathrm{U_{Ra_H}}}{\mathrm{Ra_H}}\right)^2} = \mathrm{Nu_{H,w}}\frac{0.296\mathrm{U_{Ra_H}}}{\mathrm{Ra_H}} \tag{A.49}$$

where $\mathrm{Ra_H}$ is the measured Rayleigh number. The relative uncertainty associated with the accuracy of the curve fit is estimated as the confidence interval of the fit $\mathrm{CI} = \pm \mathrm{t_{0.05,N-2}} \cdot \mathrm{SEE} = 1.5\%$, where SEE is the standard error of the estimate

$$\left(\mathrm{U_{Nu_{H,w}}}\right)_{\substack{\text{accuracy of}\\ \text{curve fit}}} = \mathrm{Nu_{H,w}}\left[\frac{1.5}{100}\right] \tag{A.50}$$

where $\mathrm{Nu_{H,w}}$ is the measured Nusselt number. Combining Eq. (A.49) and Eq. (A.50), the uncertainty in the predicted Nusselt number for water alone is

$$\mathrm{U_{Nu_{H,w}}} = \sqrt{\left[\mathrm{Nu_{H,w}}\frac{0.296\mathrm{U_{Ra_H}}}{\mathrm{Ra_H}}\right]^2 + \left[\mathrm{Nu_{H,w}}\left[\frac{1.5}{100}\right]\right]^2} \tag{A.51}$$

where $\mathrm{U_{Ra_H}}/\mathrm{Ra_H}$ is the uncertainty in the measured Rayleigh number. The uncertainty averages 2% and is as high as 5%. When the uncertainty in the Rayleigh number is large

the uncertainty in the predicted Nusselt number is dominated by the uncertainty in the Rayleigh number. Otherwise the uncertainty is dominated by the confidence interval of the fit.

A.9. Uncertainty in Enhancement Factor

The enhancement factor is $E = \left.\frac{Nu_{H,foam}}{Nu_{H,water}}\right|_{Ra_H=const} - 1$. The uncertainty in the enhancement factor is

$$U_E = \sqrt{\left(\frac{Nu_{H,f}}{\left(Nu_{H,w}\right)^2} U_{Nu_{H,w}}\right)^2 + \left(\frac{U_{Nu_{H,f}}}{Nu_{H,w}}\right)^2} \tag{A.52}$$

The uncertainty in the Nusselt number with foam, $Nu_{H,f}$, is given in Eq. (A.47) and the uncertainty in the Nusselt number with water alone is given Eq. (A.51). The average uncertainty is 6% and is as high as 10%. The uncertainty is dominated by the uncertainty in the measured Nusselt number.

APPENDIX B HEAT LOSS CALCULATIONS

Heat loss through the base of the apparatus, Q_{L_1}, is assumed to be one dimensional and is calculated using the temperature drop across the polycarbonate separator plate of length L_1 (6.35 mm).

$$Q_{L_1} = \frac{k_p A\left(T_{S_1} - T_{S_2}\right)}{L_1} \tag{B.1}$$

where k_p is the conductivity of the polycarbonate separator plate ($0.195\ W/m\ K$), and A is the area of the separator plate ($0.0127\ m^2$).

Losses from the side of the cylinder are calculated by assuming one dimensional radial heat loss at three locations: the region of the test section, the region near the hot plate, and the region near the separator place. Shown in Figure 3.9 at each of these three regions, the temperature of the outer wall (respectively T_{mo}, T_{ho}, and T_{so}) is measured in the middle of each section at two locations 180° apart. The temperature at each section is the average of the two thermocouples.

For the radial heat loss in the region containing the test section of height H, the temperature on the inside of the cylinder is assumed to be the average of the hot and cold plate, $\frac{T_h+T_c}{2}$. The heat loss is estimated to be

$$Q_{L_2} = \frac{2\pi H k_a \left(\frac{T_h + T_C}{2} - T_{mo}\right)}{\ln(d_o/d_i)} \tag{B.2}$$

where k_a is the conductivity of acrylic ($0.183\ W/m\ K$), and d_o and d_i are the outer and inner radius of the cylinder.

For the radial heat loss in the region near the hot plate, Q_{L_3}, the temperature on the inside of the cylinder is assumed to be the average temperature of the hot plate T_h,

$$Q_{L_3} = \frac{2\pi L_3 k_a (T_h - T_{ho})}{\ln(d_o/d_i)} \tag{B.3}$$

where L_3 is the height of this region (11.11 mm).

For the radial heat loss in the region near the separator plate, the temperature on the inside of the cylinder is assumed to be the average temperature of the separator plate, $\frac{T_{s_1}+T_{s_2}}{2}$. The heat loss is,

$$Q_{L_4} = \frac{2\pi L_4 k_a \left(\frac{T_{s1} + T_{s2}}{2} - T_{so}\right)}{\ln(d_{o2}/d_i)} = \frac{2\pi L_4 k_a \Delta T_{s,r}}{\ln(d_{o2}/d_i)} \tag{B.4}$$

where L_4 is the height of this region (14.29 mm) and d_{o2} is the outer diameter of the cylindrical tube plus a supporting tube of the same thickness (152.4 mm). The total heat loss is the sum of the component heat losses,

$$Q_L = Q_{L_1} + Q_{L_2} + Q_{L_3} + Q_{L_4} \tag{B.5}$$

Table B.1 provides a summary of heat loss components with a description and temperature difference. The total radial heat loss was typically less than 1% of input power, though for lower power experiments the total radial heat loss was as high as 3.7%. The loss through the base of the apparatus was typically 1% of input power and was as high as 2.6% for low power experiments.

Table B.1. Summary of one dimensional heat loss components.

Heat Loss	Description	Temperature difference
Q_{L_1}	Heat loss through base of apparatus	$T_{S_1} - T_{S_2}$
Q_{L_2}	Radial heat loss in the region of the test section	$\left(\frac{T_h + T_C}{2}\right) - T_{mo}$
Q_{L_3}	Radial heat loss in the region of the hot plate	$T_h - T_{ho}$
Q_{L_4}	Radial heat loss in the region of the separator plate	$\left(\frac{T_{s1} + T_{s2}}{2}\right) - T_{so}$

APPENDIX C MEASURED EFFECTIVE CONDUCTIVITY

Empirical estimates of the effective conductivity are available in the literature. An upper bound on the estimate of effective conductivity is calculated by considering heat to flow by conduction through the solid and fluid in parallel

$$k_e = \phi k_f + (1-\phi)k_s \tag{C.1}$$

A lower bound on the estimate of effective conductivity is calculated by considering heat to flow by conduction through the solid and fluid in series

$$k_e = \frac{1}{\frac{\phi}{k_f} + \frac{1-\phi}{k_s}} \tag{C.2}$$

Calmidi and Mahajan [29] developed an empirical model by modifying the parallel limit. The empirical constants are determined through curve fitting results with ERG Aerospace manufactured aluminum foam of 5, 10, 20, and ,40 PPI and $0.906 < \phi < 0.978$ saturated in air and water. For water, the correlation is

$$k_e = \phi k_f + 0.195(1-\phi)^{0.763} k_s \tag{C.3}$$

Bhattacharya et al. [30] considered an empirical model with contributions from the limiting values of the series and parallel model. The constant 0.35 is determined from curve fitting results with ERG Aerospace manufactured aluminum and reticulated vitreous carbon foam of 5, 10, 20, and 40 PPI and $0.906 < \phi < 0.978$ saturated in air and water

$$k_e = 0.35[\phi k_f + (1-\phi)k_s] + \frac{1-0.35}{\frac{\phi}{k_f} + \frac{1-\phi}{k_s}} \tag{C.4}$$

Ignoring convection and radiation heat transfer, the manufacturer estimates the effective conductivity to be

$$k_e = 0.33 \cdot k_s(1 - \phi) + k_f \tag{C.5}$$

In the present study, an effective thermal conductivity of the copper foam saturated in water is measured by running experiments with the test section completely filled with foam at a preconvention Rayleigh number. Multiple experiments are conducted for a range of Rayleigh numbers to ensure that no convection is taking place in the test section. To confirm pre-convection experiments, an experiment is also performed with the apparatus inverted where a stabilizing temperature gradient exists between the two plates. The effective thermal conductivity of the water-saturated copper foam is

$$k_m = \frac{QH}{A\,(T_h - T_c)} \tag{C.6}$$

where Q is the heat input, H the height of test section, A is the cross sectional of the test section, and T_h and T_c are the average hot and cold plate temperatures.

To reduce contact resistance between the isothermal boundaries and the metal foam, a thin layer of thermally conducting paste (Omegatherm 201, 2.3 W/mK) is applied to the isothermal plates before the foam is inserted into the test apparatus. The thermal paste provides a fixed thermal resistance between the foam and isothermal plate. The addition of the thermal paste reduces the measured effective conductivity of the water-saturated foam. As the height of the foam sample is decreased, the thermal resistance due to the foam becomes a smaller portion of the total resistance and thinner samples have a smaller effective conductivity. During natural convection experiments with a superposed

fluid layer, only one side of the foam contacts an isothermal boundary. However, when the effective conductivity is measured, both sides of the foam contact the boundaries. The measured effective conductivity includes an extra thermal resistance not present in the natural convection experiments.

$$\frac{Q}{A} = k_{e,meas}\frac{\Delta T}{h_p} = \frac{\Delta T}{\frac{h_p}{k_e} + \frac{t_{paste}}{k_{paste}}} \tag{C.6}$$

where $k_{e,meas}$ is the measured effective conductivity during stagnant experiments, k_e is the effective conductivity during natural convection experiments, t_{paste} is the thickness of the paste and k_{paste} is the conductivity of the paste.

The thickness of the thermal paste is 0.25 mm, and the stagnant conductivity experiments are corrected to determine the stagnant conductivity of the foam during natural convection experiments

$$k_e = h_p\left[\frac{h_p}{k_{e,meas}} - \frac{t_{paste}}{k_{paste}}\right]^{-1} \tag{C.6}$$

When measuring the effective conductivity, the uncertainty of the thickness of the paste layer becomes more significant for the thinner foam samples. Therefore. only the effective conductivity of the 25.4 mm foam samples is measured and Eq. (C.5) is used to determine the effective conductivity of the 19.1 mm and 12.7 mm samples. As observed in Eqs. (C.1) – (C.5), the effective conductivity depends on porosity and not pore density.

Table C.1. Measured and corrected effective conductivities.

Experiment	Foam Sample (25.4 mm thickness)	Porosity	Ra_H	k_e, Measured (W/mK)	k_e, Corrected (W/mK)
1	10 PPI, #1	0.914	3.5×10^6	8.8 ± 0.3	9.2 ± 0.3
2	10 PPI, #1	0.914	3.3×10^5	9.0 ± 0.7	9.4 ± 0.7
3	10 PPI, #1	0.914	1.9×10^5	9.0 ± 0.8	9.4 ± 0.8
4	10 PPI, #2	0.918	5.8×10^5	8.3 ± 0.3	8.6 ± 0.3
5	10 PPI, #2	0.918	3.2×10^5	8.2 ± 0.4	8.5 ± 0.4
6	10 PPI, #2	0.918	2.3×10^5	8.2 ± 0.5	8.5 ± 0.5
7	5 PPI	0.893	2.6×10^5	10.0 ± 1.0	10.5 ± 1.0
8	5 PPI	0.893	1.7×10^5	10.0 ± 0.8	10.4 ± 0.8
9	5 PPI	0.893	4.9×10^4	10.2 ± 1.0	10.7 ± 1.0

The measured values for the 5 PPI sample with $\phi = 0.893$ is used for $k_{e,meas}$ in Eq. (C.5) for all samples with $0.880 < \phi < 0.893$. The effective conductivity for the 19.1 mm and 12.7 mm samples is slightly reduced from the 25.4 mm samples because the foam layer is a smaller portion of the total resistance. No distinction was made between the two, 25.4 mm, 10 PPI foam samples with, $\phi = 0.914$ and 0.918, during experiments and the average of the two samples is presented as the effective conductivity for both samples. A summary of the measured effective conductivities is shown in Table C.1. A summary of the average and corrected effective conductivities is shown in Table C.2. The uncertainty of the effective conductivity is discussed in Appendix A.

The present results are compared to the experimental results of Kathare [32] and estimates from Eqs. (C.1) – (C.5) for copper foam of porosity 0.916 and 0.893 in Table C.3. The present results show lower effective conductivity compared to the

Table C.2. Average of measured and corrected effective conductivities.

Foam Sample	Avg. Porosity	Thickness (mm)	Avg. k_e, Measured (W/mK)	Avg. k_e, Corrected (W/mK)
10 PPI	0.916	25.4	8.6 ± 0.6	8.9 ± 0.6
5 PPI	0.893	25.4	10.1 ± 1.0	10.5 ± 1.0
5/10 PPI	0.893	19.1	---	10.4 ± 1.0
5/10 PPI	0.893	12.7	---	10.1 ± 1.0

Table C.3. Comparison of present results with theoretical limits, the correlations of Calmidi and Mahajan [29], and Bhattacharya et al. [30], the manufacturer's estimate [25] and the experimental work of Kathare [32].

Method	k_e, W/mK	
	$\phi = 0.916$	$\phi = 0.885$
Upper bound	33.4	45.3
Lower bound	0.6	0.7
Calmidi and Mahajan [29]	12.1	15.1
Bhattacharya et al. [30]	12.1	16.3
Manufacturer's estimate [25]	12.1	15.7
Kathare [32]	8.8 ± 0.4	-----
Present study (25.4 mm)	8.9 ± 0.6	10.5 ± 1.0

correlations of Calmidi and Mahajan [29], and Bhattacharya et al. [30], as well as the manufacturer's estimate [25]. There are two potential explanations for the present results providing lower effective conductivity than the models of [29] and [30]: The thermal paste thickness was underestimated and the contact resistance due to the thermal paste was not completely corrected for, or the braze material used by [29] and [30] increased the effective conductivity of the foam sample.

APPENDIX D HYPOTHESIS TESTING

Hypothesis testing is performed to determine if the variation in the data, for 10 PPI foam on the hot boundary, with respect to η, is statistically significant. Correlations that consider all data for each PPI were determined using ordinary least squares. Separate correlations were determined for each η and PPI, where the exponent is set to equal that for the correlation that includes all data. The individual correlations were then compared to the correlation that includes all data to determine if the difference is statistically significant. The first section describes the general method of hypothesis testing used. The section defines this procedure for the correlations used in the present experiments. The equations and discussion of hypothesis testing is based on the text of Hayter [40].

D.1. Hypothesis Testing Background for Comparing the Means of Independent Samples with Unequal Variances

For two populations A, and B, with means μ_A and μ_B, the null hypothesis and alternative hypothesis for making an inference on population means is

$$H_0: \mu_A - \mu_B = 0$$
$$H_A: \mu_A - \mu_B \neq 0 \qquad \text{(D.1)}$$

For the null hypothesis, $H_0: \mu_A - \mu_B = 0$, where the estimate of the mean of A is $\bar{x}$ and the estimate of the mean of B is $\bar{y}$, the t-statistic is

$$t = \frac{\bar{x} - \bar{y}}{\sqrt{\frac{s_x^2}{n} + \frac{s_y^2}{m}}} \qquad \text{(D.1)}$$

where s_x and s_y are the standard deviations of the sample means $\bar{x}$ and $\bar{y}$ with sample sizes n and m. The t-distribution has degrees of freedom

$$\nu = \frac{\left(\frac{s_x^2}{n} + \frac{s_y^2}{m}\right)^2}{\frac{s_x^4}{n^2(n-1)} + \frac{s_y^4}{m^2(m-1)}} \tag{D.2}$$

The two-sided p-value is

$$\text{p-value} = 2 \times P(X > |t|) \tag{D.3}$$

where the random variable X has a t-distribution with ν degrees of freedom. $P(X > |t|)$ is the area under the curve of the t-distribution with ν degrees above the value |t|. For a two sided test, this value is doubled to account for the two tails of the t-distribution. The meaning of the p-value is discussed in the following paragraph.

The null hypothesis states that the difference between the population means is zero, $\mu_A - \mu_B = 0$. If population means are estimated again, $\bar{x}_1$ and $\bar{y}_1$, the p-value is the probability that the difference between the new estimate of the population means , $\bar{x}_1 - \bar{y}_1$, is equal to or greater than the current difference, $\bar{x} - \bar{y}$, if the null hypothesis is true. If this probability is sufficiently small, then it is unlikely that the null-hypothesis is true and there is evidence that the population means are different. For 95% confidence, if p-value is smaller than 5% (a significance level $\alpha = 0.05$), the null hypothesis is rejected in favor of the alternative hypothesis; the population means are different.

D.2. Hypothesis Testing for Current Results

Consider a family of curves of the form $Nu_H = \chi Ra_H^n$ where curves differ by the pre-exponential factor χ. A finite sample of the population of one of the curves is measured and the true value of the constant χ is estimated as C using ordinary least squares (after the data are linearized). The standard error of the estimate is

$$SEE = \sqrt{\frac{1}{N-1}\sum_{n=1}^{N}(Nu_i - Nu_i')^2} \tag{D.4}$$

where Nu_i is the measured value of Nu for a given Ra_i and Nu' is the predicted value of Nu for a given Ra_i. Note that $1/(N-1)$ is used instead of $1/(N-2)$ for typical linear curve fitting because the exponent is considered to be a known value, equal to that of the correlation that includes all data for each PPI, and does not contribute to the degrees of freedom. If the exponent is not known, SEE is calculated using $1/(N-2)$. If estimates of the pre-exponential factor for two sets of curves are obtained through measurement, the values of C can be compared using hypothesis testing to determine if the estimates are statistically different. The hypothesis testing procedure described in the preceding section is used during data analysis though the standard error of the estimate for each set of data (SEE) is used for the standard deviation (s_x and s_y), the number of data points for each set of data is used for the number of samples (n and m), and the estimates of the true pre-exponential factor for each set of data (C) are used for estimates of the mean ($\bar{x}$ and $\bar{y}$).

Table D.1. Results of hypothesis testing.

Config.	Correlation Data, $Nu = CRa_H^n$					Hypothesis testing results, comparing C for water alone to C for the foam cases $H_0: \chi_w - \chi_f = 0,\ H_A: \chi_w - \chi_f \neq 0$			
	n	C	R^2	Count	SEE	DOF	t-stat	p-value	Result ($\alpha = 0.05$)
5 PPI (all data)	0.287	0.164	0.99	18	0.019	---	---	---	---
$\eta = 0.25$	0.287	0.165	0.98	6	0.017	9.6	0.15	0.89	Fail to reject null hypothesis
$\eta = 0.5$	0.287	0.164	0.99	6	0.019	8.6	0.03	0.98	Fail to reject null hypothesis
$\eta = 0.75$	0.287	0.164	0.98	6	0.023	7.6	0.15	0.89	Fail to reject null hypothesis
10 PPI (all data)	0.284	0.155	0.99	22	0.020	---	---	---	---
$\eta = 0.25$	0.284	0152	0.97	9	0.024	12.7	1.28	0.22	Fail to reject null hypothesis
$\eta = 0.5$	0.284	0153	0.99	8	0.018	13.5	0.83	0.42	Fail to reject null hypothesis
$\eta = 0.75$	0.284	0161	0.99	6	0.013	12.2	2.45	0.03	Reject null hypothesis

D.2.1. Results of Hypothesis Testing

The results of the correlation and hypothesis testing are shown in Table D.1. The hypothesis testing compares the pre-exponential factor for the case that includes all data for each PPI to that of the cases that individually consider each η, for each PPI. The 5 PPI foam is not a function of η. The variation in the 10 PPI, $\eta = 0.25$ and 0.5 data is not significant. The pre-exponential factor for $\eta = 0.75$ is 4% higher than the pre-exponential factor for the correlation that considers all η, which is significant to a 95% confidence level ($p_{value} = 0.03$).

APPENDIX E FLUID PROPERTY CORRELATIONS

Table E.1 lists water property correlations determined using Engineering Equation Solver V8.422-3D at an ambient pressure of 101.325 kPa and over the temperature range 15 – 35 °C. A forth order polynomial is fit to the EES data over the temperature range 15 – 35 °C using Microsoft Excel. The error of the curve fits is negligible.

Table E1. Properties of water at 101.325 kPa over the temperature range 15 – 35 °C.

Water Property	Correlation of the form $AT^4 + BT^3 + CT^2 + DT + E$				
	A	B	C	D	E
α [m^2/s]	-1.9841E-14	2.1919E-12	-9.4575E-11	2.6425E-09	1.0804E-07
β [1/K]	-2.6171E-11	4.2951E-09	-3.1902E-07	1.9096E-05	-7.5474E-05
ν [m^2/s]	1.0632E-13	-1.7172E-11	1.2624E-09	-5.7666E-08	1.7726E-06
k [W/m-K]	8.1122E-10	-1.3353E-07	-2.6979E-06	2.0256E-03	5.4758E-01
c_p [J/kg-K]	4.8356E-05	-5.6218E-03	2.3739E-01	-4.3227E+00	4.2117E+03